JAERI-Research
97-065

NEUTRONICS ANALYSIS OF INTERNATIONAL FUSION MATERIAL IRRADIATION FACILITY (IFMIF) – JAPANESE CONTRIBUTIONS –

October 1997

Yukio OYAMA, Kazuaki KOSAKO*and Kenji NODA

日本原子力研究所
Japan Atomic Energy Research Institute

本レポートは，日本原子力研究所が不定期に公刊している研究報告書です。
入手の問合わせは，日本原子力研究所研究情報部研究情報課（〒319-11 茨城県那珂郡東海村）あて，お申し越しください。なお，このほかに財団法人原子力弘済会資料センター（〒319-11 茨城県那珂郡東海村日本原子力研究所内）で複写による実費頒布をおこなっております。

This report is issued irregularly.
Inquiries about availability of the reports should be addressed to Research Information Division, Department of Intellectual Resources, Japan Atomic Energy Research Institute, Tokai-mura, Naka-gun, Ibaraki-ken 319-11, Japan.

編集兼発行　日本原子力研究所
印　　刷　㈱原子力資料サービス

Neutronics Analysis of International Fusion Material Irradiation Facility (IFMIF) - Japanese Contributions -

Yukio OYAMA, Kazuaki KOSAKO* and Kenji NODA

Department of Materials Science and Engineering
Tokai Research Establishment
Japan Atomic Energy Research Institute
Tokai-mura, Naka-gun, Ibaraki-ken

(Received August 29, 1997)

In fusion reactor development for demonstration reactor, i.e., DEMO, materials tolerable for D-T neutron irradiation are absolutely required for both mechanical and safety point of views. For this requirement, several kinds of low activation materials were proposed. However, experimental data by actual D-T fusion neutron irradiation have not existed so far because of lack of fusion neutron irradiation facility, except fundamental radiation damage studies at very low neutron fluence. Therefore such a facility has been strongly requested. According to agreement of need for such a facility among the international parties, a conceptual design activity (CDA) of International Fusion Material Irradiation Facility (IFMIF) has been carried out under the frame work of the IEA-Implementing Agreement. In the activity, a neutronics analysis on irradiation field optimization in the IFMIF test cell was performed in three parties, Japan, US and EU. As the Japanese contribution, the present paper describes a neutron source term as well as incident deuteron beam angle optimization of two beam geometry, beam shape (foot print) optimization, and dpa, gas production and heating estimation inside various material loading Module, including a sensitivity analysis of source term uncertainty to the estimated irradiation parameters.

Keywords: IFMIF, Neutronics, Fusion Materials, DT Neutron Irradiation, dpa, He Production,

---

* Sumitomo Atomic Energy Industries Ltd.

国際核融合材料照射施設（IFMIF）の中性子工学解析
—日本の寄与—

日本原子力研究所材料研究部
大山　幸夫・小迫　和明*・野田　健治

（1997年8月29日受理）

核融合実証炉（DEMO）の建設のために、構造安全の観点からD-T中性子に耐照射性のある材料の開発は必須である。このため、いくつかの低放射化材料が提案されている。しかし、これまでD-T中性子による工学的材料データの取得が行える材料照射施設が無いためにその実験データが無く、このような試験施設の建設が強く望まれている。この背景の下に、国際的な合意に基づきIEAの下で国際核融合材料照射施設（IFMIF）の概念設計活動（CDA）が実施された。この活動の中でIFMIFに関する中性子工学的解析が日米欧の3極で行われ、得られる照射場の最適化検討が行われた。日本の貢献部分としては、線源項、入射ビーム角及びビーム形状の最適化、照射モジュール内でのdpa、He生成、核発熱についての検討、また、線源項の不確定さが結果に及ぼす影響の検討が上げられる。本報告では、これらの検討結果をまとめた。

東海研究所：〒319-11　茨城県那珂郡東海村白方白根2—4
*住友原子力（株）

Contents

目　　次

1. Introduction

In fusion reactor development for demonstration reactor, i.e., DEMO, materials tolerable for D-T neutron irradiation are absolutely required for both mechanical and safety point of views. For this requirement, several kinds of low activation materials were proposed. However, experimental data by actual D-T fusion neutron irradiation have not existed so far because of lack of fusion neutron irradiation facility, except fundamental radiation damage studies at very low neutron fluence. Therefore such a facility has been strongly requested. The US proposed the FMIT facility[1] and performed design work but the project was terminated in 1985. After the FMIT project, as a Japanese domestic project, the conceptual design study of ESNIT was performed in 1988-1995 for an energy selective accelerator and less laborious specification to construct in shortest period.[2] At the same time, international technical assessment working group of material scientists recommended to study of conceptual design of International Fusion Material Irradiation Facility (IFMIF) and select d-Li reaction type neutron source as a candidate.[3] According to agreement between the international parties, a conceptual design activity (CDA) of IFMIF has been carried out under the frame work of the IEA-Implementing Agreement for a Programme of Research and Development on Fusion Materials since 1995.[4]

The basic concept of IFMIF consists of the deuteron linac accelerator system, the target system, and the irradiation test cell. Two deuteron accelerators of energy up to 40 MeV and of 125 mA are used for irradiation at the same time on single target. The FMIT type Li-jet stream is adopted for the target. The test module with sample materials loading is placed in the test cell. The CDA task is separated into three major design units, i.e., the accelerator system, the target system and the test cell. These are performed consistently each other by design integration which includes building and utilities. The test cell design strongly requests neutronics analysis because the test module and beam spot sizes depend much on spatial distribution of neutron flux or damage parameters inside the test module in optimizing irradiation strategy. The nuclear heating estimation is also required to design cooling systems for the test module, the test assembly and the test cell itself.

The neutronics analysis was performed in three parties, Japan, US and EU. This report gives only Japanese contributions. Japanese contributions include source function production, incident deuteron beam angle optimization of two beam geometry, beam shape (foot print) optimization, and dpa, gas production and heating estimation inside various material loadings. Also a sensitivity analysis of source term uncertainty to the estimated parameters was performed. In the present paper, neutron source term for neutronics analysis and target spot size effect on neutron field are described in Chapter 2, neutron flux and damage parameters inside sample loading materials comparing with the DEMO reactor environment in Chapter 3, dpa and nuclear heat distribution inside the test cell useful for test

cell design in Chapter 4, some uncertainty analyses in Chapter 5, and summary in Chapter 6. In appendix, some ideas for dosimetry method for this facility are described.

2. Neutron Source Term by D-Li Reaction for Neutronics Calculations

To evaluate neutron irradiation field obtained from the d-Li neutron source of IFMIF (International Fusion Material Irradiation Facility), a neutron source function was prepared for the proposed acceleration energies of 30, 35 and 40 MeV. The source function is used as the source term for neutron transport calculations for obtaining damage parameters inside the materials samples located in front of the Li target, and also for shielding design calculations. The source function consists of angle-dependent energy spectrum of emitted neutrons.

There exist no experimental data of energy differential neutron emission cross section data with good accuracy and fully covered for emitted neutron spectrum. Only the thick target experiments are available. The deuteron stopping range in these energies is large enough to affect neutron field characteristics by dependence of reaction position. The stopping range for 35 MeV deuteron in lithium is 17 mm, while the test module is placed at the distance of 1-2 mm from the target backwall. The deuteron energy is changed along the track by energy loss and also changed reaction energy for producing neutrons. Therefore one has to prepare an energy differential cross section model to provide the neutron emission source term inside the target region.

The source function was calculated based on the method developed in the previous work for ESNIT at JAERI.[5] For the present work, the computer code with that method was modified to add the capability of two beam geometry and three dimensional treatment. The deuteron reaction energy is changed with the depth but the same energy on the vertical plane of the same depth for single beam. This is still correct, when two beams are incident to the target with symmetrical angle.

2.1. Nuclear Reaction Model

2.1.1 Deuteron Slowing Down

Assuming that the attenuation of deuteron flux through the range is negligible, the integration through the trajectory can be transformed to the integration by deuteron energy using stopping power. Here we replace the integration with respect to z', i.e., the depth inside the target, by the deuteron energy which can be related to the depth z' by using the stopping power.

We calculate the d-Li reaction rate at deuteron depth z in the Li layer as follows:

cell design in Chapter 4, some uncertainty analyses in Chapter 5, and summary in Chapter 6. In appendix, some ideas for dosimetry method for this facility are described.

2. Neutron Source Term by D-Li Reaction for Neutronics Calculations

To evaluate neutron irradiation field obtained from the d-Li neutron source of IFMIF (International Fusion Material Irradiation Facility), a neutron source function was prepared for the proposed acceleration energies of 30, 35 and 40 MeV. The source function is used as the source term for neutron transport calculations for obtaining damage parameters inside the materials samples located in front of the Li target, and also for shielding design calculations. The source function consists of angle-dependent energy spectrum of emitted neutrons.

There exist no experimental data of energy differential neutron emission cross section data with good accuracy and fully covered for emitted neutron spectrum. Only the thick target experiments are available. The deuteron stopping range in these energies is large enough to affect neutron field characteristics by dependence of reaction position. The stopping range for 35 MeV deuteron in lithium is 17 mm, while the test module is placed at the distance of 1-2 mm from the target backwall. The deuteron energy is changed along the track by energy loss and also changed reaction energy for producing neutrons. Therefore one has to prepare an energy differential cross section model to provide the neutron emission source term inside the target region.

The source function was calculated based on the method developed in the previous work for ESNIT at JAERI.[5] For the present work, the computer code with that method was modified to add the capability of two beam geometry and three dimensional treatment. The deuteron reaction energy is changed with the depth but the same energy on the vertical plane of the same depth for single beam. This is still correct, when two beams are incident to the target with symmetrical angle.

2.1. Nuclear Reaction Model

2.1.1 Deuteron Slowing Down

Assuming that the attenuation of deuteron flux through the range is negligible, the integration through the trajectory can be transformed to the integration by deuteron energy using stopping power. Here we replace the integration with respect to z', i.e., the depth inside the target, by the deuteron energy which can be related to the depth z' by using the stopping power.

We calculate the d-Li reaction rate at deuteron depth z in the Li layer as follows:

$$S(z,E_n,\Omega)dzd\Omega_{Lab}dE_{n,Lab}=\frac{N\cdot J}{e}\left[\left(\frac{d^2\sigma}{d\Omega dE_n}\right)_{CM}\left|\frac{\partial(\Omega_{CM},E_{n,CM})}{\partial(\Omega_{Lab},E_{n,Lab})}\right|\frac{1}{(dE_d/dz)}dz\right]d\Omega_{Lab}dE_{n,Lab}\ ,$$

[n/s/sr/MeV/cm] (2.1)

where (dE_d/dX) is the stopping power of deuterons in Li, J the deuteron current density, N the Li density, $(d^2\sigma/d\Omega dE)$ the d-Li cross section, and Jacobian term. The stopping power is represented for the incident energy range of 1-100 MeV as the following formula given in Ref. 6.

$$\left(\frac{dE_d}{dX}\right)=\left(A_6/\beta^2\right)\left[\ln\left(\frac{A_7\beta^2}{1-\beta^2}\right)-\beta^2-\sum_{i=0}^{4}A_{i+8}(\ln E_d)^i\right]$$

[eV/(10^{15}atoms/cm^2)] (2.2)

where E_d = deuteron energy/deuteron mass [keV/amu], b = v/c and A_i is given for lithium in the table of Ref. 2 as A_6=0.00153, A_7=21470, A_8=-0.5831, A_9=0.562, A_{10}=-0.1183, A_{11}=0.009298 and A_{12}=-0.000166, respectively.

2.1.2 Cross Section Model

The differential cross section is calculated by the same assumption as that of Johnson et al.,[7] except some modifications. The neutron production reaction of ^{7}Li(d,n)^{8}Be is only considered for the main reaction among the possible reactions, and in the calculation of cross sections the Serber's stripping reaction model[8] and the evaporation process are taken into account by the following linear combination.

$$\left(\frac{d^2\sigma}{d\Omega dE_n}\right)=A_S\cdot\left(\frac{d^2\sigma}{d\Omega dE_n}\right)_{Serber}+A_C\cdot\left(\frac{d^2\sigma}{d\Omega dE_n}\right)_{Evapolation}, \quad (2.3)$$

The first term by the Serber's theory is written as follows:

$$\left(\frac{d^2\sigma}{d\Omega dE_n}\right)_{Serber}=\frac{1}{2}\cdot\frac{(E_d-E_b)\cdot E_b}{\left[(E_n-E_d/2)^2+E_b\cdot E_d\right]^{3/2}}\cdot\frac{\Theta_0}{\left(\Theta_0^2+\Theta^2\right)^{3/2}} \quad \text{for} \quad |E_n-E_d/2|<2(\Delta E)_{1/2}$$

$$=0 \quad \text{for} \quad |E_n-E_d/2|\geq 2(\Delta E)_{1/2} \quad (2.4)$$

where E_d : Incident deuteron energy,

E_b : Binding energy of deuteron,

Θ_0 : $\sqrt{E_b/E_d}$.

And the second term of evaporation process is due to compound reaction:

$$\left(\frac{d^2\sigma}{d\Omega dE_n}\right)_{Evapolation}=E_n\cdot e^{(-E_n/T)}\ , \quad (2.5)$$

where $T: 3.2\sqrt{E_d/A}$ (A: mass number).

Here we modified the Serber's cross section by adding the energy cut-off (E_C = $E_d/2 \pm$ FWHM , full-width-half-maximum) for the neutron spectrum tail by Eq. (2.4), because the high energy tail of Serber's spectrum breaks an energy conservation law and that model may be valid only for a gross structure. This energy cut-off, however, can not eliminate producing the negative energy neutrons in lower energy tail by this model. This may provide the unreasonable increase of the lower energy neutrons below ~2 MeV, and also the break-up reactions to two or three bodies should be taken into account for low energy range. Hence this modification is not valid for such low energy region. The other type of reaction is also necessary to be considered for the higher energy neutrons above E_d; Q-value of 15 MeV means there is a possibility for generating the high energetic neutrons of E_d+15 MeV to the ground state of residual nuclei. Since this is not considered here, higher energy neutrons are produced only as an evaporation tail.

The A_S and A_C are energy dependent mixing parameters of two spectral shapes. The energy cut-off of 6 MeV for A_S comes from the low energy limit of stripping reaction for ^{7}Li. The shoulder of 10 MeV was introduced as an energy-weighting parameter but it was insensitive. The parameter A_C was weighted for lower energy deuterons below 15 MeV. The energy cut-off of 2 MeV for the energy of coulomb barrier and the high energy cut-off of 15 MeV for energy weighting parameter were introduced for A_C. The values of parameters in A_S and A_C were determined by the trial and error method to reproduce the measured spectrum and angular distribution. The evaporation part is essential for representing the angular dependence of neutron spectrum.

2.1.3 Normalization

The source term of $S(z,E_n,\Omega)dzd\Omega_{Lab}dE_{n,Lab}$ was normalized by comparison with the experiment. The experiments were always measured at the position far from the target. This measured flux corresponds to the followings:

$$\Phi(E_n,\Omega)d\Omega_{Lab}dE_{n,Lab} = [\int_{surface}^{range} S(z,E_n,\Omega)dz\ ]d\Omega_{Lab}dE_{n,Lab} \quad [\text{n/s/sr/MeV}] \quad . \qquad (2.6)$$

The integration is performed from the Li target surface to deuteron stopping range, i.e., 13, 17 and 22 mm for 30, 35 and 40 MeV, respectively. The normalization was done at 32 MeV deuteron energy using Lone and Sugimoto experiments[9,10], taking average of both experimental value of flux integration above 2 MeV for emission at 0 degree direction.

2.2 Neutron Field of Two Beam-on Target Geometry

Two separated beams are recommended for injection in order to reduce the risk for development of high current accelerator. To check the effect of two beam geometry on the flux distribution in the irradiation field, the program was modified to calculate the flux superposed by two beams with a fixed angle. This calculation was done for 100 x 100 mm square target configuration as shown in Fig. 2.2.1. The beam angles of 0, 5 and 15 degrees from the center axis were examined in terms of volume-flux and flux gradient relations.

The contour flux distribution in the case of 35 MeV deuteron incident energy is shown in Fig.2.2.2 for beam angle of 0 degree, i.e., in symmetric of x and y axes. The contour flux distributions on the x-z and y-z planes are also shown in Figs. 2.2.3-6 for the beam angles of 5 and 10 degrees, respectively. The equal flux region along the y axis are flattened with a distance from the target with increase of incident angle, but the flux gradient increases on the z axis.

The neutron energy spectra at the different distances from 1 to 20 cm in front of the target are shown in Fig. 2.2.7 in the case of 35 MeV deuteron energy and 0-degree beam angle. This figure indicates that the neutron peak energy shifts to lower energy with approaching tha target. This energy shift does not depend on the beam angle as shown in Fig. 2.2.8. However, as seen in Fig. 2.2.9 and 2.2.10, the flux at the position far from the target decreases with increase of the beam angle. The independence of peak energy shift from the beam angle may suggest that neutrons generated at the end of the range contribute more than neutrons genrated by high energy deuterons, because of $1/r^2$ law.

Figures 2.2.11-13 show neutron spectra of neutrons emitted for forward direction (0-5 degrees) from various depths in the Li target with 30, 35 and 40 MeV of deuteron incident energies and for the case with 10 degree of incident beam angle. These spectra are normalized as observed at very far position from the target, i.e., to allow the point source approximation. The deuteron ranges for those energies are 13, 17 and 21 mm, respectively. From the figures, one can see that neutrons born at the surface have a stripping reaction peak, while neutrons in deep position have evaporation spectra. In the medium region, the peak energy of the spectra shifts to lower energy.

Figures 2.2.14 and 2.2.15 show dpa and He production rates for ^{56}Fe as a function of the distance from the target surface. To compare characteristics of the irradiation filed to fusion reactor environment, the ratio of He production to dpa is shown in Fig. 2.2.16. This ratio is quickly approaching, with increase of distance from the target, to 14 the ratio of which is typically seen in a fusion reactor. At the distance more than 5 cm from target, the ratio is almost 14. For the flux gradient, which is required to be less than 10%/cm from the uniformity inside the specimen, Table 2.2.1 summarizes the gradient of dpa and He

production rates. These results show that the beam angle within 10 degree could be within 10%/cm gradient, though the gradient becomes steeper with increase of beam angle.

Finally, for the flux-volume relation, i.e., the required flux vs. the volume in which the required flux can be obtained, the beam angle does not affect significantly the volume for required flux as seen in Fig. 2.2.17. The relative effect of beam angle to the irradiation volume is shown in Fig. 2.2.18 by percentage ratio to the 0 degree case.

In conclusion, it is recommended for the beam angle of the incident deuterons that the angle should be less than 15 degree from the center axis to keep the gradient requirement and might be allowed by 10 degree at maximum.

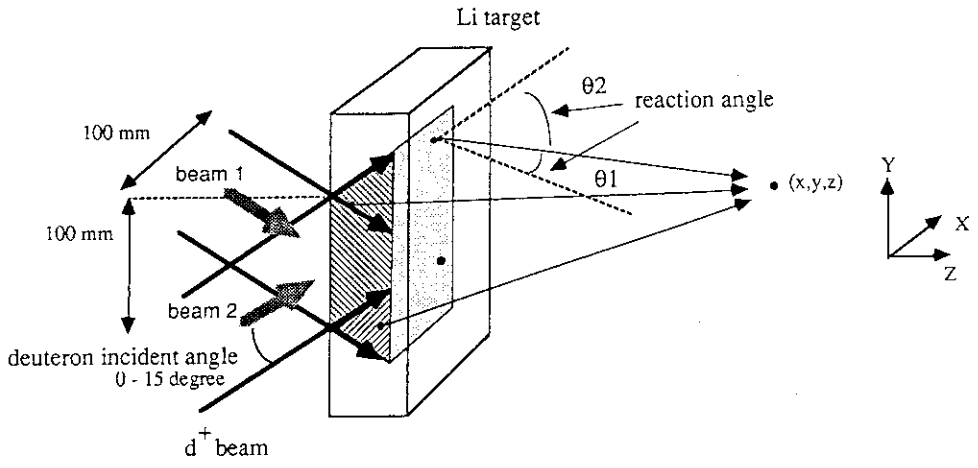

Fig. 2.2.1 Neutron flux and spectrum calculation model at positions in irradiation field. Two beams are incident on the x-z plane.

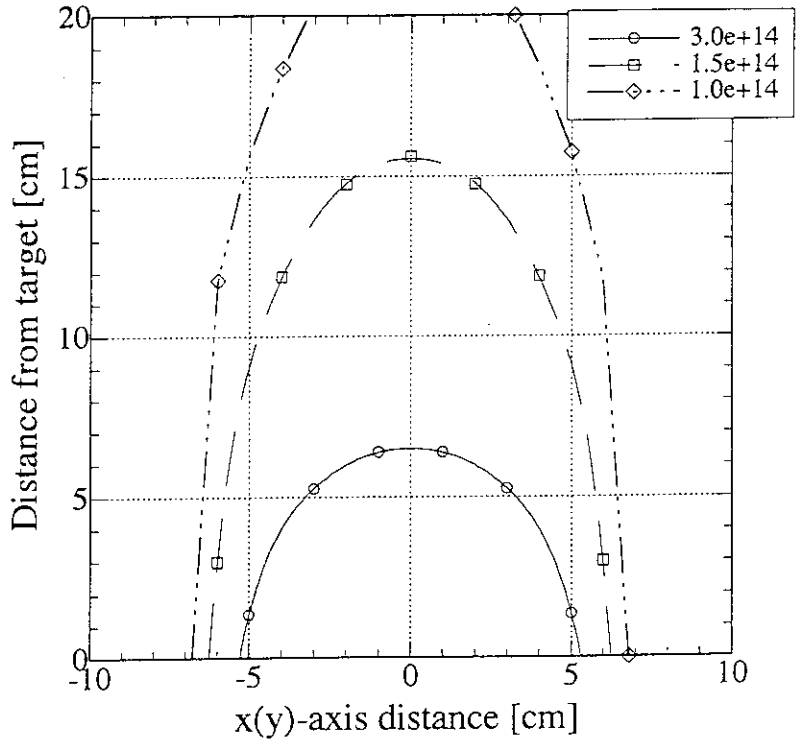

Fig. 2.2.2 Contour plot of neutron flux on x-z plane in the case of 0 degree of beam angle for 35 MeV deuteron

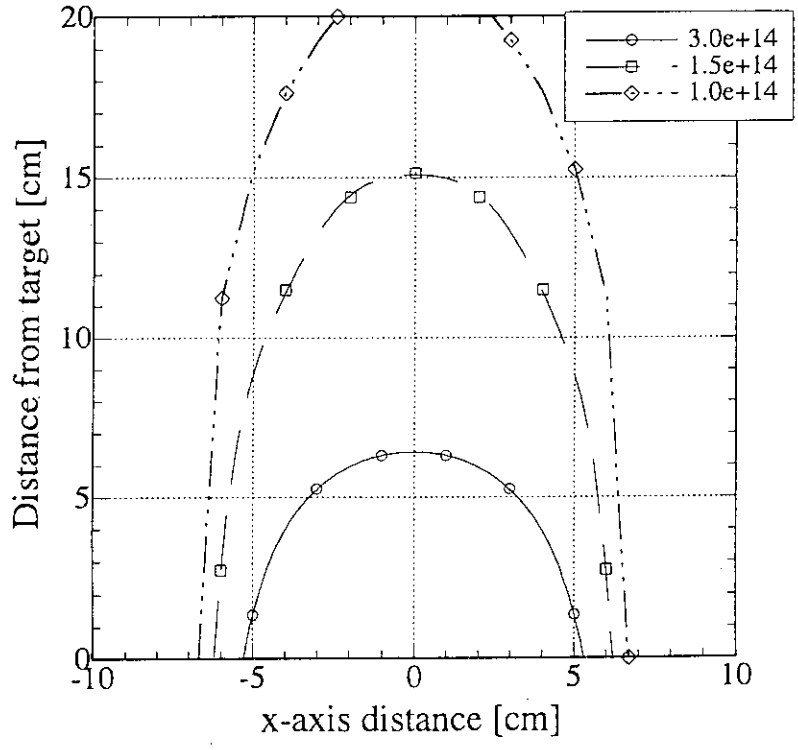

Fig. 2.2.3 Contour plot of neutron flux on x-z plane in the case of 5 degree of beam angle for 35 MeV deuteron

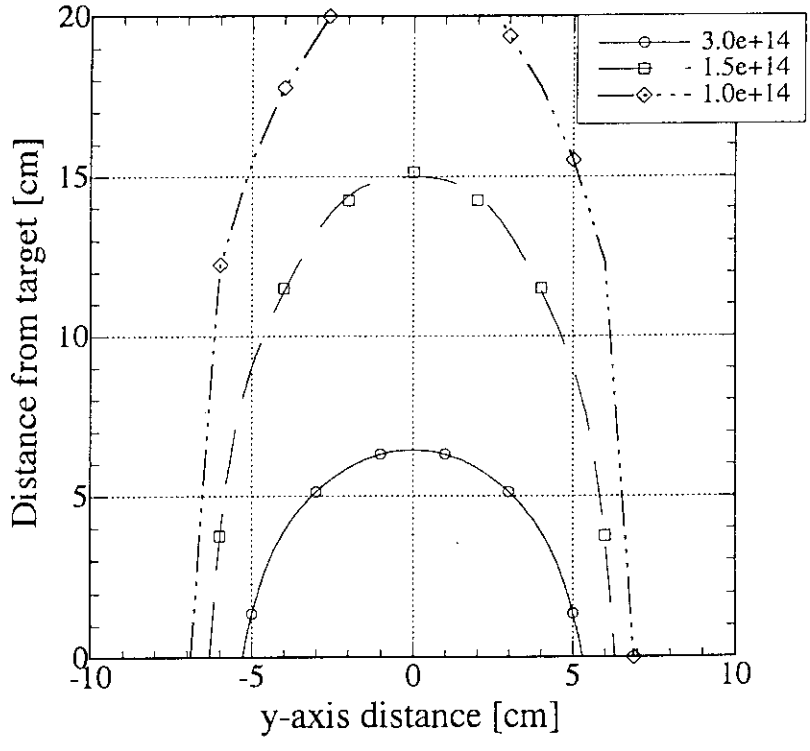

Fig. 2.2.4 Contour plot of neutron flux on y-z plane in the case of 5 degree of beam angle for 35 MeV deuteron

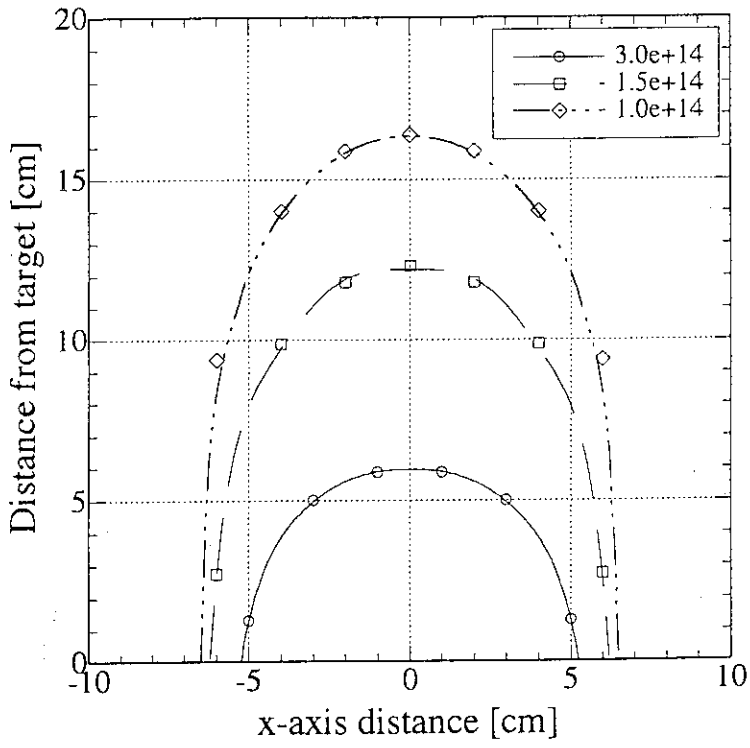

Fig. 2.2.5 Contour plot of neutron flux on x-z plane in the case of 15 degree of beam angle for 35 MeV deuteron

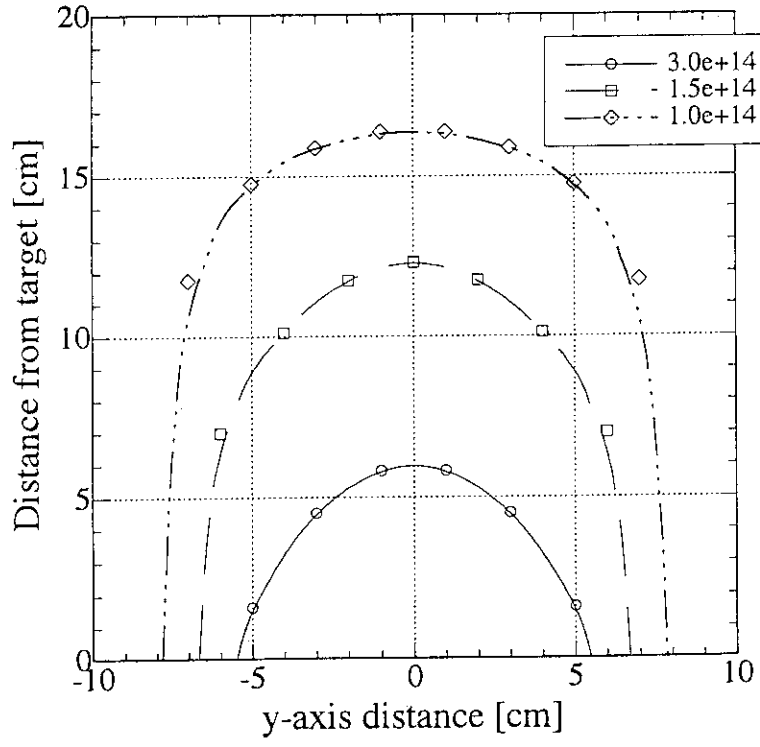

Fig. 2.2.6 Contour plot of neutron flux on y-z plane in the case of 15 degree of beam angle for 35 MeV deuteron

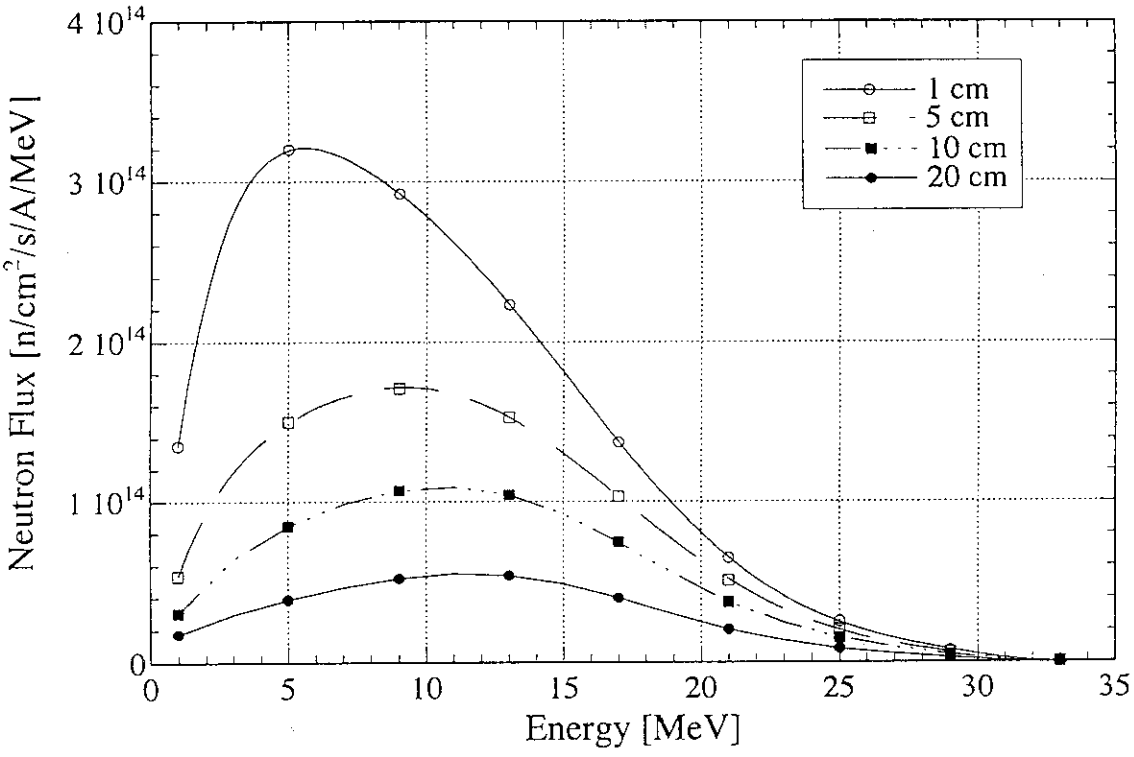

Fig. 2.2.7 Neutron spectra at 4 different positions on z axis (beam direction) for 35 MeV deuteron and 0 degree of two beam angle

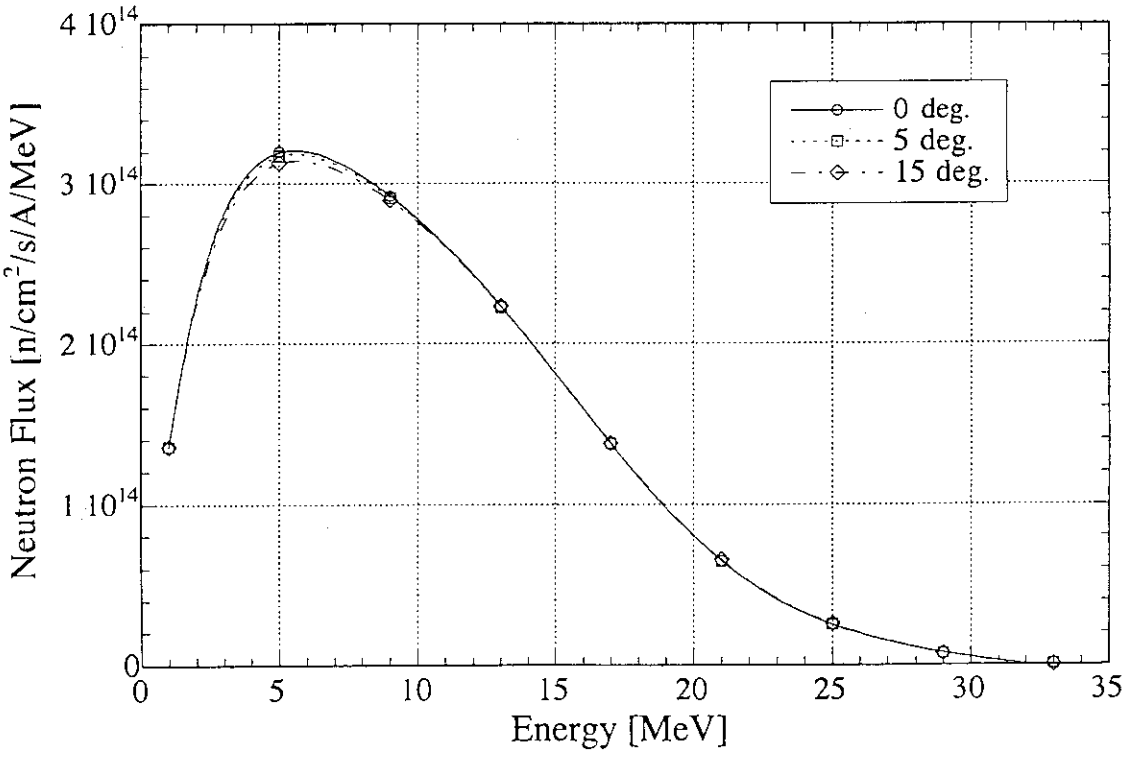

Fig. 2.2.8 Neutron spectra at 1 cm on z axis for different beam incident angles

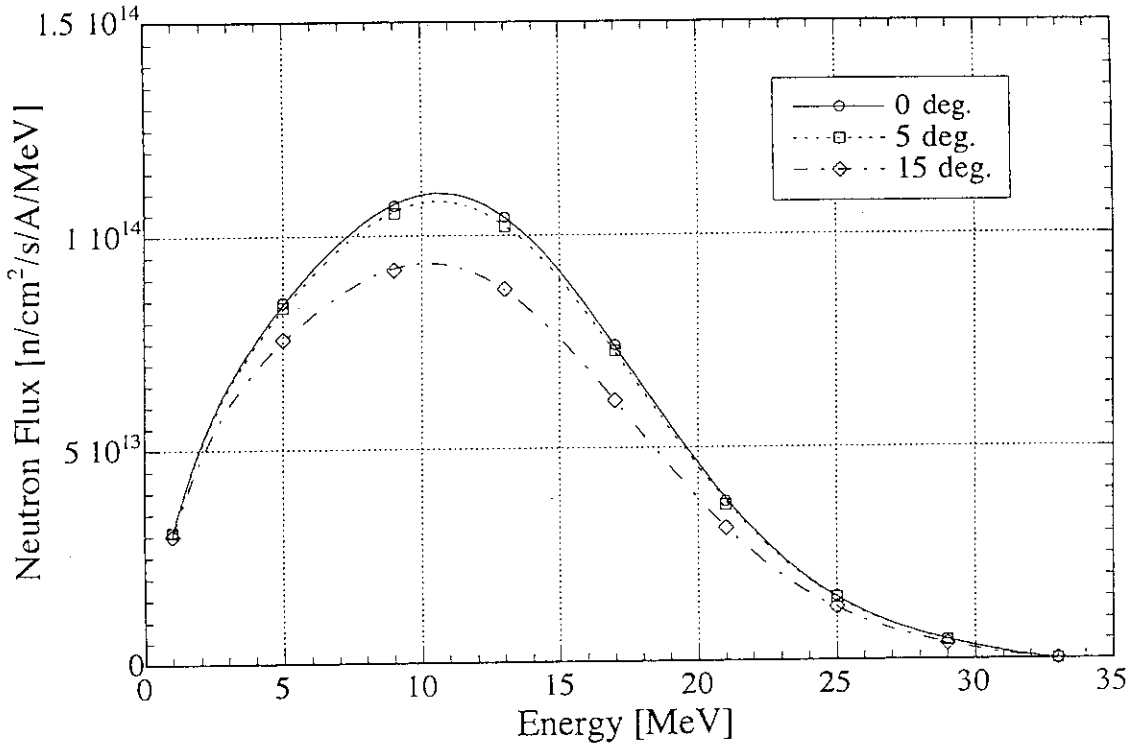

Fig. 2.2.9 Neutron spectra at 10 cm on z axis for different beam incident angles

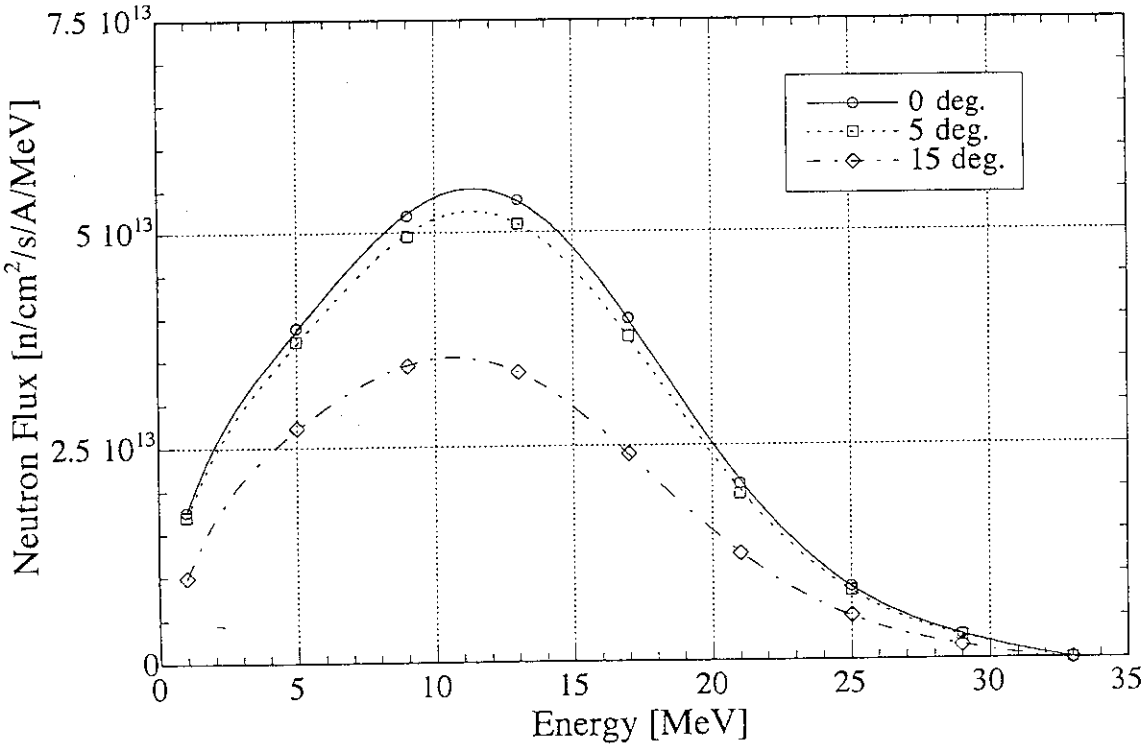

Fig. 2.2.10 Neutron spectra at 20 cm on z axis for different beam incident angles

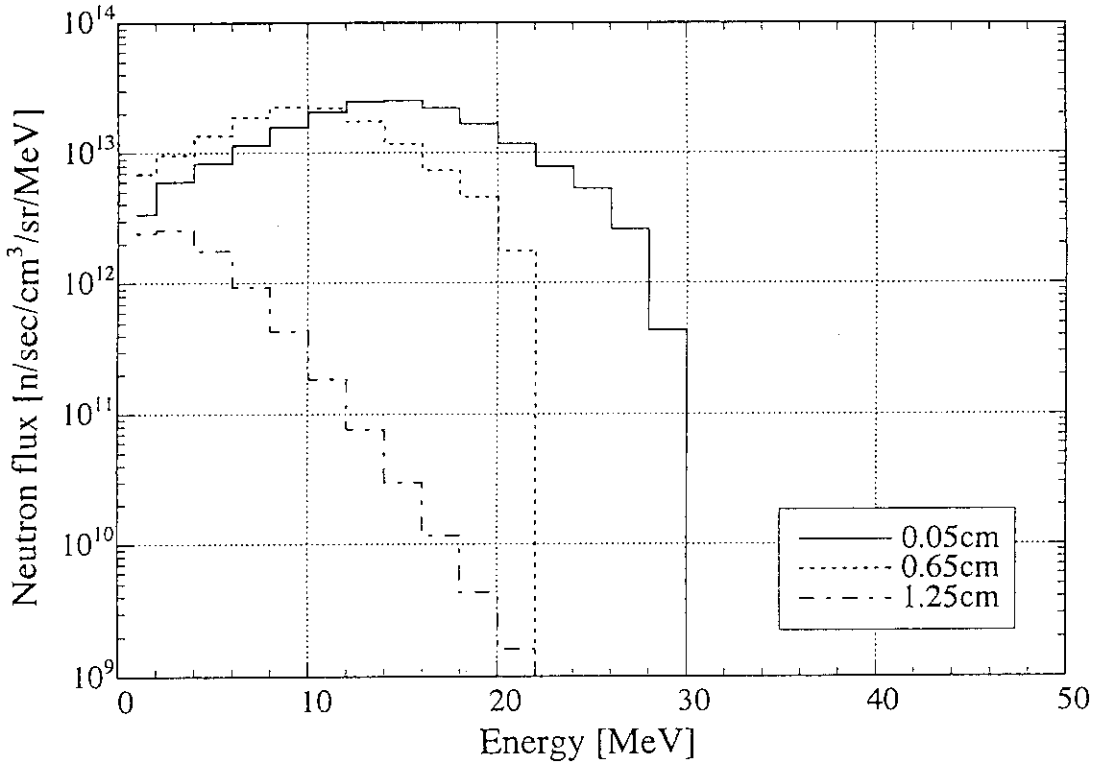

Fig. 2.2.11 Neutron spectra emitted from the different depth inside the Li-target layer between 0 and 5 degrees of polar and azimuthal angles for 30 MeV deuteron

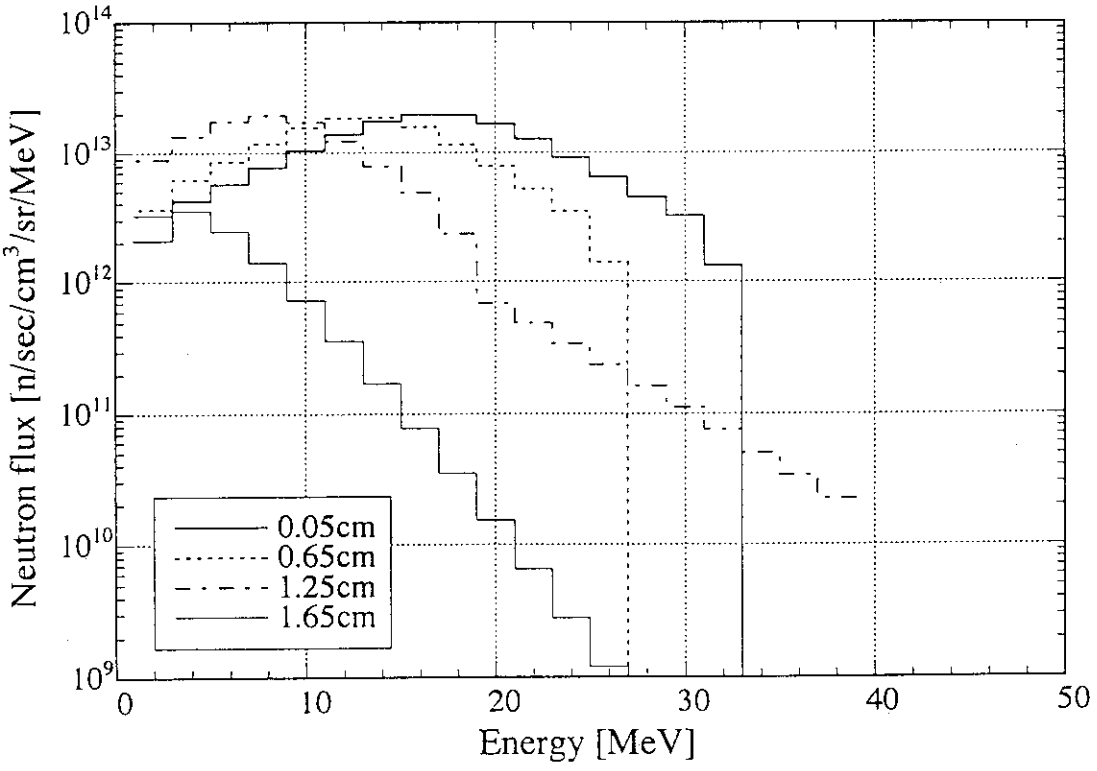

Fig. 2.2.12 Neutron spectra emitted from the different depth inside the Li-target layer between 0 and 5 degrees of polar and azmuthal angles for 35 MeV deuteron

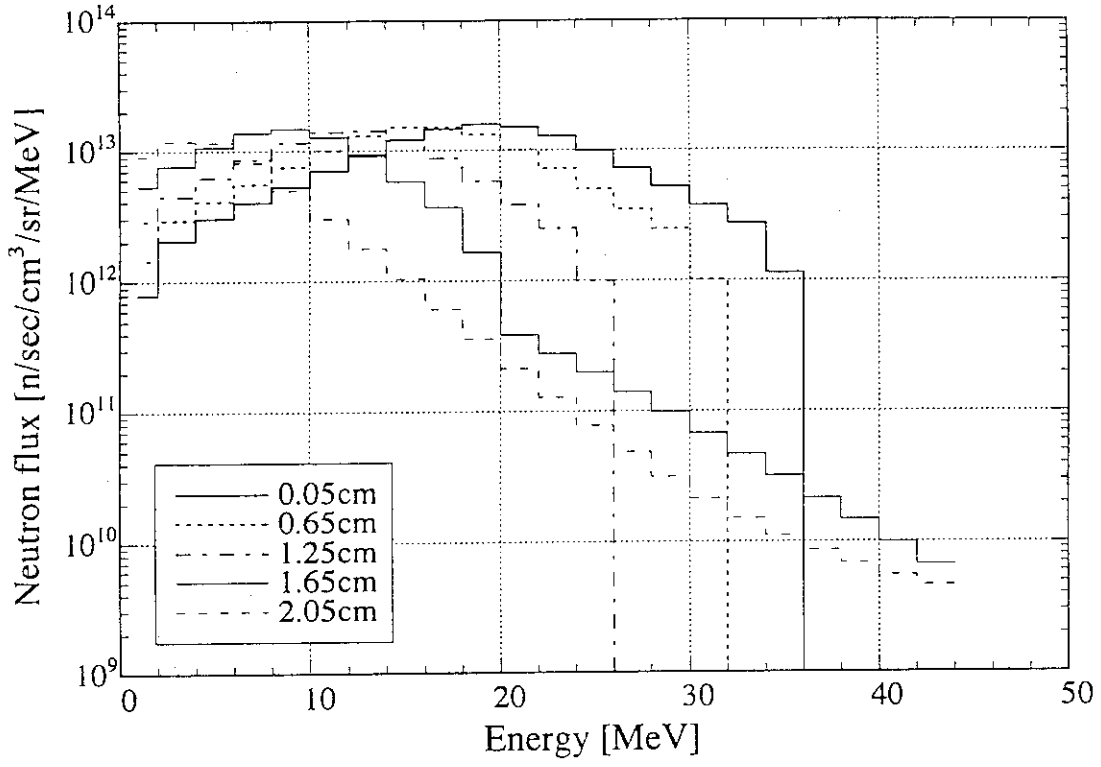

Fig. 2.2.13 Neutron spectra emitted from the different depth inside the Li-target layer between 0 and 5 degrees of polar and azmuthal angles for 40 MeV deuteron

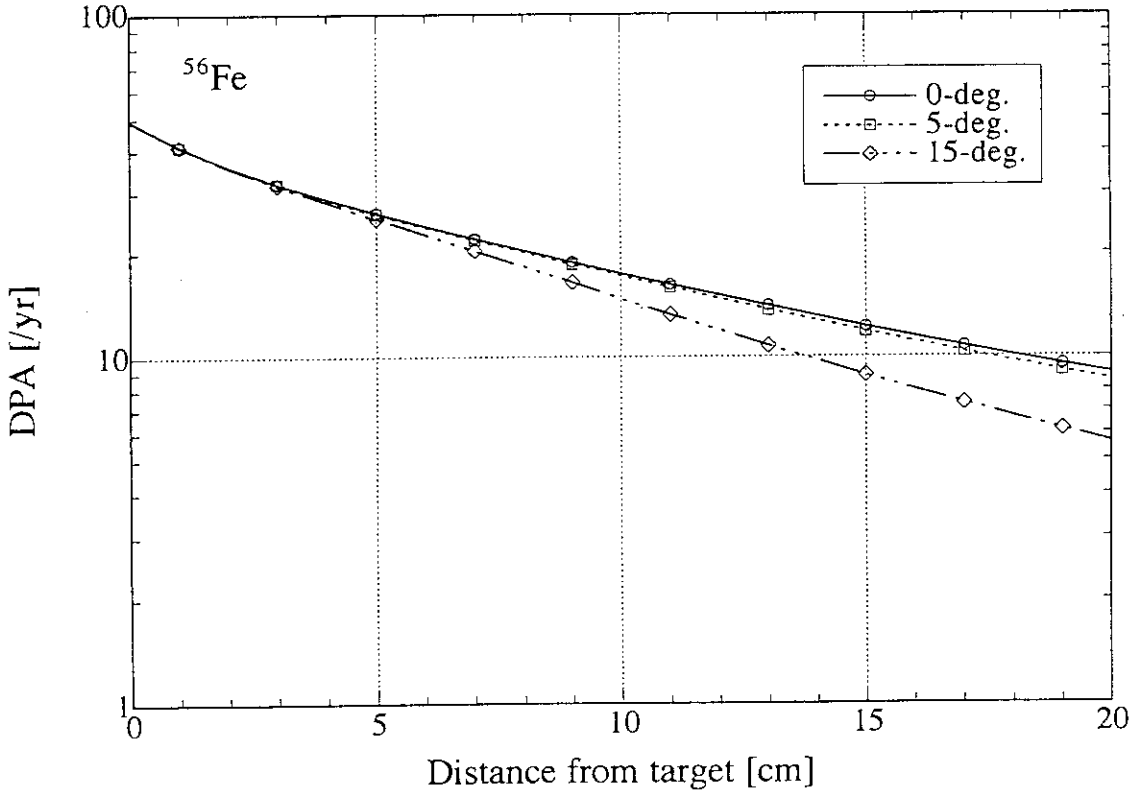

Fig. 2.2.14 Spatial distribution of dpa rate on z-axis for different beam incident angles

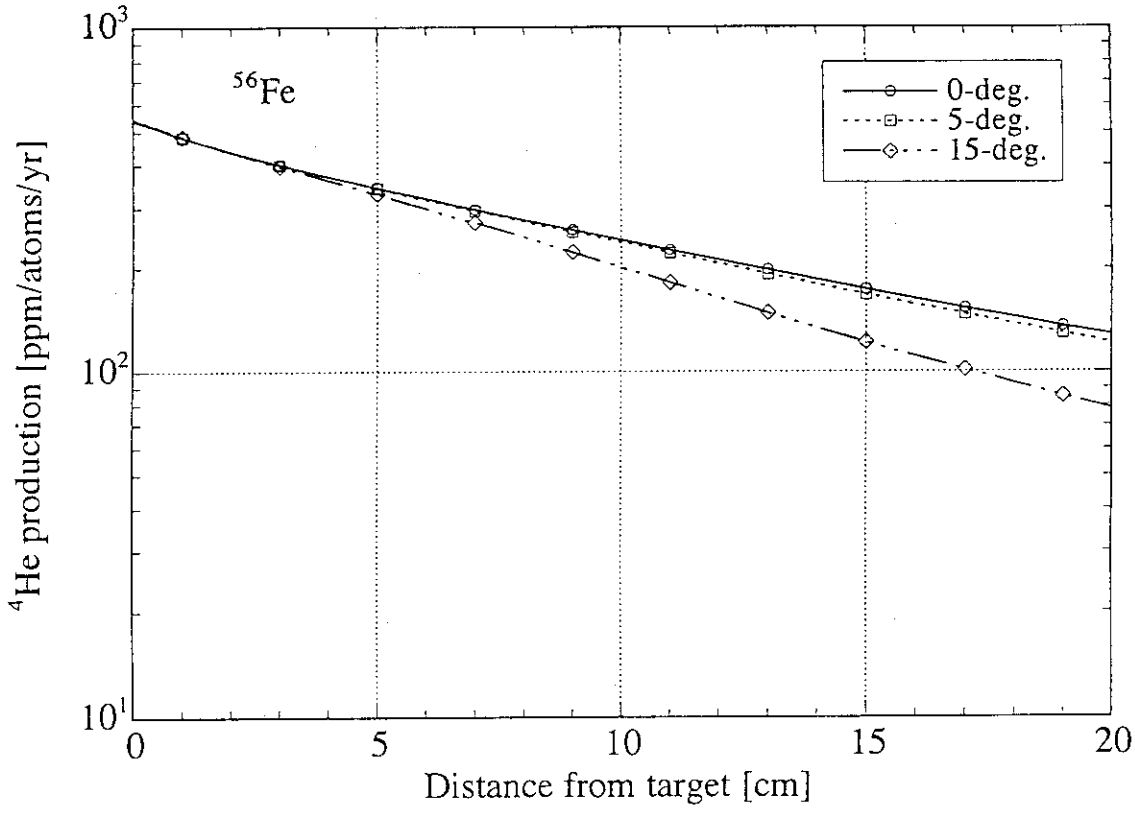

Fig. 2.2.15 Spatial distribution of He production rate on z-axis for different beam incident angles

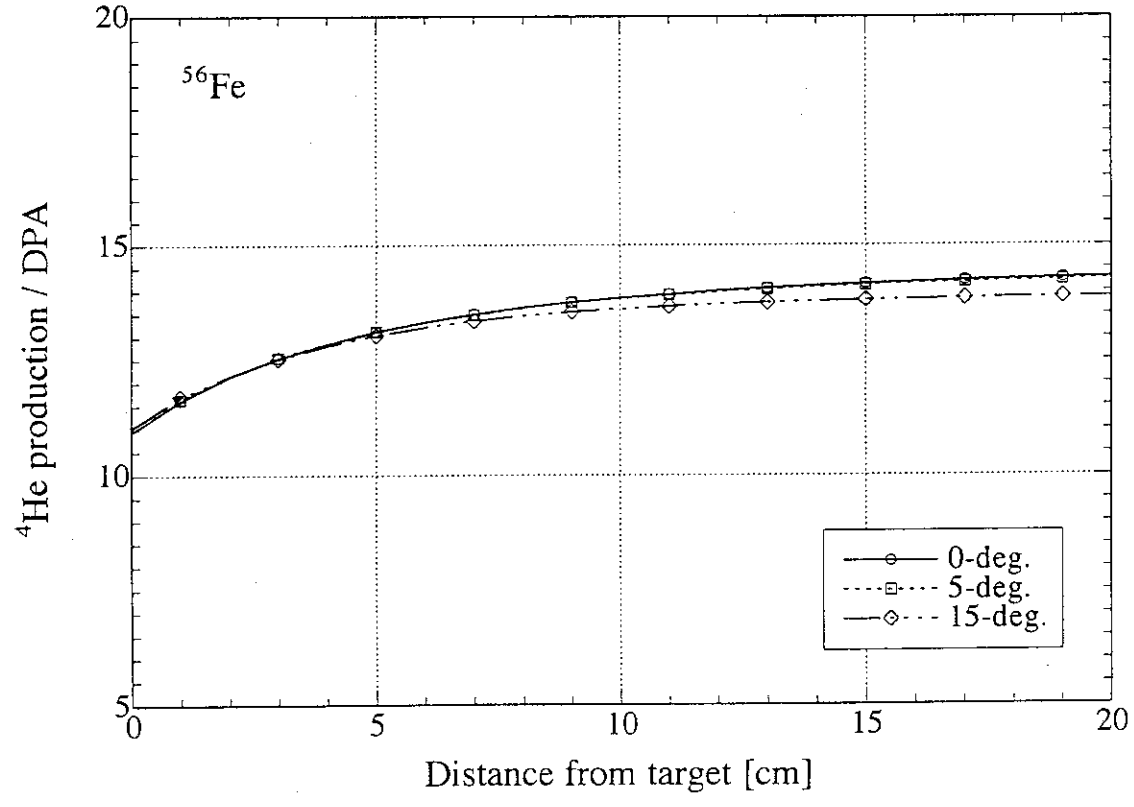

Fig. 2.2.16 Spatial distribution of He/dpa ratio on z-axis for different beam incident angles

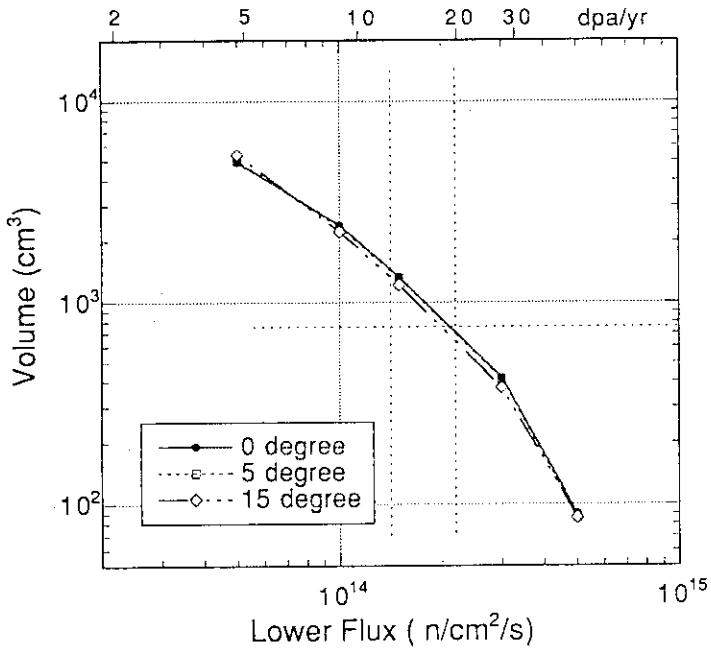

Fig. 2.2.17 Volume with the specific neutron flux attainable in irradiation

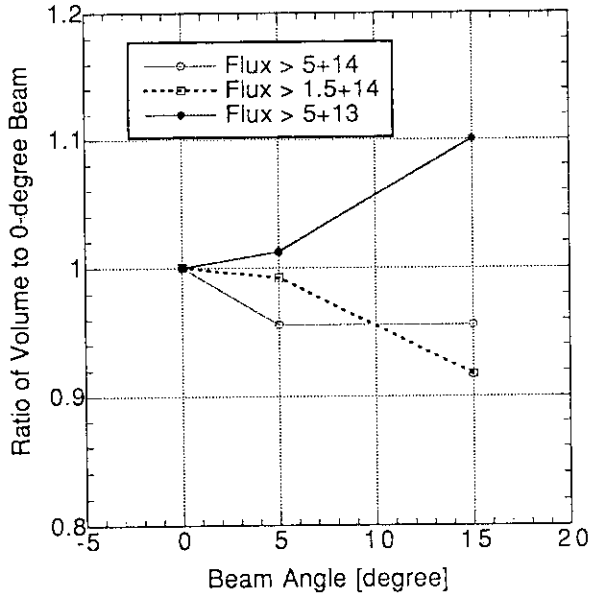

Fig. 2.2.18 Effect of beam angle on irradiation volume

Table 2.2.1 Spatial gradient of dpa and He production distribution (Ed=35 MeV, 10 cm x10 cm foot print)

DPA on Z-axis

Beam angle (degree)	Z= 2 cm	Z= 10 cm	Z= 15 cm	Z= 20 cm
0, 5	13%	9.3%	7.5%	6.7%
15	13%	11%	11%	9.7%

He production on Z-axis

Beam angle (degree)	Z= 2 cm	Z= 10 cm	Z= 15 cm	Z= 20 cm
0, 5	9.2%	7.5%	6.8%	6.4%
15	9.9%	9.4%	10%	9.6%

3. Irradiation Characteristics of Test Modules with Standard Loadings

Quantitative estimation of the spatial volume to be able to used in the IFMIF irradiation field is required for the four standard loading samples with different cooling materials. The reference conditions of the IFMIF deuteron beam and Li target configuration for examination are 1) 250 mA and 35 MeV for deuteron beam current and energy, respectively, and 2) the two 125 mA beam injection to the target with angle of 20 degrees (10 degrees from the center axis) as determined by the previous section.

3.1 Standard Loading Module

Four standard loading configurations were specified as follows:

for iron sample,

1) Fe 50%, He (and Void) 50%,

2) Fe 50%, NaK 30%, Void 20%,

and for SiC sample,

3) SiC 50%, He (and Void) 50%,

4) SiC 50%, NaK 30%, Void 20%.

The test matrices are packed in the module with the standard loading were averaged by the volume fraction and homogenized. The estimated parameters are calculated for the element of 100 % density. The module was placed at 2 mm from the target surface where the backwall thickness of 1 mm and the Li thickness margin of 2 mm for the deuteron range of 19 mm in Li for 35 MeV deuteron were assumed. The module size was 20 % bigger than the target area and the module depth was 200 mm for the 50 mm x 200 mm target, the 60 mm x 240 mm x 200 mm matrix is placed. The atomic number density of loading samples, i.e., Fe and SiC, and coolant, i.e., NaK are given in Table 3.1.1.

3.2 Neutronics Calculation

Neutronics calculation was performed using the Monte Carlo neutron transport code, GMVP[11], that was vectorized from MORSE-CG[12]. The nuclear data library used is HILO86/J3[13] that was modified from HILO86[14] by replacing the data below 20 MeV by JENDL-3.1[15] with self shielding factor. The test matrix was divided into 20 mm cubics, which corresponds 360 cubics for the 60 mm x 240 mm x 200 mm module, and each cubic was assigned to track length cell detector, as shown in Fig.3.2.1. On the other hand, for dpa-volume relation of only 60 mm x 240 mm x 200 mm case, the detailed analysis was also applied using fine model shown in Fig. 3.2.2. The irradiation volume above the desired flux or dpa rate was estimated by counting these cubics. These cubics are divided to more fine matrix for the detailed analysis for the irradiation volume to obtain better accuracy as described in the further section.

Nuclear responses below 20 MeV was processed by FAIR-CROSS/T[16] from JENDL-3.1 and those above 20 MeV such as He production and transmutation production cross sections are processed by FAIRCROSS/X from the newly evaluated cross sections which is prepared for the JENDL High Energy File. The gas production cross section for ^{56}Fe is shown in Fig. 3.2.3. The dpa cross section of natural Fe, Si, and Carbon above 20 MeV were calculated from displacement KERMA factors which were extrapolated from the data of JENDL-3.2[17] below 20 MeV as shown in Fig. 3.2.4-6. The dpa cross section is given as

$$\sigma = 0.8\frac{T_D}{2E_D},$$

where T_D is displacement KERMA and E_D is displacement energy. The used displacement energies were 40 eV for Fe and 25 eV for the others.

The source function providing energy spectrum, angular distribution and intensity of neutrons emitted from Li target were given by the method described in the previous section. The source function was expressed as distribution source over the deuteron stopping range.

3.3 Effect of Beam Foot Print Shape[18]

First the effect of the beam shape (foot print of the beam) on the irradiation volume i.e., on the volume in which the required flux can be obtained, and field gradient were examined. Three beam shapes are examined: 100 mm x 100 mm, 50 mm x 200 mm and 25 mm x 400 mm squares as shown in Fig. 3.3.1. From the viewpoint of Li flow, 25 mm x 400 mm is the best because of the shortest free flow distance. Since the irradiation condition is the highest priority, these three shapes were compared with volume and gradient.

Figures 3.3.2-4 shows the flux contour map for the test module with Fe 50 % and NaK 30 % and for each shape. Figures 3.3.5-7 show also the flux contour for the case without modules, corresponding to each shape. The flux gradient of the cases was compared each other in Figs. 3.3.8 and 3.3.9, for without and with the modules. The flux gradient of the squared shape without the module is the most modest and almost 10 %/cm which is requirement from the user. In Fig. 3.3.9 shown for various loadings, most of the case is close to 15 %/cm for the 50 x 200 mm shape, although the 100 x100 mm shape is not different but the 25 x 400 mm shape is worse. It can be concluded from the figure that the gradient of 10%/m could not be achieved in the module.

Table 3.3.1 also shows the space volume giving the neutron flux above specific level. In practical, the neutron flux of 5×10^{14} n/cm^2/s is attainable maximum limit for the irradiation. For the 25 x 400 mm case, however, this limit could not be reached. It can be pointed out that the case with Fe sample loading increases the volume of higher neutron flux region in comparison with the case without samples. Table 3.3.2 summarizes the space volume giving the dpa rate above specific value for various combinations of beam foot print

shape and loadings. From the table, for 50 x 200 mm target, only 0.3 litter of the volume is obtained for a region over 20 dpa, and a 300 mA of deuteron beam current is required for Fe loading matrix to exceed 0.4 litter. It is also pointed out that the space volume of attainable dpa in the higher dpa region does not increase by material samples in contrast to the neutron flux case. This is because the dpa is contributed by higher energy neutrons and neutron spectrum is changed to the lower by materials.

3.4 Detailed Analysis for Volume of Irradiation Space

The test module model was divided more precisely as shown in Fig. 3.2.2 for the detailed analysis of the volume-dpa relation. The deuteron energy was also changed to see the increase of the volume. Table 3.4.1 summarizes the results of the volume-dpa relation. In the table, the original means the calculation by the model shown in Fig. 3.2.1. There is a little difference between the rough and detailed models. The difference is less than 5 %. For the energy dependence of the volume above 20 dpa level, the volume increases from 0.3 litter to 0.5 litter with increase of the energy of 35 to 40 MeV. Therefore, the volume requirement can be satisfied by the 40 MeV acceleration. These are consistent with the results by the US team.[19]

Figures 3.4.1 and 3.4.2 show the contour graphs of the desired limit of dpa rate for the 35 MeV incident energy case, and Figs. 3.4.3 and 3.4.4 are for the 40 MeV. Figs. 3.4.5 and 3.4.6 are of SiC for 35 MeV. There is no difference seen in the contour maps for both energies and configurations of Fe 50% and Fe 50% + NaK 30%. This means NaK coolant has a negligible effect in gloss behavior of neutrons. For SiC, low dpa of C is due to the low dpa cross sections in extrapolated energies.

3.5 Gas production and Nuclear Heating

For gas production, He production rate was calculated inside the module. The energy dependence of He production cross section is rather flat seen in Fig. 3.2.3, while the dpa cross section increases with the energy. Therefore, the dpa at the front of the module is higher than that of the back end. This causes lower He-production to dpa ratio as the same as in the free space shown in Fig. 2.2.16. However, at the middle of the module this ratio is close enough to the fusion condition such as the ratio of 14. Table 3.5.1 summarizes average dpa, He production rates and He/dpa value. The average values of both dpa and He production rates decrease with decrease of height of the beam foot print, but the ratio of them does not change much.

Nuclear heating in the standard sample loading was calculated and the results are summarized in Table 3.5.2. For iron sample, the gamma-ray heating is 50 % larger than neutron heating, and for SiC sample, the gamma-ray heating is one tenth of neutron heating. However, total heating is almost the same for both samples and that is around 20-23 W/cm^3

at maximum. The average heating is about half of the maximum.

3.6 Transmutation and Radio-activity

Nuclear transmutation was calculated by the TRANSM code[20] using effective one group cross sections reduced with averaged neutron spectra inside the module. The TRANSM code includes a decay data library and calculates time dependent nuclei production and disappearance, and decay chain. Figures 3.6.1 and 3.6.2 summarize the number of nuclei mainly generated by 1000 days irradiation as a function of cooling time, for Fe-NaK, and SiC cases with the 50 x 200 mm beam shape.

For iron, main contributions are ^{55}Mn, H, He, ^{53}Cr, ^{53}Mn, ^{54}Cr, and ^{55}Mn. ^{55}Mn and ^{54}Cr increase with cooling time because of decay from ^{55}Fe and ^{54}Mn, respectively. The largest number of transmutants is ^{55}Mn from iron, and the second one is hydrogen and the third is helium. For SiC, the largest is hydrogen, and the next is helium, and followed by ^{24}Mg, ^{25}Mg and ^{26}Mg. For SiC, He production is larger than the iron.

Radio-activities produced inside the module were also estimated by collecting from transmutants. Figures 3.6.3 and 3.6.4 show radio-activities produced by 1000 days irradiation, for iron and SiC modules. The main activities in iron are ^{55}Fe (electron capture, $T_{1/2}$=2.73y), ^{54}Mn (electron capture, $T_{1/2}$=312.2d), ^{49}V (electron capture, $T_{1/2}$=330d), and ^{56}Mn (β^- decay, $T_{1/2}$=2.6h). However, electron capture is not concerned for radiation protection. For SiC, activity level is very low, and only ^{26}Al (β^+ decay, $T_{1/2}=7\times10^5$y) and ^{22}Na (β^+ decay, $T_{1/2}$=2.6y) are concerned.

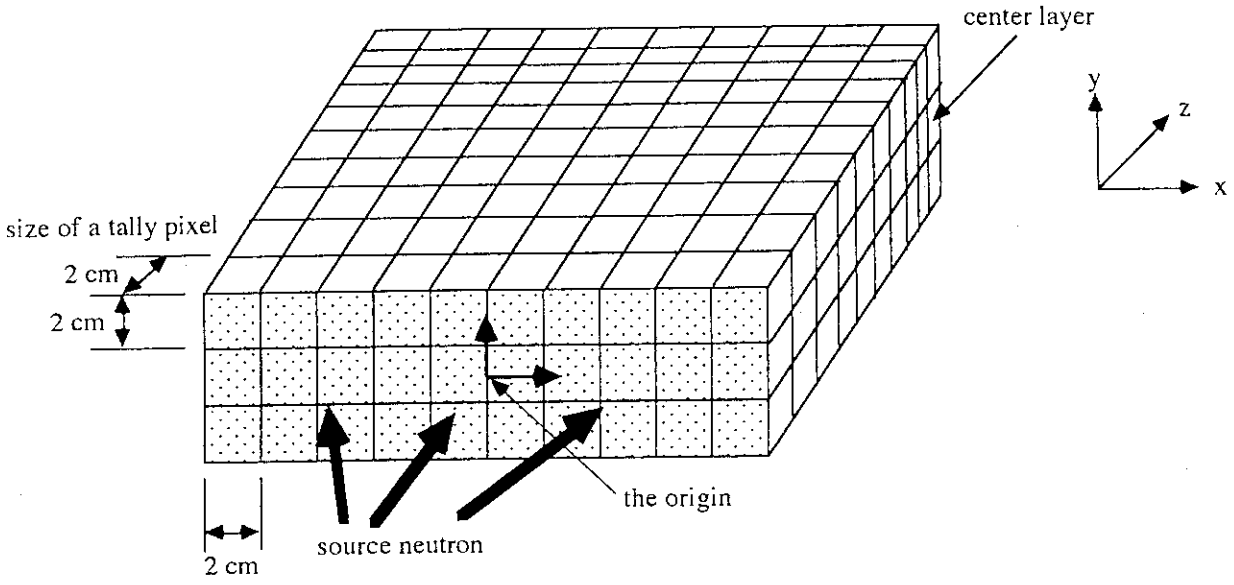

Fig. 3.2.1 Arrangement of tally cells in a irradiation test module for GMVP calculation (The calculated area is 24 cm x 6 cm and 20 cm in depth)

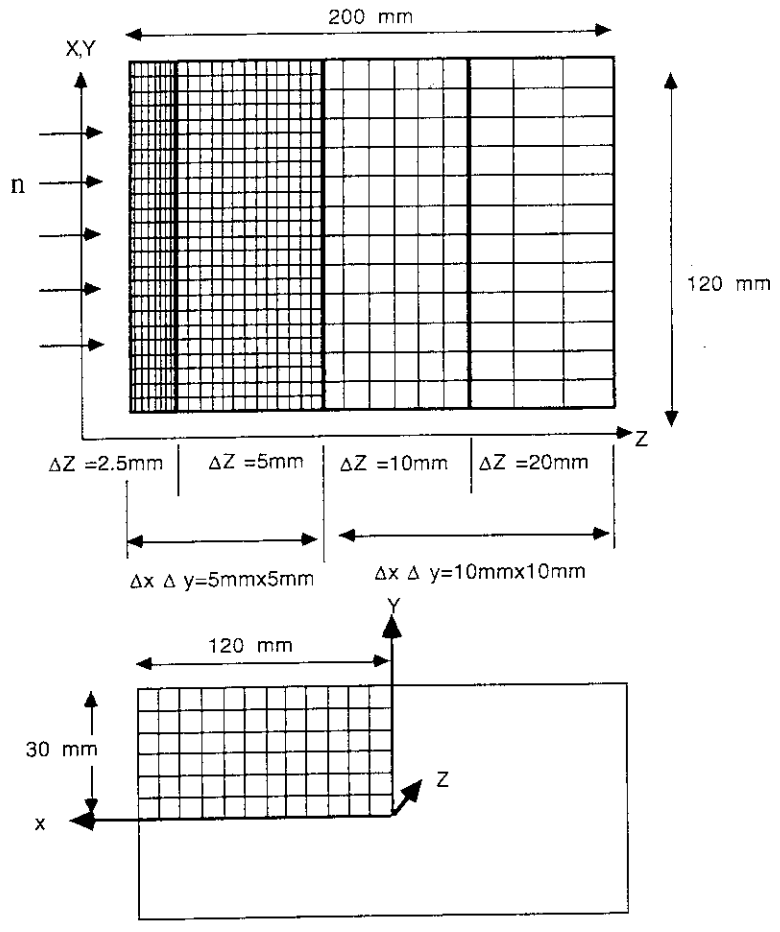

Fig. 3.2.2 Detailed mesh arrangement of tally cells with 1/4 symmetrical region in a test module

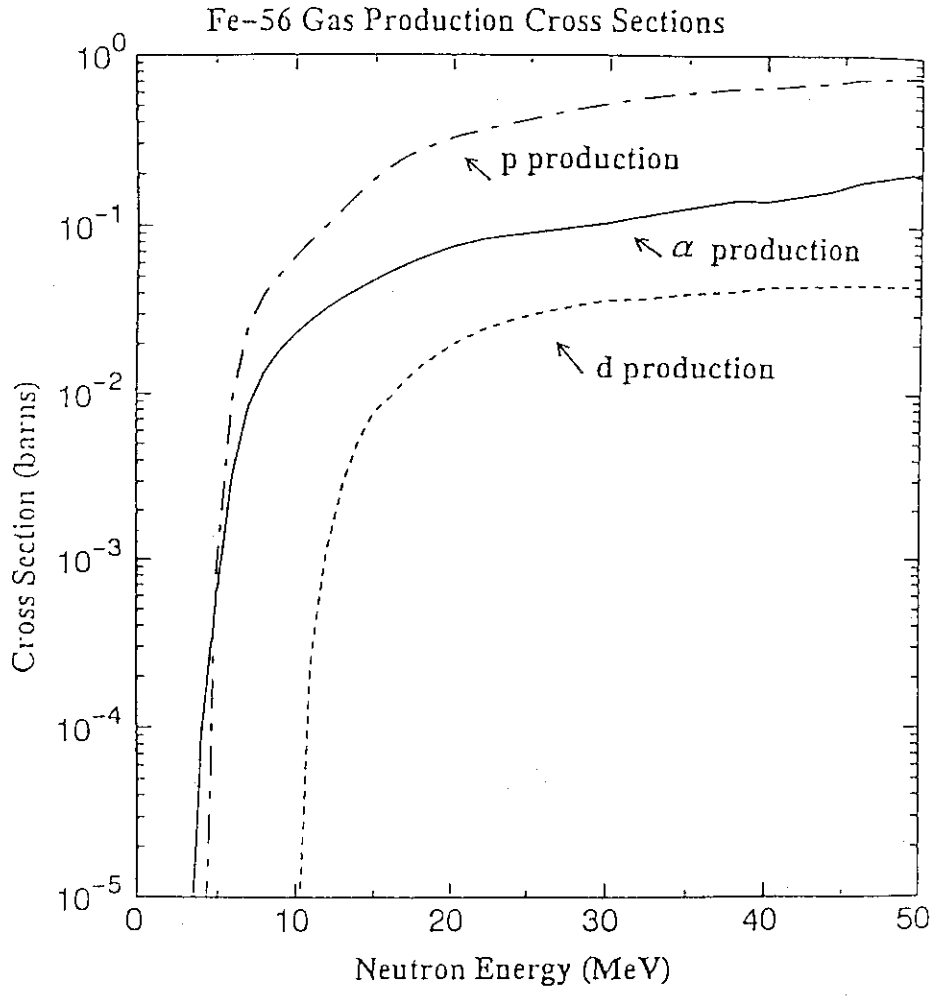

Gas production cross section of ^{56}Fe

Fig. 3.2.3 Gas production cross section used in the calculation above 20 MeV

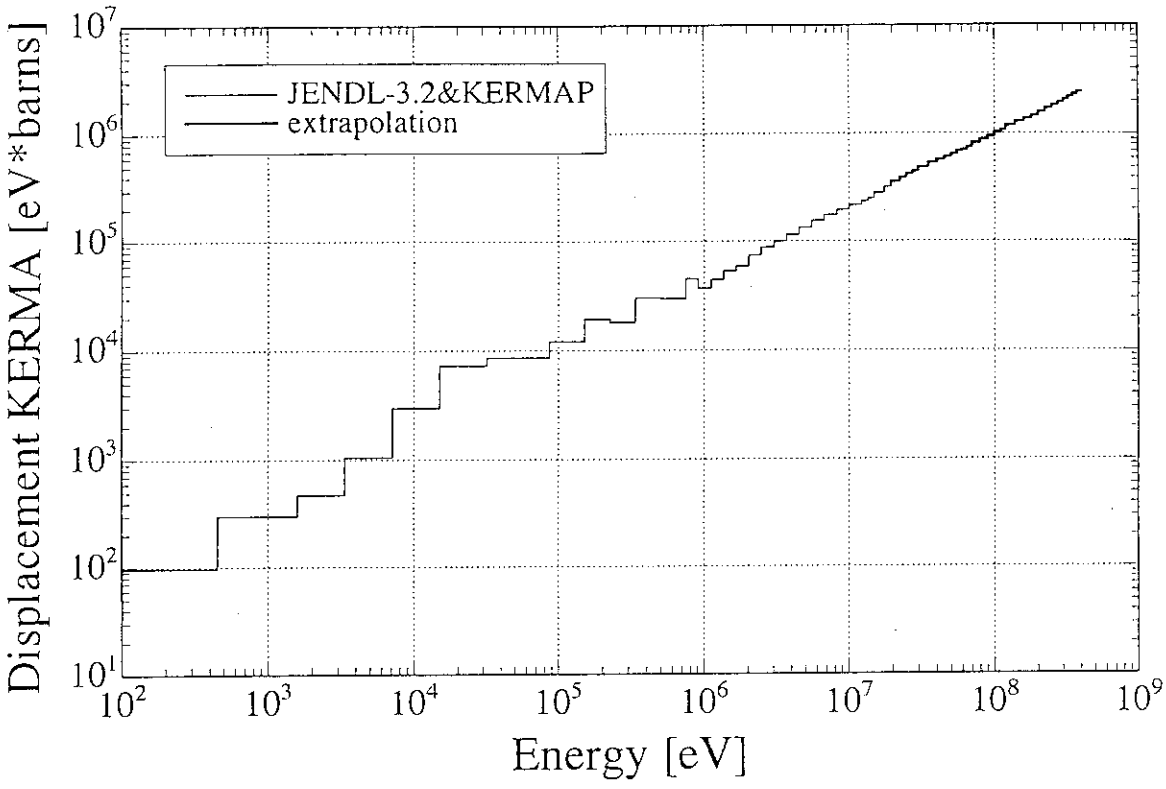

Fig. 3.2.4 Displacement KERMA of Fe used for dpa calculation up to 50 MeV

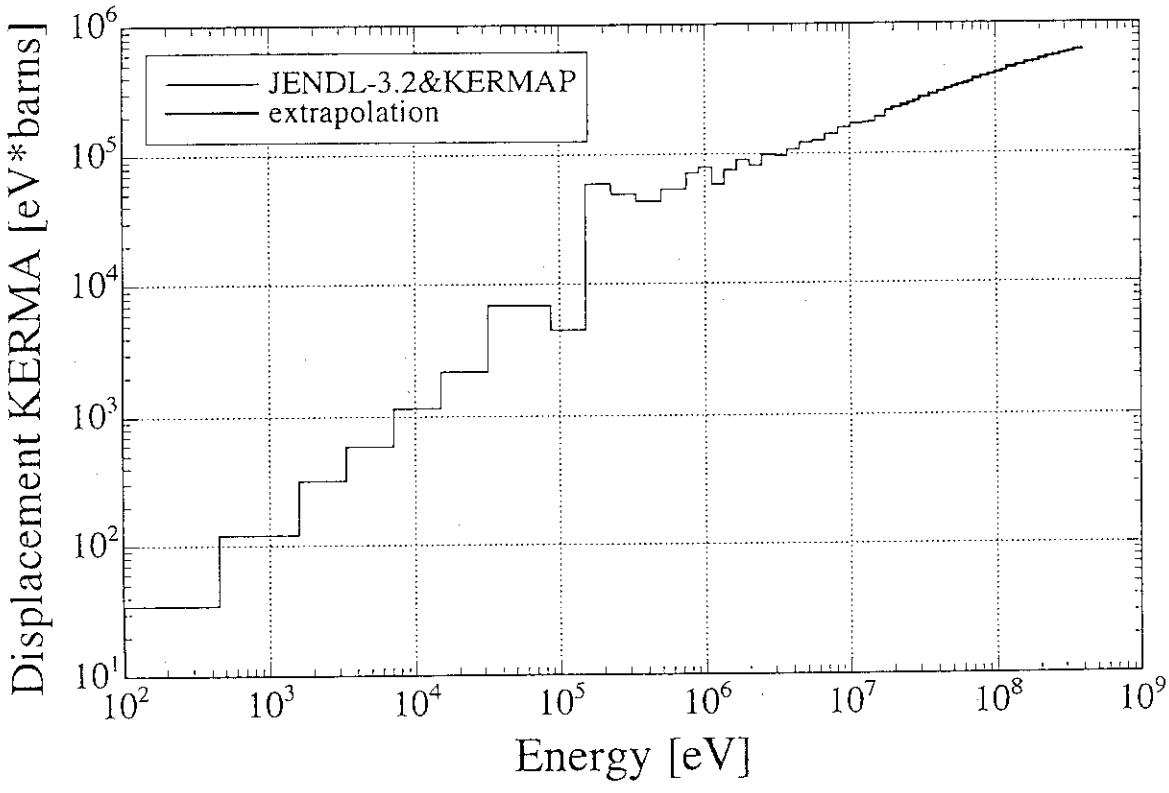

Fig. 3.2.5 Displacement KERMA of Si used for dpa calculation up to 50 MeV

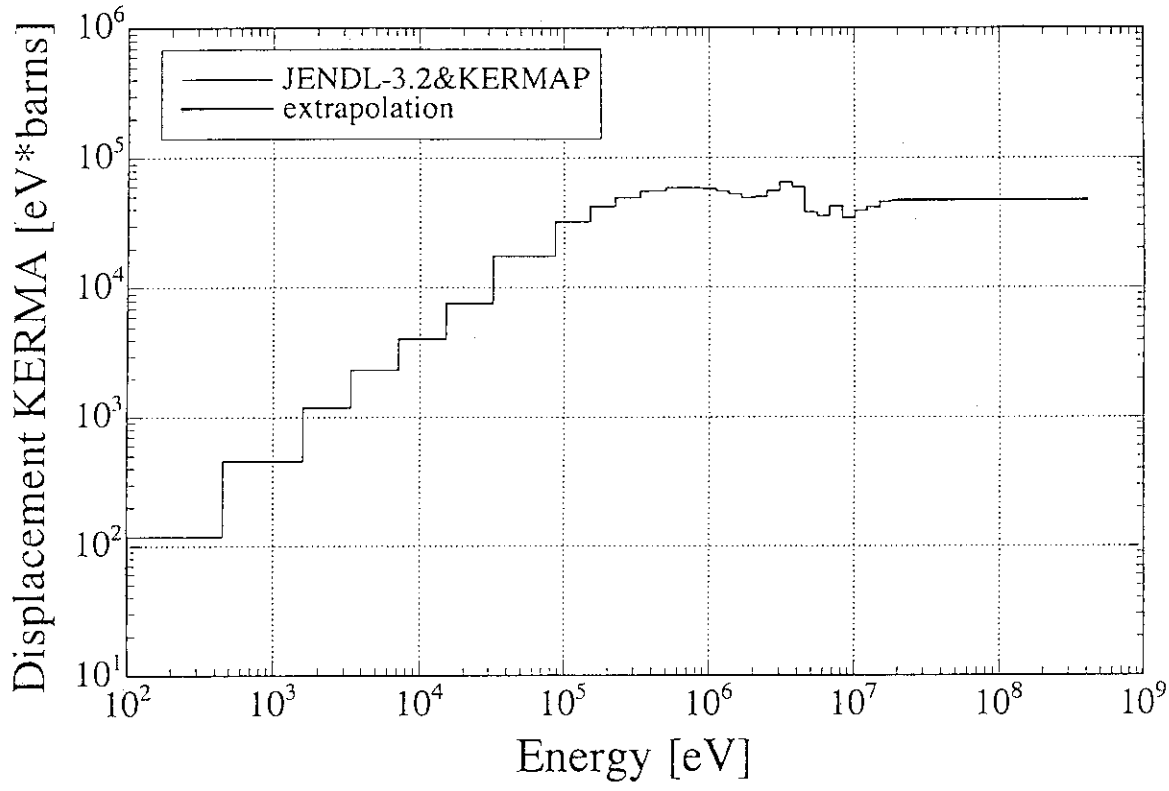

Fig. 3.2.6 Displacement KERMA of Carbon used for dpa calculation up to 50 MeV

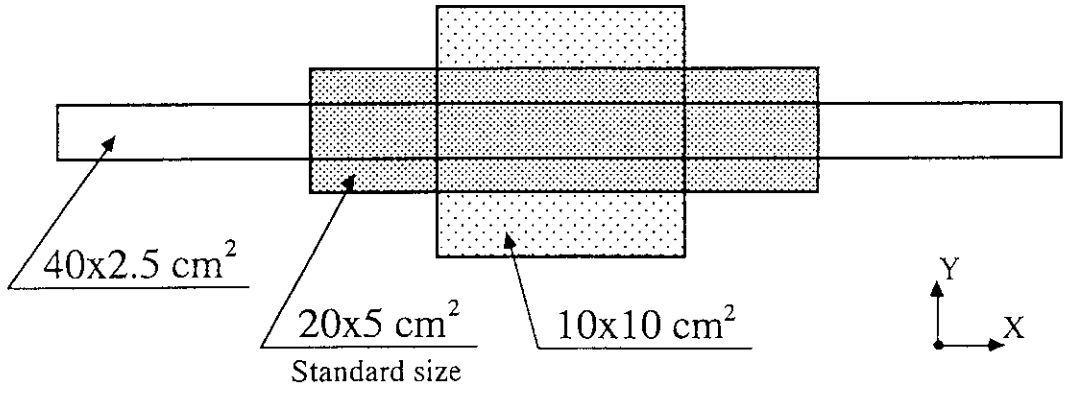

Fig. 3.3.1 Sizes of three beam foot prints of deuteron on the target surface

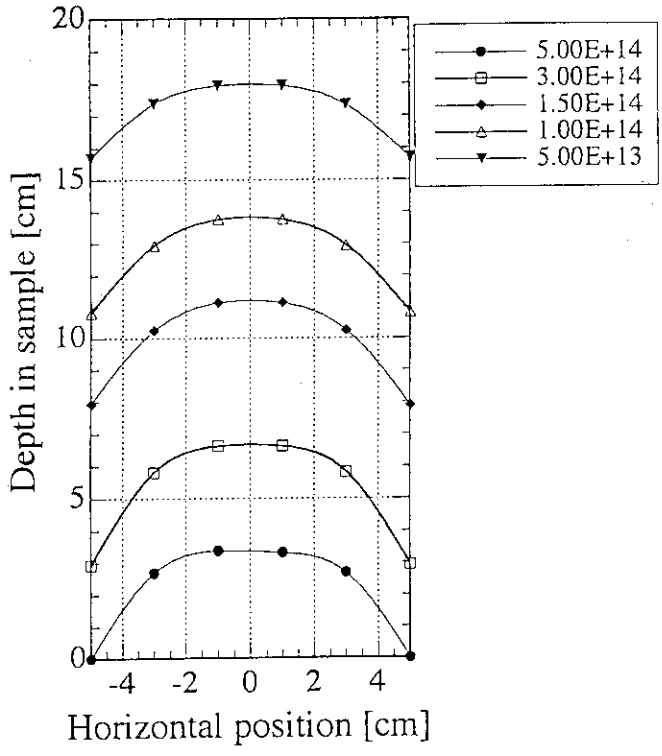

Fig. 3.3.2 Contour plot of neutron flux on the x-z plane inside the Fe 50% /NaK 30% test module for the case of 10 cm x10 cm foot print

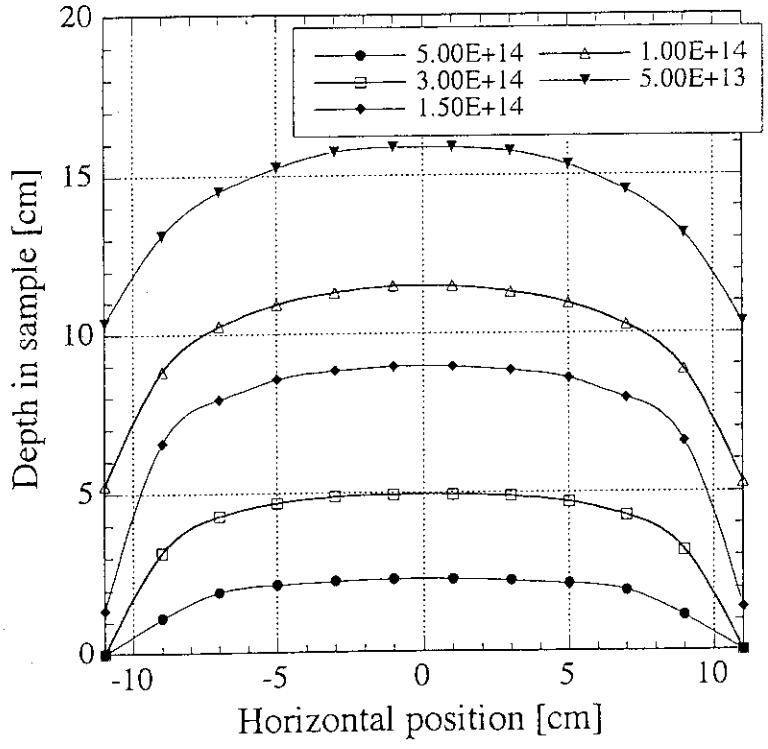

Fig. 3.3.3 Contour plot of neutron flux on the x-z plane inside the Fe 50% /NaK30% test module for the case of 5 cm x20 cm foot print

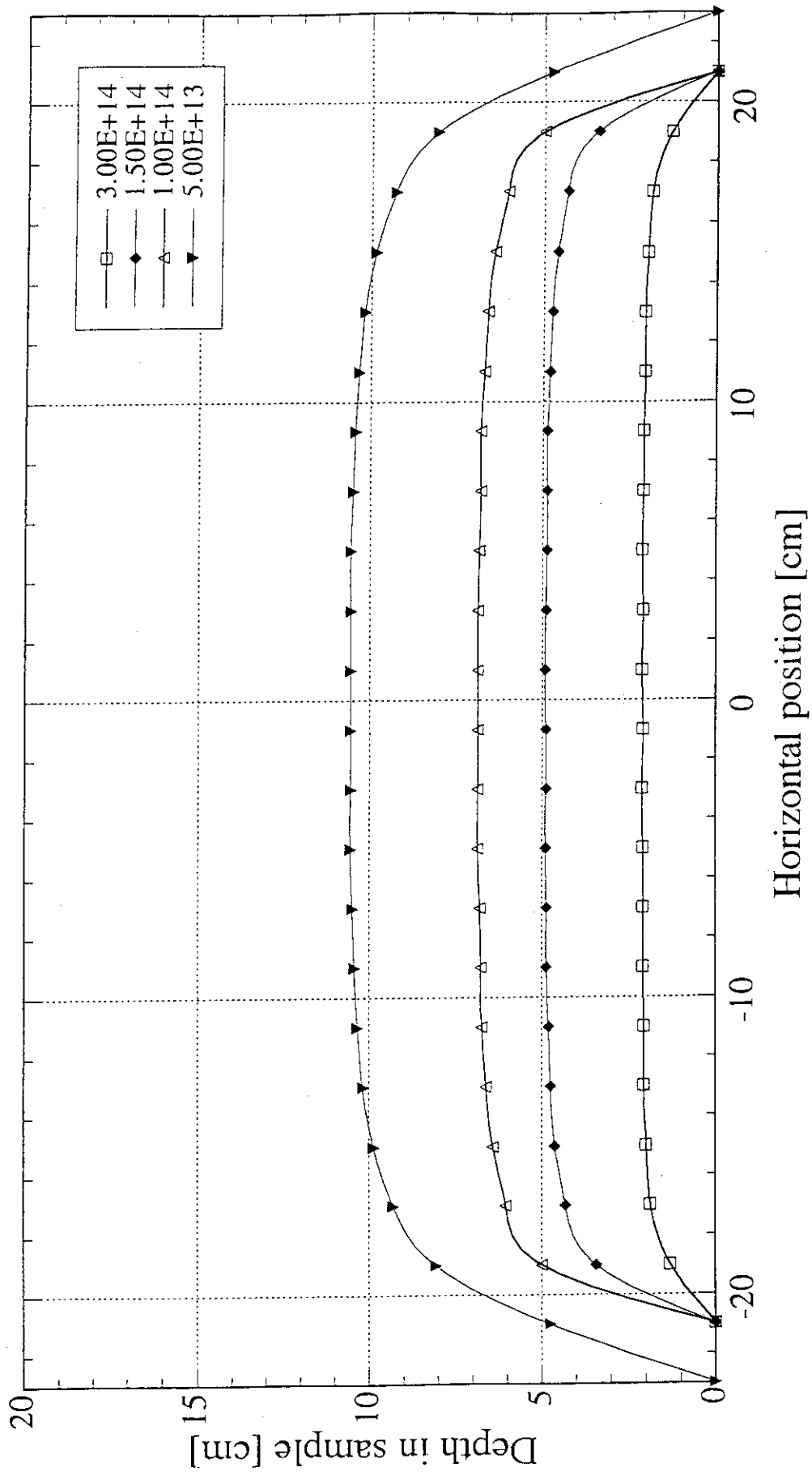

Fig. 3.3.4 Contour plot of neutron flux on the x-z plane inside the Fe 50% /NaK30% test module for the case of 2.5 cm x40 cm foot print

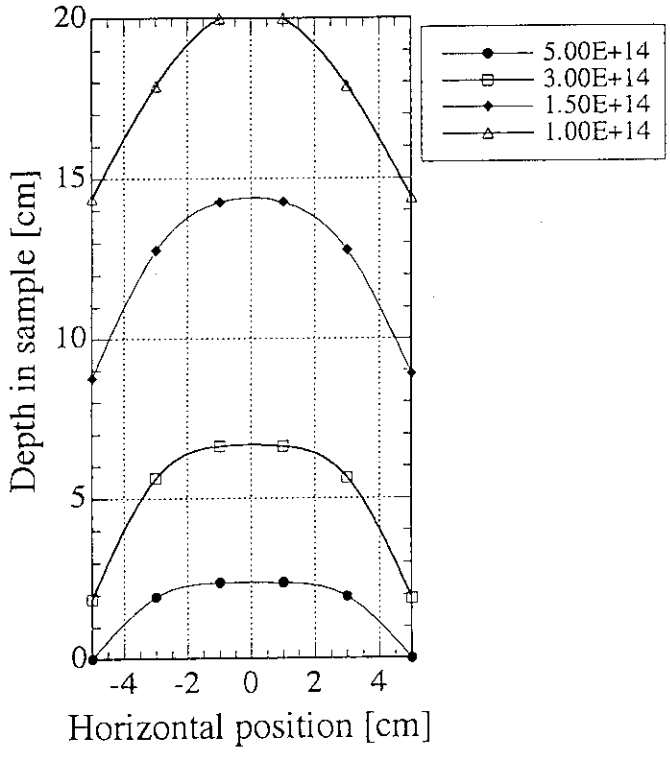

Fig. 3.3.5 Contour plot of neutron flux on the x-z plane without the test module for the case of 10 cm x10 cm foot print

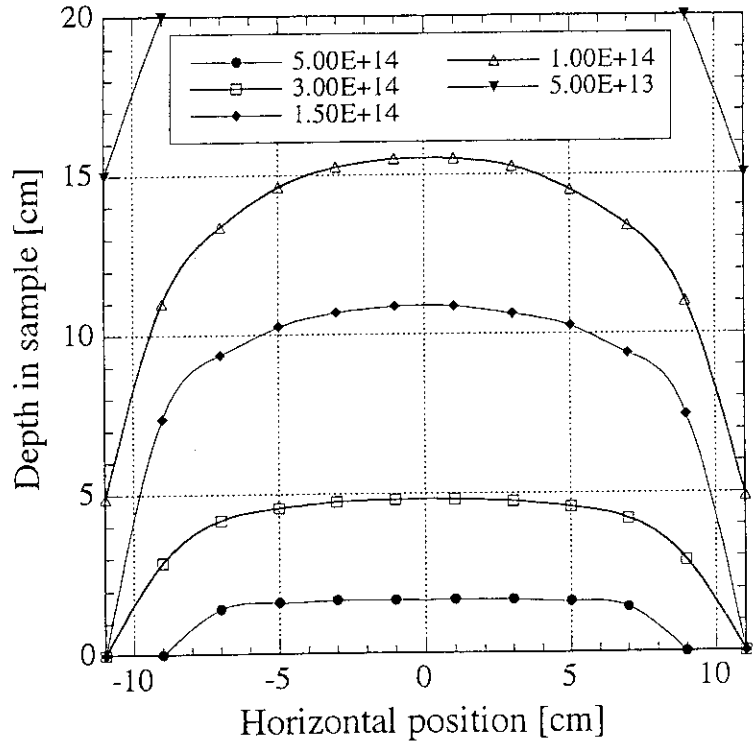

Fig. 3.3.6 Contour plot of neutron flux on the x-z plane without the test module for the case of 5 cm x20 cm foot print

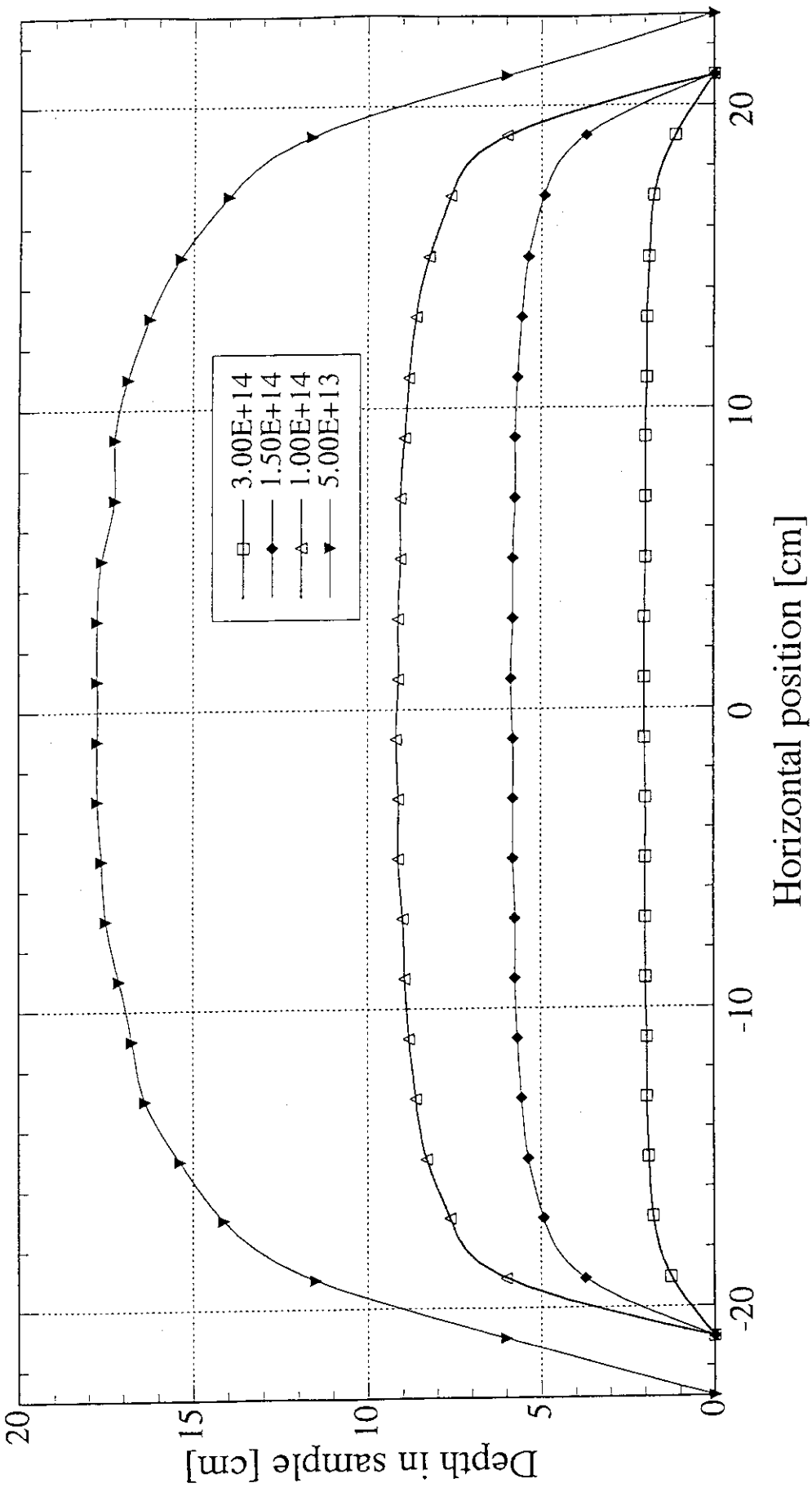

Fig. 3.3.7 Contour plot of neutron flux on the x-z plane without the test module for the case of 2.5 cm x40 cm foot print

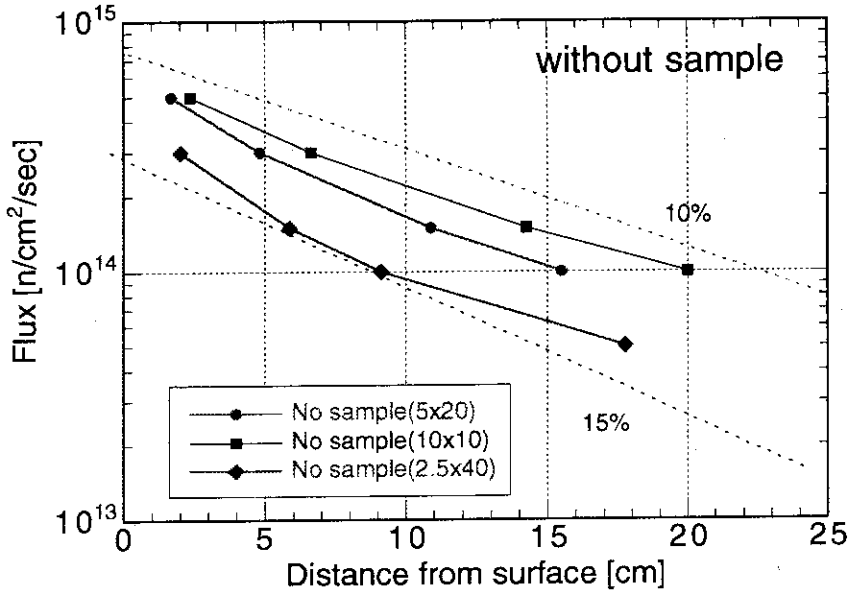

Fig. 3.3.8 Flux gradient on the z axis for three types of foot print without the module

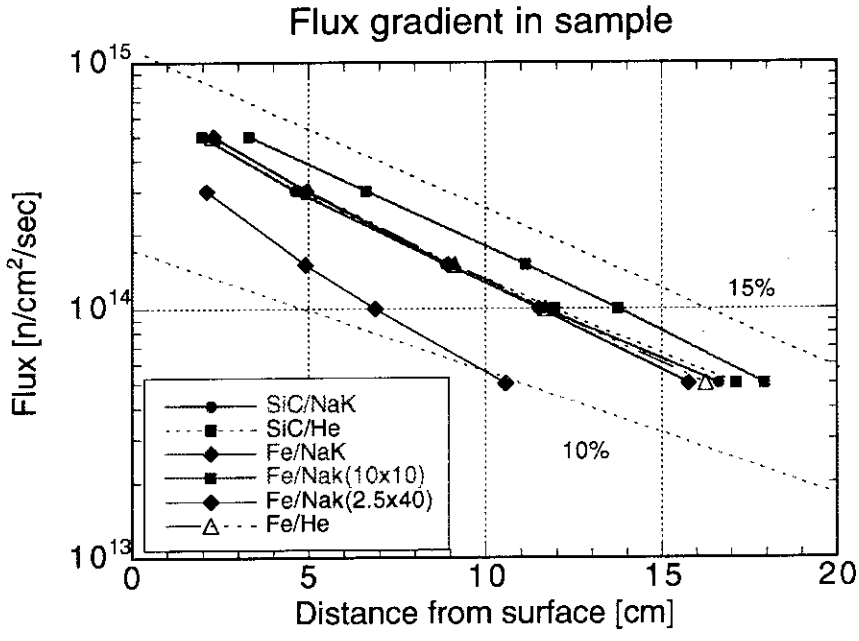

Fig. 3.3.9 Flux gradient on the z axis for three types of foot print and for the different test modules

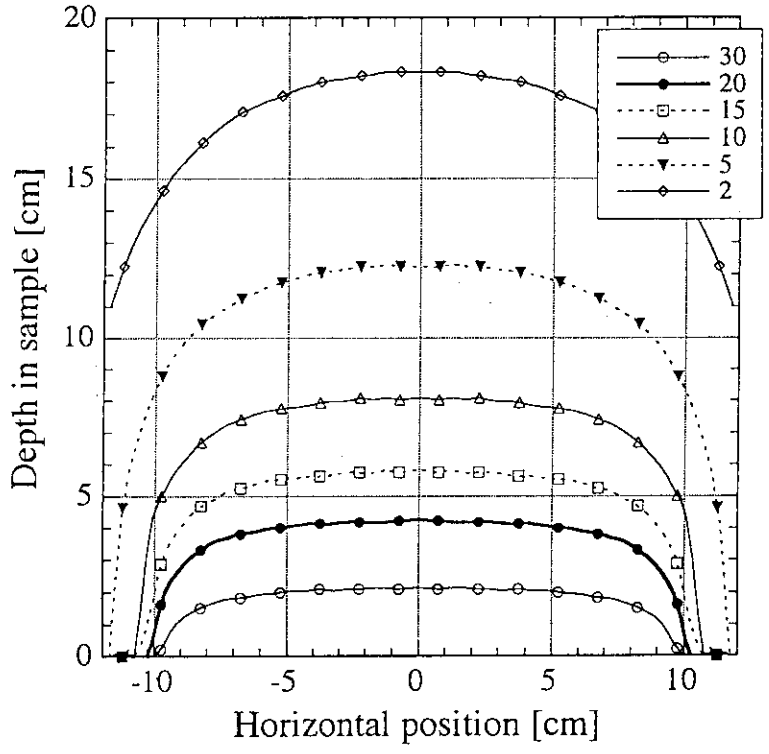

Fig. 3.4.1 Contour plot of dpa of Fe on x-z plane for the Fe 50%/NaK 30% module for 35 MeV and the foot print of 5 cm x 20 cm

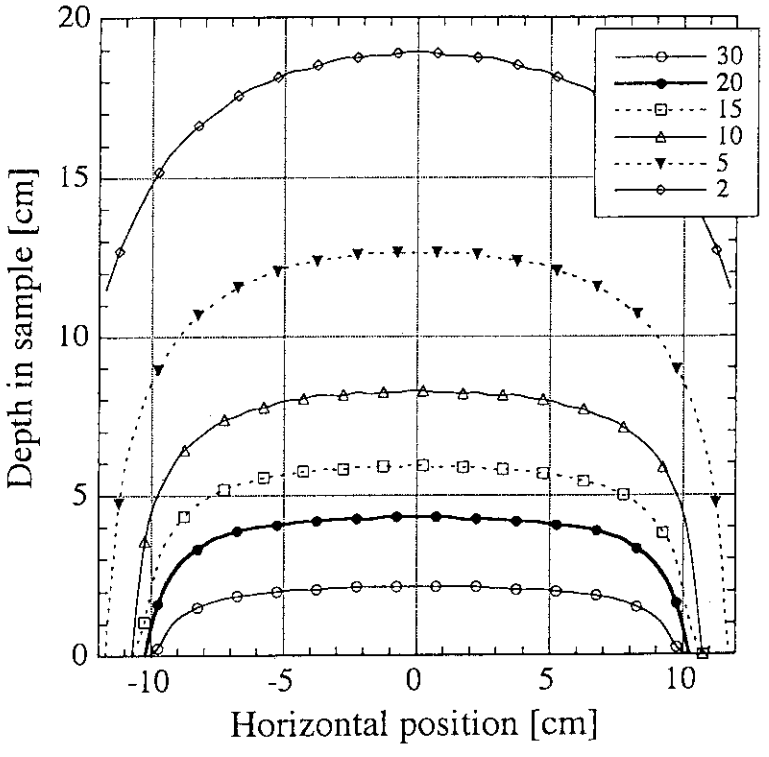

Fig. 3.4.2 Contour plot of dpa of Fe on x-z plane for the Fe 50%/He module for 35 MeVand the foot print of 5 cm x 20 cm

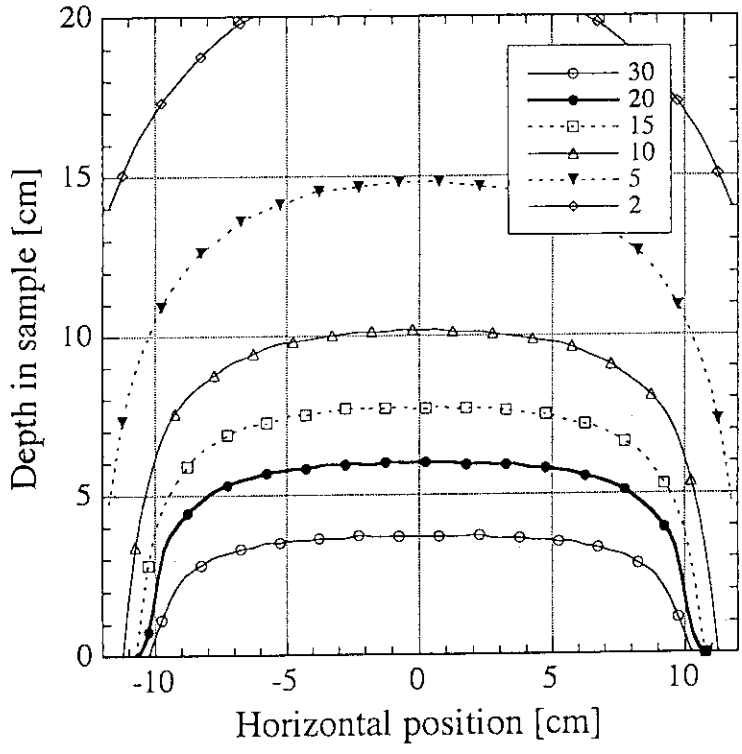

Fig. 3.4.3 Contour plot of dpa of Fe on x-z plane for the Fe 50%/NaK 30% module for 40 MeV and the foot print of 5 cm x 20 cm

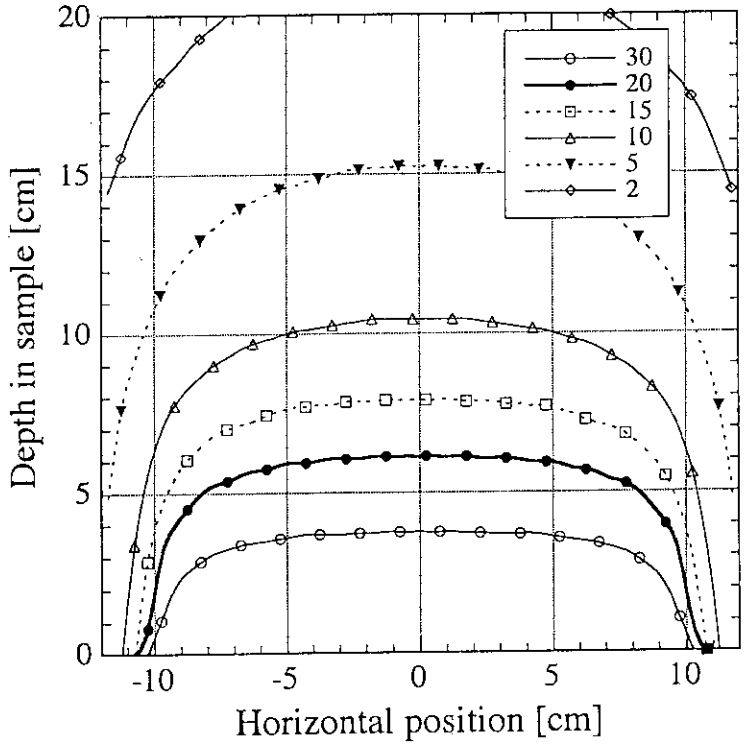

Fig. 3.4.4 Contour plot of dpa of Fe on x-z plane for the Fe 50%/He module for 40 MeV and the foot print of 5 cm x 20 cm

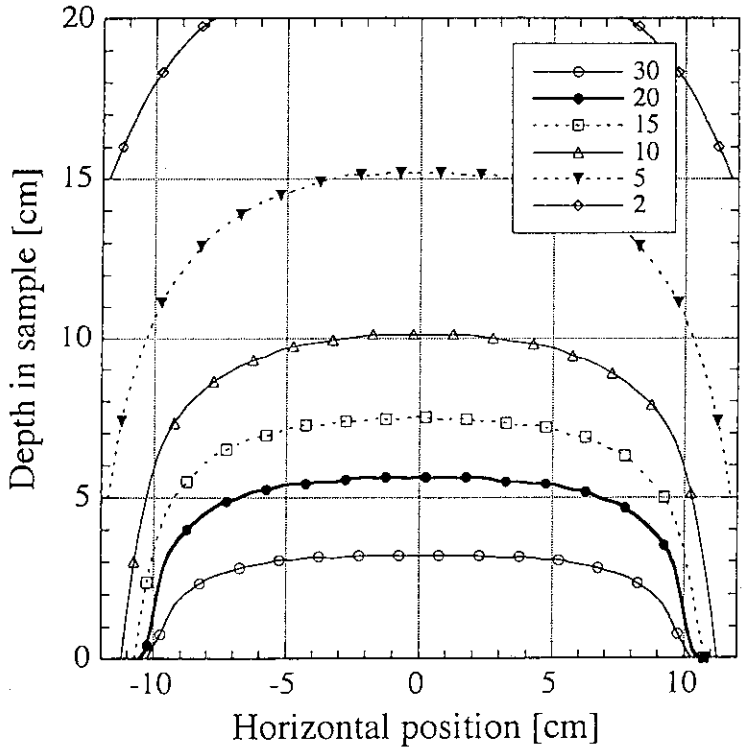

Fig. 3.4.5 Contour plot of dpa of Si on x-z plane for the SiC 50%/NaK 30% module for 35 MeV and the foot print of 5 cm x 20 cm

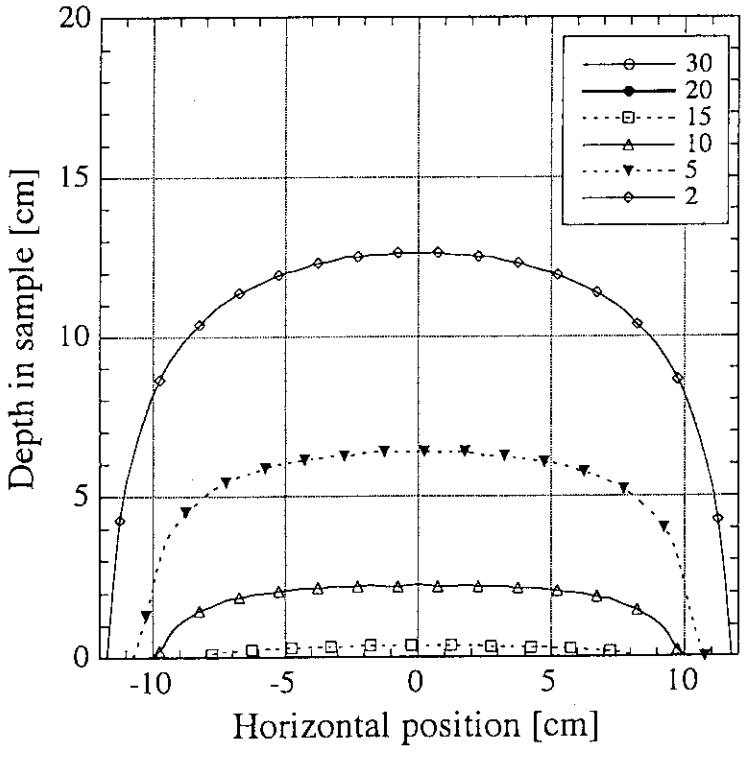

Fig. 3.4.6 Contour plot of dpa of Fe on x-z plane for the SiC 50%/NaK 30% module for 35 MeV and the foot print of 5 cm x 20 cm

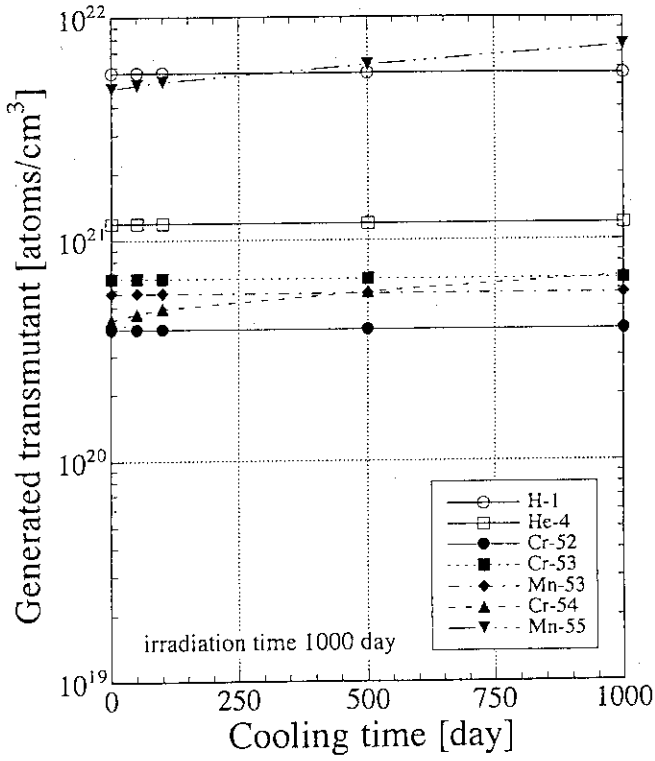

Fig. 3.6.1 Cooling time dependence of the number density of transmutant produced from Fe by 1000 day irradiation for the Fe50%/NaK30% module and the 5 cm x 20 cm foot print

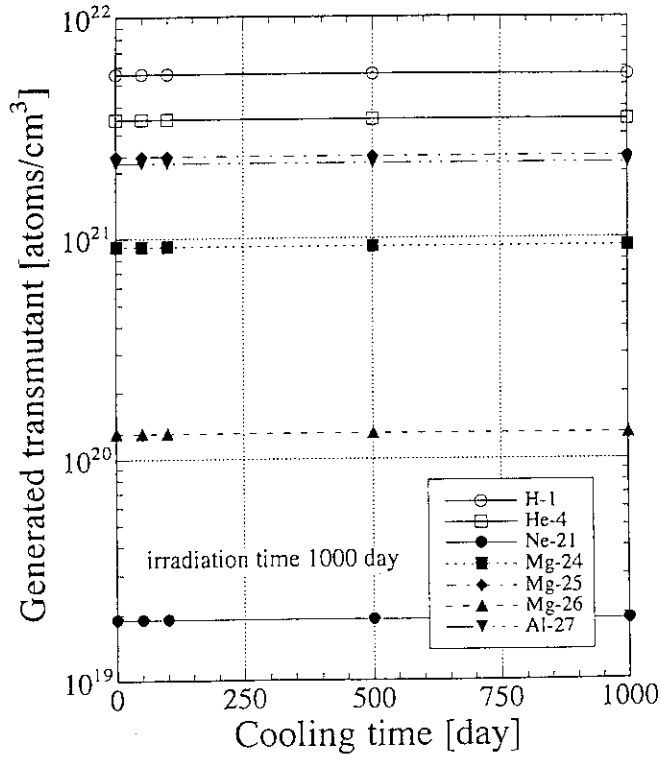

Fig. 3.6.2 Cooling time dependence of the number density of transmutant produced from SiC by 1000 day irradiation for the SiC50%/He module and the 5 cm x 20 cm foot print

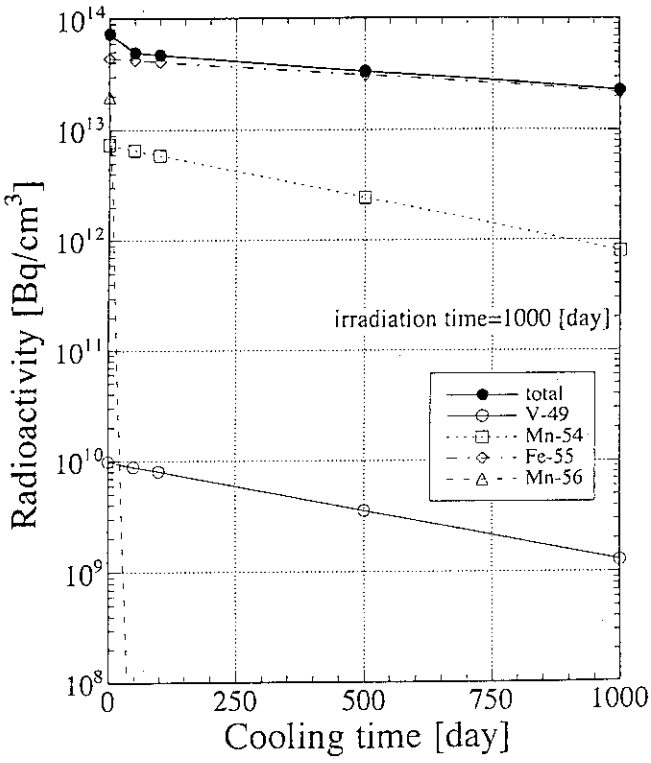

Fig. 3.6.3 Cooling time dependence of the number density of radio-activity produced from Fe by 1000 day irradiation for the Fe50%/NaK30% module and the 5 cm x 20 cm foot print

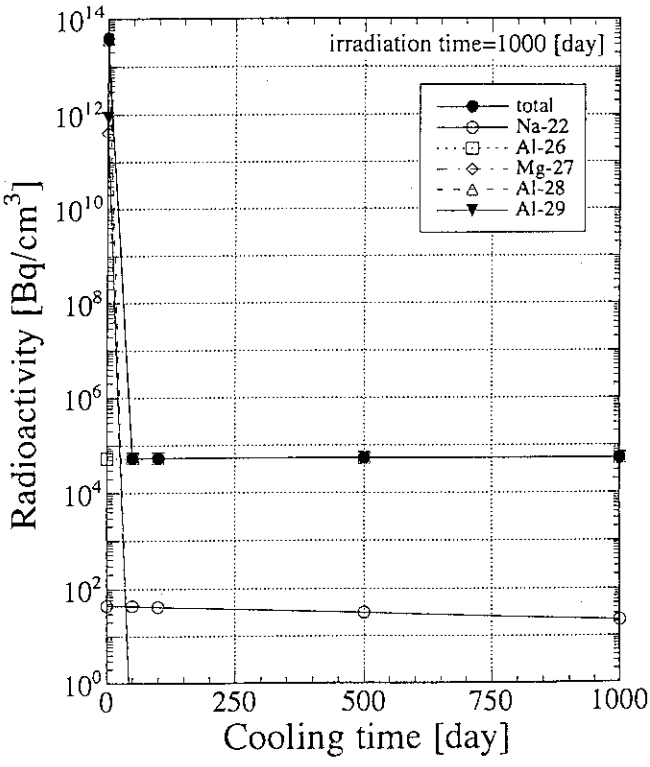

Fig. 3.6.4 Cooling time dependence of the number density of radio-activity produced from SiC by 1000 day irradiation for the SiC50%/He module and the 5 cm x 20 cm foot print

Table 3.1.1 The density and atomic number density of standard loading materials

material	density [g/cm^3]	nuclide	atomic number density [1x10^{24}/cm^3]
Iron	7.86	Fe	8.4760 x 10^{-2}
NaK	0.762	^{23}Na	4.4312 x 10^{-3}
		K	9.1312 x 10^{-3}
SiC	3.12	Si	4.6860 x 10^{-2}
		^{12}C	4.6860 x 10^{-2}

Table 3.3.1 The volume over the specific neutron flux for different material loadings and for different foot prints

	Cumulative volume [cm³]								
Area [cm²]	24x6				12x12	48x3	24x6	12x12	48x3
Lower flux [/cm²/sec]	Fe-50% NaK-30%	Fe-50%	SiC-50% NaK-30%	SiC-50%	Fe-50% NaK-30%	Fe-50% NaK-30%	Without material		
5.0x10¹⁴	112	80	64	64	160	0	64	128	0
3.0x10¹⁴	416	440	400	400	480	240	368	480	240
1.5x10¹⁴	896	944	880	896	1216	480	1088	1408	672
1.0x10¹⁴	1296	1328	1264	1312	1600	696	1656	2192	1032
5.0x10¹³	1968	2000	2048	2096	2336	1224	2736	2880	2040
0.0	2880	2880	2880	2880	2880	2880	2880	2880	2880

Table 3.3.2 The volume over the specific dpa rate for different material loadings and for different foot prints

	DPA cumulative volume of Fe [cm³]						
Area [cm²]	24 x 6		12 x 12	48 x 3	24 x 6	12 x 12	48 x 3
Lower DPA [/yr]	Fe 50% NaK 30%	Fe 50%	Fe 50% NaK 30%		Without material		
20	304	304	416	240	416	512	240
15	496	496	576	240	688	832	456
10	736	752	960	480	1120	1504	696
5	1360	1392	1648	912	2432	2792	1368
2	2240	2288	2528	1488	2880	2880	2568
0	2880	2880	2880	2880	2880	2880	2880

Table 3.3.2 The volume over the specific dpa rate for different material loadings and for different foot prints (continued)

	DPA cumulative volume of Si [cm³]			DPA cumulative volume of ^{12}C [cm³]		
Area [cm²]	24 x 6					
Lower DPA [/yr]	SiC 50% NaK 30%	SiC 50%	Without material	SiC 50% NaK 30%	SiC 50%	Without material
20	496	496	512	0	0	0
15	720	736	864	0	0	0
10	976	1008	1360	176	176	80
5	1728	1840	2576	608	608	576
2	2736	2752	2880	1440	1440	1864
0	2880	2880	2880	2880	2880	2880

Table 3.4.1 The volume over the specific dpa rate for different material loadings and for different foot prints by the detailed calculation

	DPA cumulative volume of Fe [cm³]							
deuteron energy	35 MeV						40 MeV	
sample material	Fe 50% and NaK 30%			Fe 50%			Fe 50% NaK 30%	Fe 50%
Lower DPA [/yr]	original	detailed	(ratio)	original	detailed	(ratio)	detailed	detailed
50	0	0		0	0		39.25	39.5
40	0	35.25		0	35.5		110.5	111.5
30	0	122.25		0	122.75		245.25	247.25
20	**301**	**312.5**	**0.963**	**304**	**319.0**	**0.953**	**521.0**	**528.5**
15	512	504.5	1.015	512	514.25	0.996	738.0	759.75
10	784	800.75	0.979	816	818.25	0.997	1083.0	1104.25
5	1440	1400.0	1.029	1472	1435.5	1.025	1728.0	1806.5
2	2344	2328.0	1.007	2392	2392.0	1.0	2692.0	2728.0
0	2880	2880.0		2880	2880.0		2880.0	2880.0

(Note)

ratio = (original DPA) / (detailed DPA)

The sample volume is 24 [cm] x 6 [cm] x 20 [cm] = 2880.0 [cm³].

The original calculation used 360 cell tallies with 2 x 2 x 2 = 8 [cm³].

The detailed calculation used 4 zones of cell tallies in a quarter of the region; first zone was 1152 cells with 0.5 x 0.5 x 0.25 = 0.0625 [cm³], second zone was 1728 cells with 0.5 x 0.5 x 0.5 = 0.125 [cm³], third zone was 216 cells with 1 x 1 x 1 = 1 [cm³], and forth zone was 108 cells with 1 x 1 x 2 = 2 [cm³].

Table 3.4.1 The volume over the specific dpa rate for different material loadings and for different foot prints by the detailed calculation (continue)

	DPA cumulative volume of SiC [cm³]	
deuteron energy	35 MeV	
sample material	SiC 50% and NaK 30% (detailed calculation)	
Lower DPA [/yr]	Si	C
50	21.25	0.0
40	85.75	0.0
30	203.25	0.0
20	**464.5**	**0.0**
15	696.0	10.0
10	1058.0	124.75
5	1786.5	553.25
2	2760.0	1404.0
0	2880.0	2880.0

Table 3.5.1 He/dpa ratio of Fe in different test module and foot prints

Area [cm^2]	24 x 6		12 x 12	48 x 3
Sample	Fe 50% NaK 30%	Fe 50%	Fe 50% NaK 30%	
Averaged DPA of Fe [/yr]	8.04	8.20	9.54	5.38
Averaged ^{4}He of Fe [ppm/yr]	111.8	114.6	130.2	78.2
^{4}He / DPA	13.9	14.0	13.6	14.5

Table 3.5.2 Nuclear heating at front region (0-2 cm layer) of the module

		Nuclear heating by Fe [W/cm³]				Nuclear heating by SiC [W/cm³]	
Area [cm²]		24 x 6		12 x 12	48 x 3	24 x 6	
Sample		Fe 50% NaK 30%	Fe 50%	Fe 50% NaK 30%		SiC 50% NaK 30%	SiC 50%
Gamma-ray	Average	9.593	9.473	11.76	5.726	1.303	1.208
	Maximum	14.12	13.93	17.71	6.952	1.874	1.740
Neutron	Maximum	9.483	9.498	10.29	6.464	17.61	17.63

4. Comparison of Transmutation to DEMO Reactor

4.1 Irradiation Condition in the DEMO reactors

For the typical reactor irradiation conditions, the SSTR[21] and DREAM[22] design were adopted from the Japanese DEMO designs. The SSTR reactor uses F82-H steel for structural material and water for coolant, and the DREAM uses SiC and He, respectively. The conceptual view of the SSTR reactor is shown in Fig. 4.1.1 and the major parameters is listed in Table 4.1.1. The reference wall load was 5 MW/m^2 (1.8 x 10^{14} n/cm^2/s). The calculations for both reactors were done by the one dimensional Sn code, ANISN, in which the model used is shown in Figs. 4.1.2 and 4.1.3. Figures 4.1.4 and 4.1.5 compare the neutron spectra of both the averaged flux of IFMIF, and the first wall fluxes of SSTR and of DREAM, respectively. The low energy neutron flux of DREAM is lower than the SSTR, and the IFMIF flux has no thermal neutrons. As seen in the next section, even including the wall of the target cell, the lower energy flux of the IFMIF is lower than both the reactors by three decades of order. The fractions of high energy flux above 1 MeV to the total flux are 42, 50 and 90 %, for SSTR, DREAM and IFMIF, respectively. Thus the IFMIF spectrum is very hard compared to that in the fusion reactor environment. This might be affected to the transmutation due to capture reaction. However, the spectrum can be simulated to the reactor one, by adopting an appropriate reflector.

4.2 Comparison to the IFMIF Condition

The tranmutants of iron loaded in the IFMIF module are compared to the transmutants when the iron sample is placed at the first wall of the SSTR reactor and the SiC in the IFMIF to the DREAM. The irradiation period 1000 days corresponds to about 20 dpa in the first wall of the reactors with 5 MW/m^2 neutron wall load. Fig 4.2.1 presents the production rates of major transmuted nuclides from Fe by the IFMIF neutrons at the 5x 10^{14} n/cm^{2}s for 35 MeV incident deuteron and from F82H steel by the SSTR neutrons of 5 MW/m2 wall load (1.8 x10^{14} n/cm^{2}s) after 1000 days irradiation. The averaged spectrum in the whole sample volume was used to calculate the transmutation, so that the 25 x 400 mm^2 target case is lower than the others. The transmutations of IFMIF are higher than the SSTR even considering the flux intensity. Figure 4.2.2 shows ratio of transmutation to the ^{55}Mn production. The productions of ^{54}Cr and ^{53}Cr are slightly different, where the ^{51}V is a product from ^{52}Cr of F82H. The generation rate of transmutant should be compared with the dpa rate to see how different the transmutant is produced in the same dpa irradiation and how fast the IFMIF can simulate the transmutant impurity. Figures 4.2.3-5 show the transmutant from Fe as a function of dpa in SSTR, for 0, 500, 1000 days cooling time, respectively. These can be compared to the results of the IFMIF samples in the Fe/He module with 50 x200 mm^2 beam shape as shown in Figs. 4.2.6-8 and also to those of Fe/NaK module as

shown in Figs. 4.2.9-11. The largest production is hydrogen and ^{55}Mn, and ^{55}Mn increases with cooling time. The transmutant generation for hydrogen and ^{55}Mn in the SSTR is higher than the IFMIF at the same dpa. Hydrogen produced by ^{56}Fe(n,p) and ^{55}Mn by ^{56}Fe(n,np) and ^{54}Fe(n,γ), where (n, p) has a threshold about a few MeV, and (n,np) has over 15 MeV but (n,γ) has large cross section. Thus the large production of those in the SSTR is due to higher flux at 15 MeV and at low energy in the SSTR. However, there is no significant difference for the other transmutants from the Fe/He and Fe/Nak modules in the IFMIF.

Figure 4.2.12 also shows the production rates for the SiC sample and the DREAM reactor. It is seen from this figure that the production of ^{27}Al and ^{24}Mg in the IFMIF is larger than the DREAM. The ^{21}Ne production comes from high energy reaction. The ratios to ^{25}Mg show that the production are two time higher for ^{27}Al and four times higher for ^{24}Mg. Figures 4.2.13 and 4.2.14 show the transmutants from Si at the first wall in the DREAM and the IFMIF SiC module. To compare, hydrogen and helium in the DREAM are almost the same behavior with dpa as the IFMIF, but ^{25}Mg and ^{27}Al in the DREAM are different from the IFMIF. This can be explained by as follows: ^{25}Mg is produced by ^{28}Si(n,α) and ^{27}Al by (n,np); (n,np) has high threshold over 15 MeV and (n,α) has a response in 5-10 MeV range. Because the IFMIF has harder spectrum than the DREAM, and the DREAM has higher flux at the 10 MeV region, ^{27}Al is higher in the IFMIF and the ^{25}Mg higher in the DREAM.

Table 4.1.1 Major parameters of SSTR

Major Radius	Rp	7.0m	Bootstrap Current	Ibootstrap	9 MA
Minor Radius	ap	1.75m	Beam Driven Current	Ibeam	3 MA
Elongation	κ	1.8	NBI Power	P_{NBI}	60 MW
Triangularity	δ	0.3	Beam Energy	Ebeam	2MeV
Aspect Ratio	A	4.0	Fusion Power	Pfusion	3000MW
Plasma Volume	V	760m³	Power Gain	Q	50
Plasma Current	Ip	12MA	Total Thermal Output	P_{th}	3710MW
Toroidal Field	Bt	9T	Max. Neutron Wall Load	P_n	5MW/m²
Safety Factor	q(95%)	5.0	Gross Electric Power	P_{eG}	1280MWe
Safety Factor	q(0)		Net Electric Power	P_{enet}	1080MWe
Toroidal Beta	βt	2.52%			
Poloidal Beta	βp	2.0			
Troyon Factor	g	3.3			
Average Density	<ne>	1.45×10^{20}m⁻³			
Average Temperature	$\frac{<nT>}{<n>}$	17keV			
Effective Charge	Zeff	1.8			
He Concentration	f(He)	0.05			

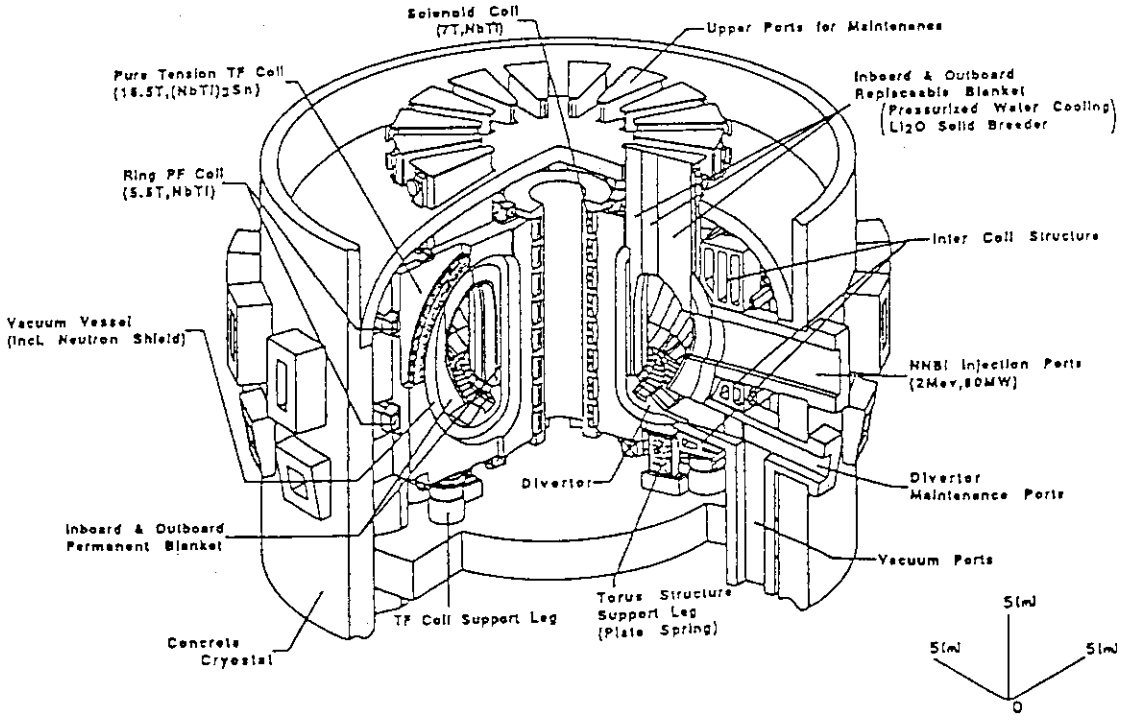

Fig. 4.1.1 Bird's eye view of SSTR

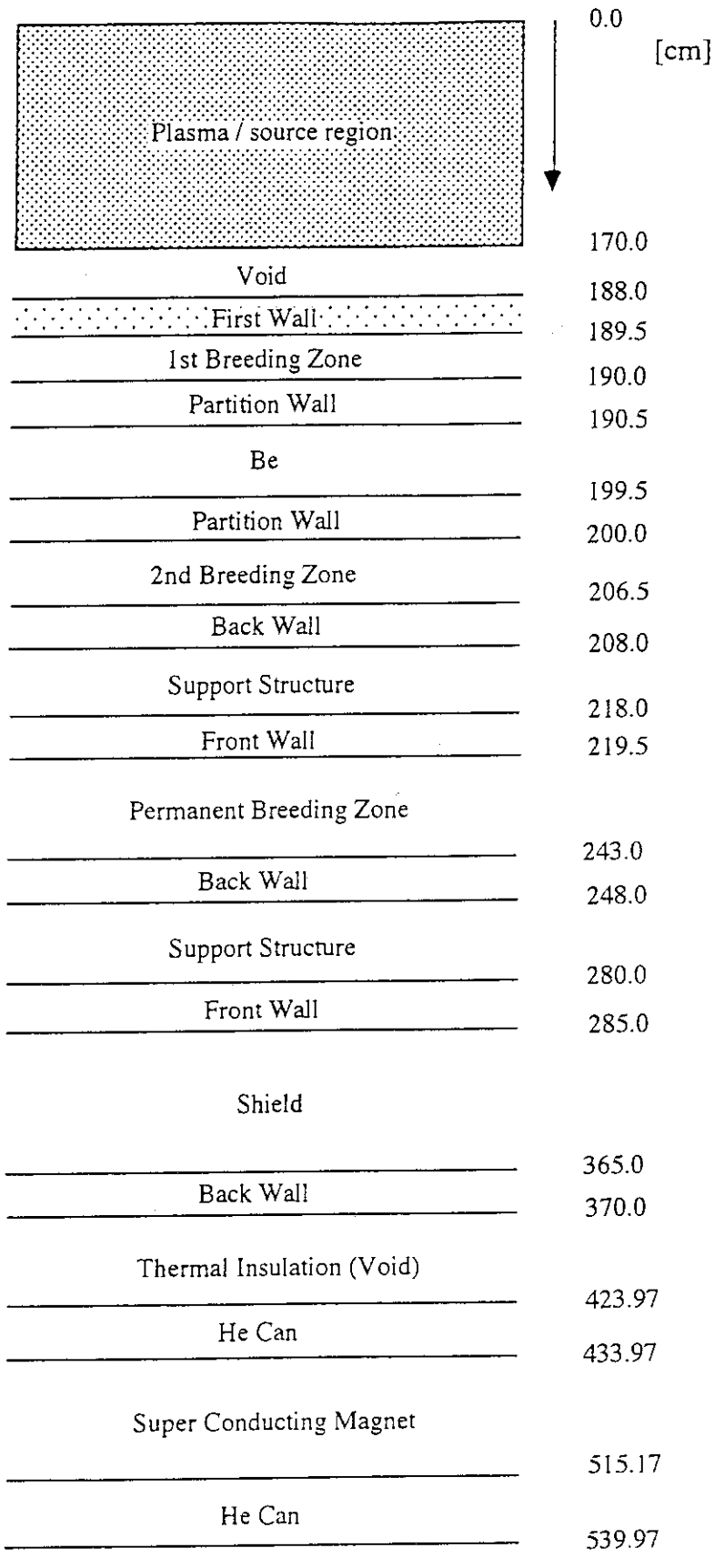

Fig. 4.1.2 One dimensional cylinder model of the SSTR for ANISN calculation

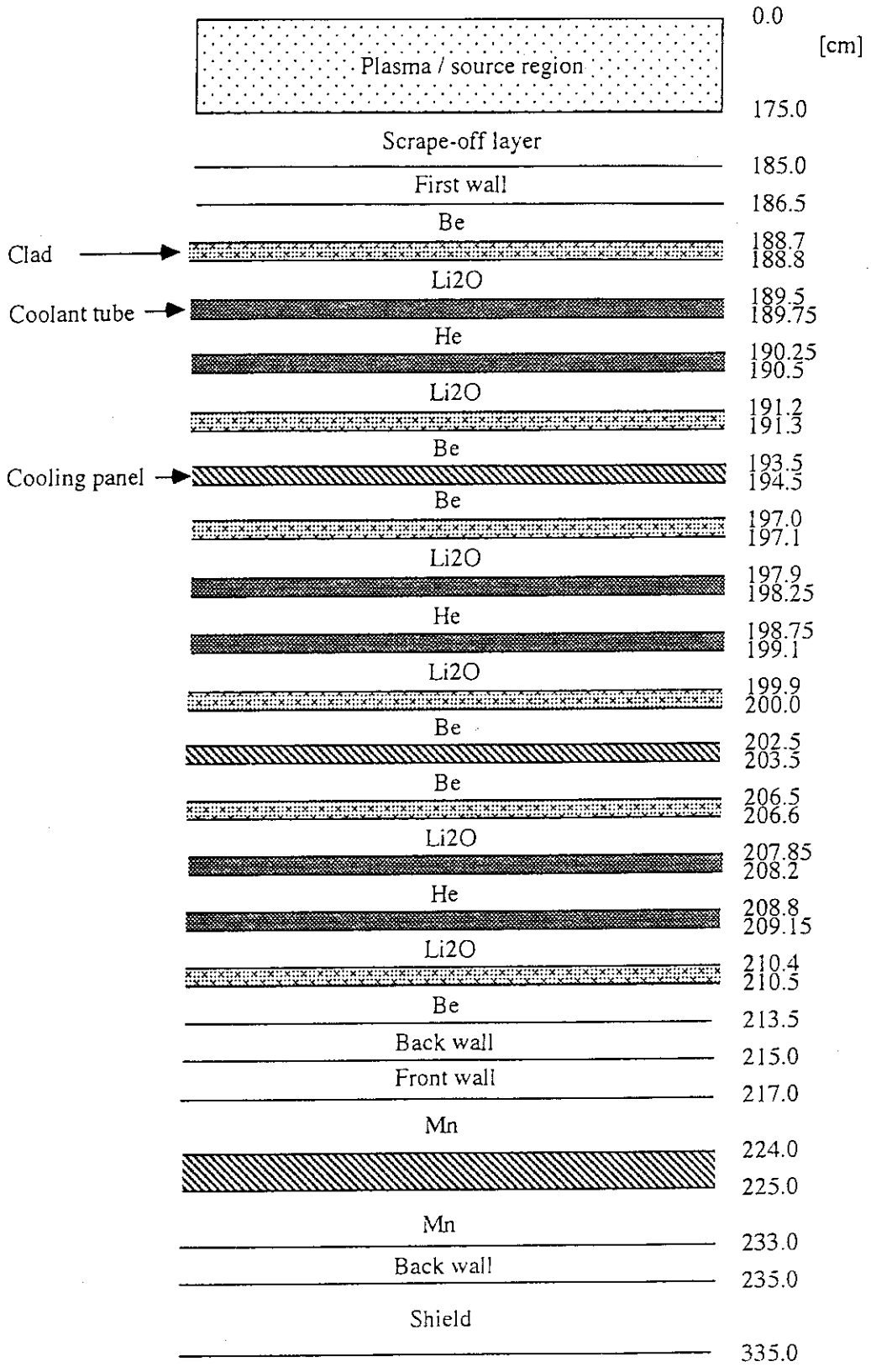

Fig. 4.1.3 One dimensional cylinder model of the DREAM for ANISN calculation

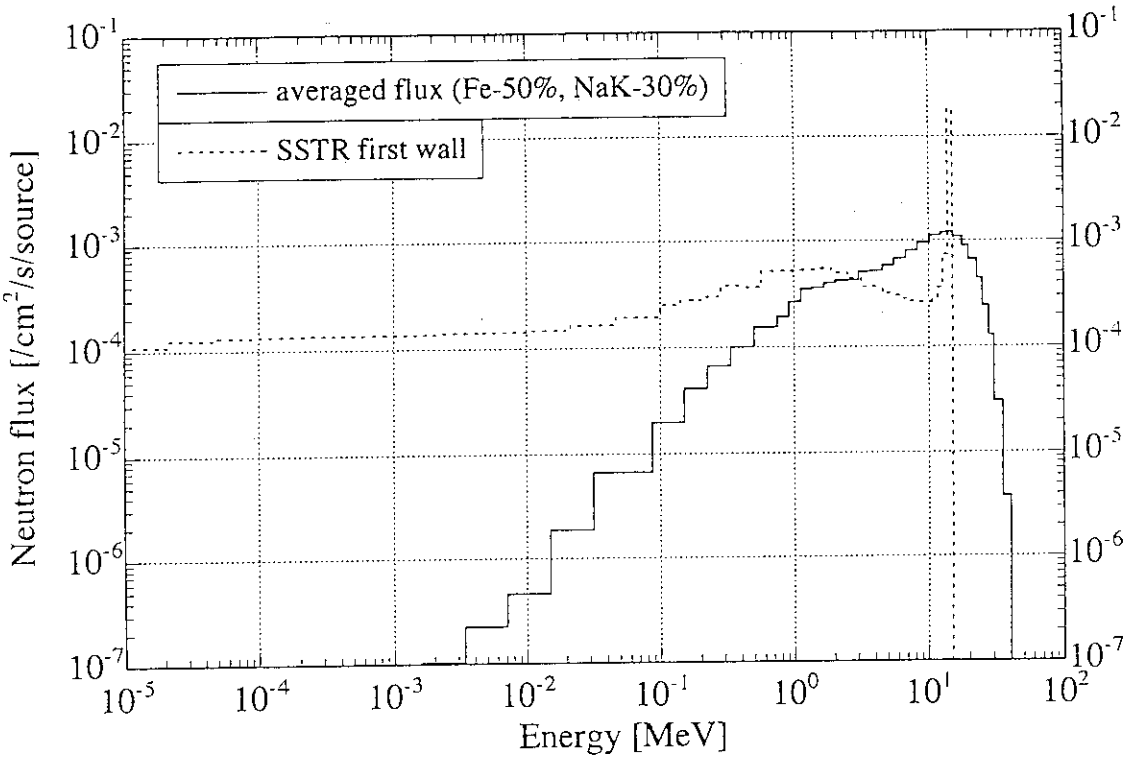

Fig. 4.1.4 Comparison of neutron spectrum of the IFMIF test module with Fe50%/ NaK30% to the spectrum at the first wall of the SSTR

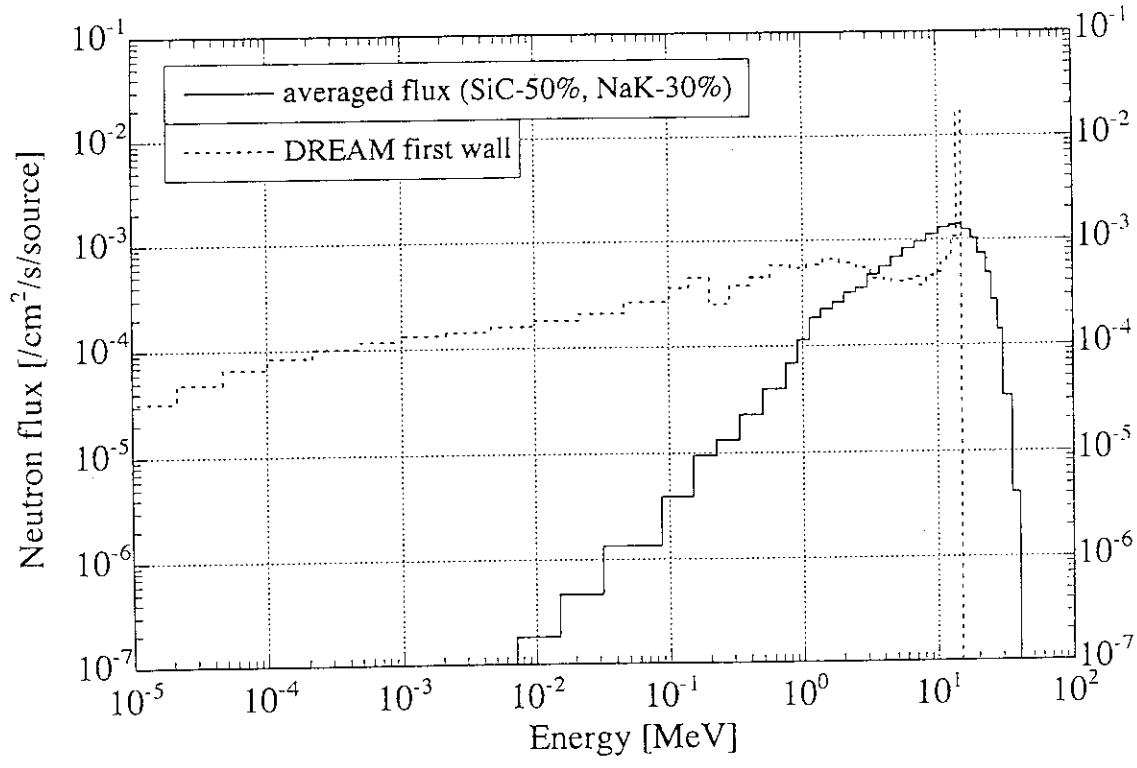

Fig. 4.1.5 Comparison of neutron spectrum of the IFMIF test module with SiC50%/ NaK30% to the spectrum at the first wall of the DREAM

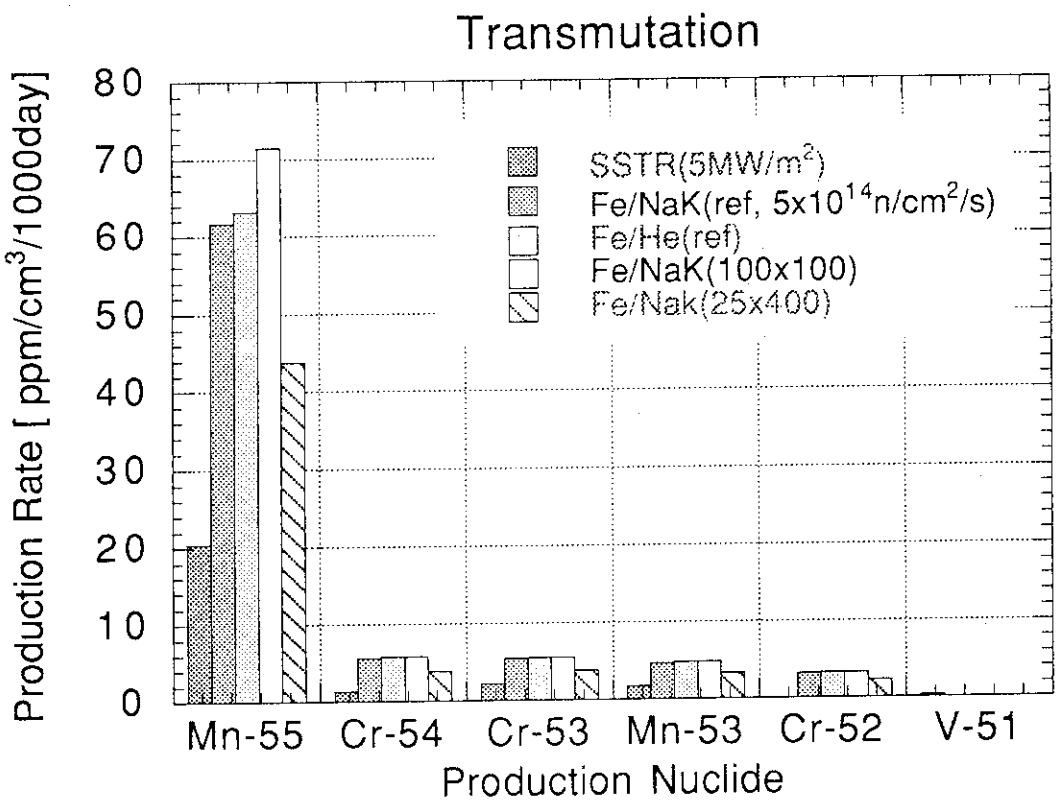

Fig. 4.2.1 Comparison of production rate of transmutants from Fe among the various cases

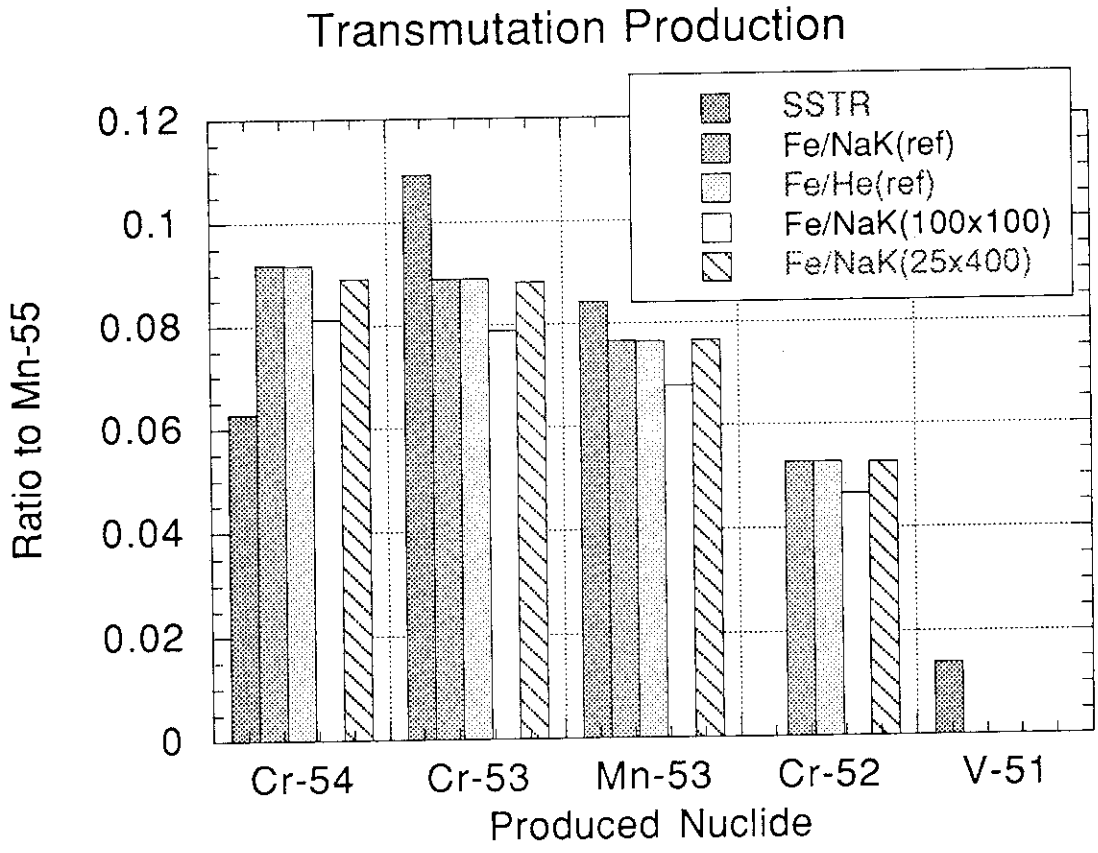

Fig. 4.2.2 Ratio of transmutants to the ^{55}Mn production

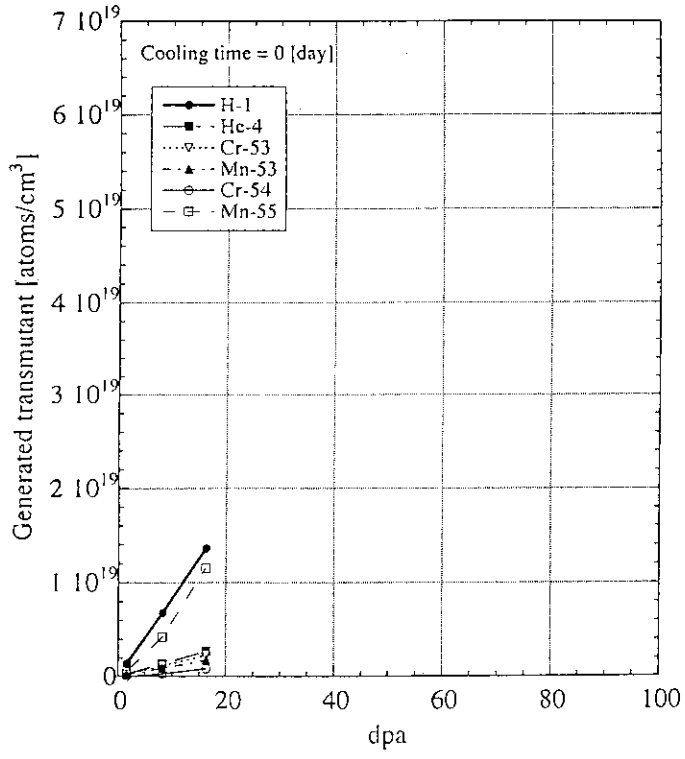

Fig. 4.2.3 Generation rate of transmutant with dpa of Fe at the SSTR first wall (cooling time = 0 day)

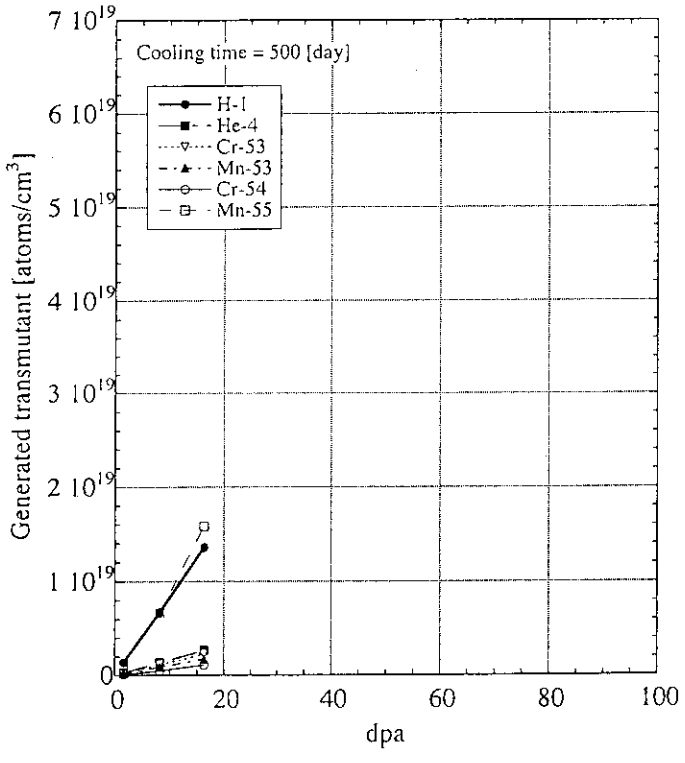

Fig. 4.2.4 Generation rate of transmutant with dpa of Fe at the IFMIF Fe50%/He module with the foot print of 5 cm x 20 cm (cooling time = 0 day)

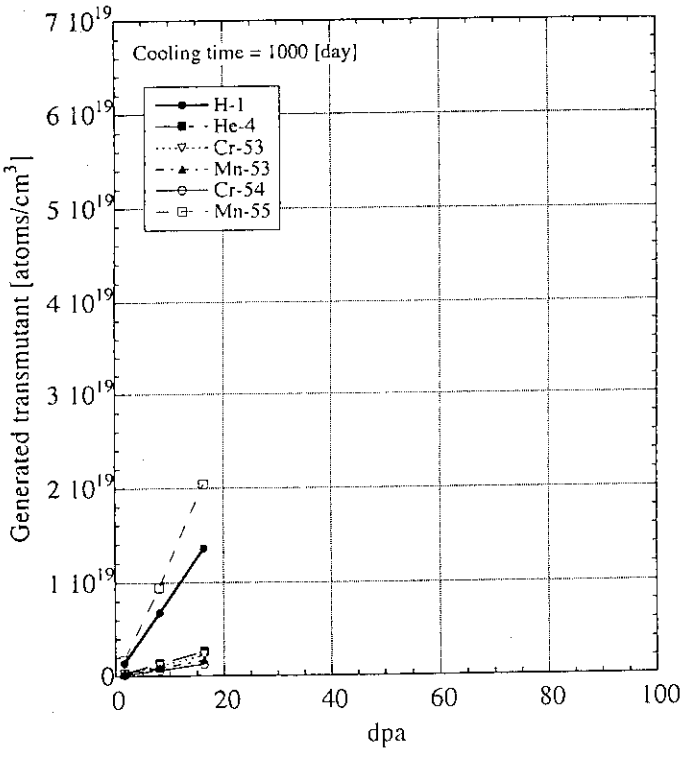

Fig. 4.2.5 Generation rate of transmutant with dpa of Fe at the SSTR first wall (cooling time = 500 day)

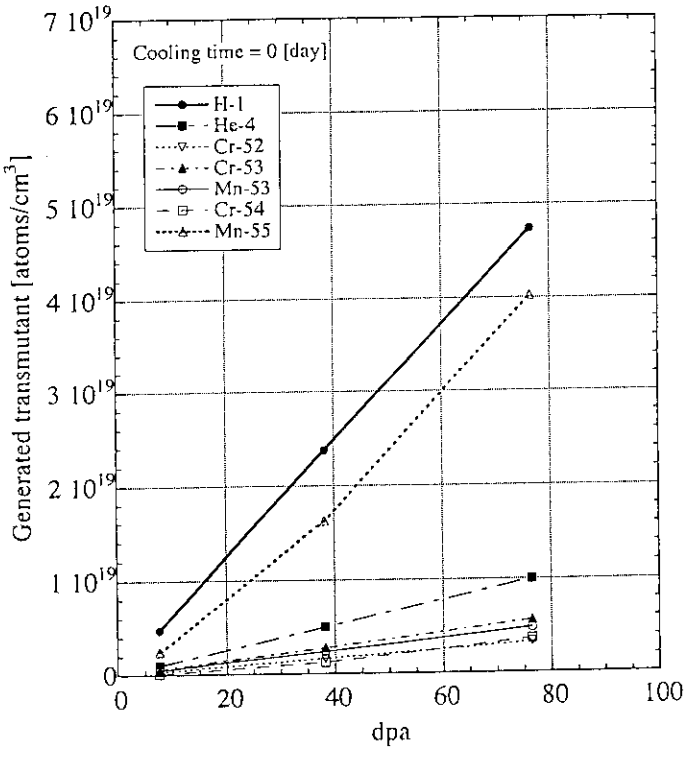

Fig. 4.2.6 Generation rate of transmutant with dpa of Fe at the SSTR first wall (cooling time = 1000 day)

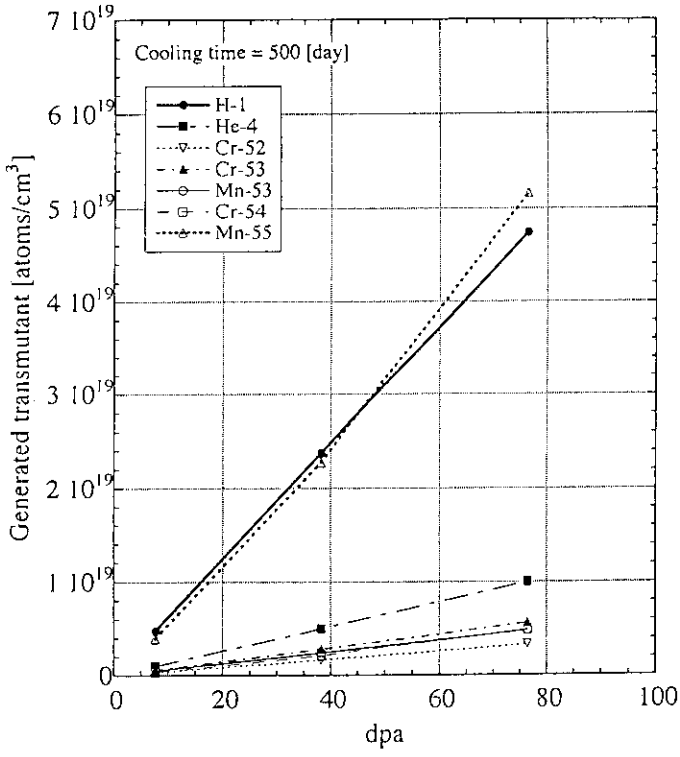

Fig. 4.2.7 Generation rate of transmutant with dpa of Fe at the IFMIF Fe50%/He module with the foot print of 5 cm x 20 cm (cooling time = 500 day)

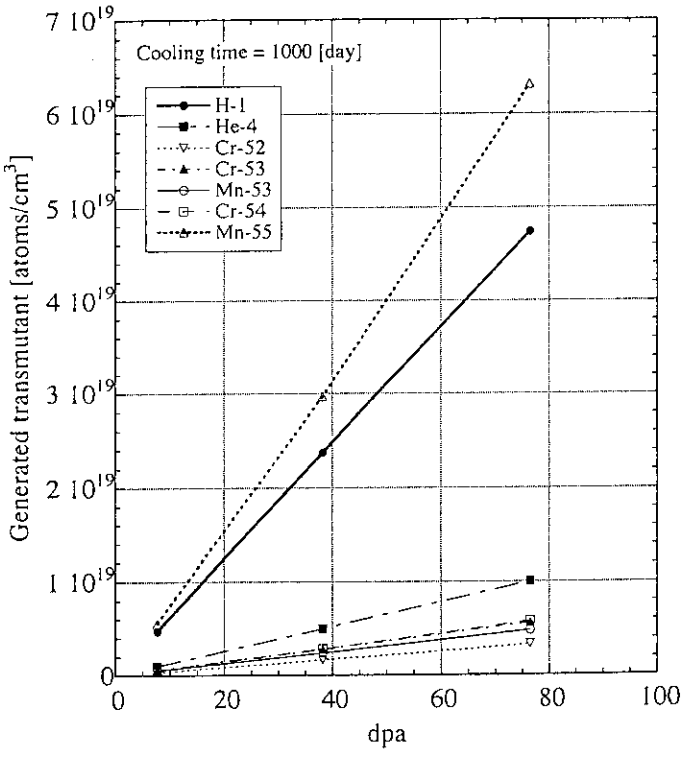

Fig. 4.2.8 Generation rate of transmutant with dpa of Fe at the IFMIF Fe50%/He module with the foot print of 5 cm x 20 cm (cooling time = 1000 day)

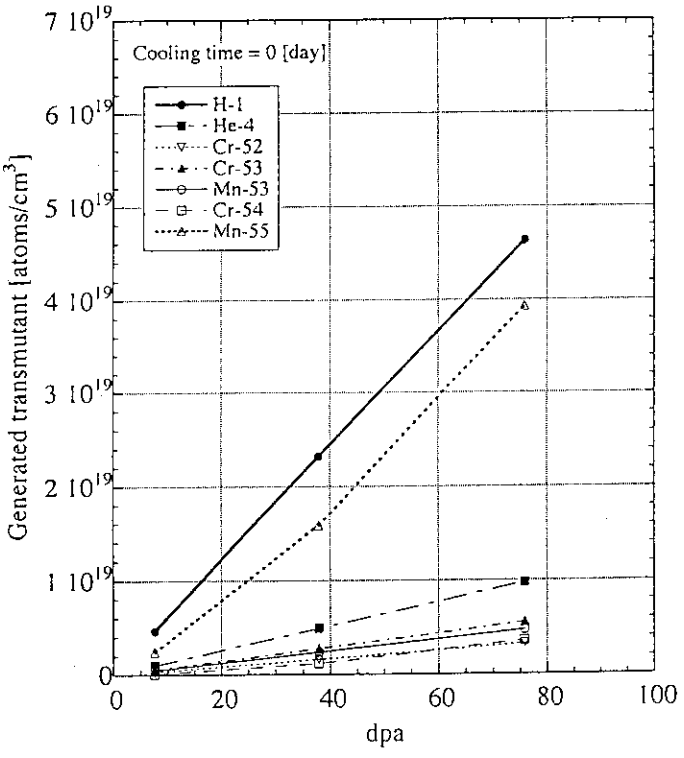

Fig. 4.2.9 Generation rate of transmutant with dpa of Fe at the IFMIF Fe50%/NaK30% module with the foot print of 5 cm x 20 cm (cooling time = 0 day)

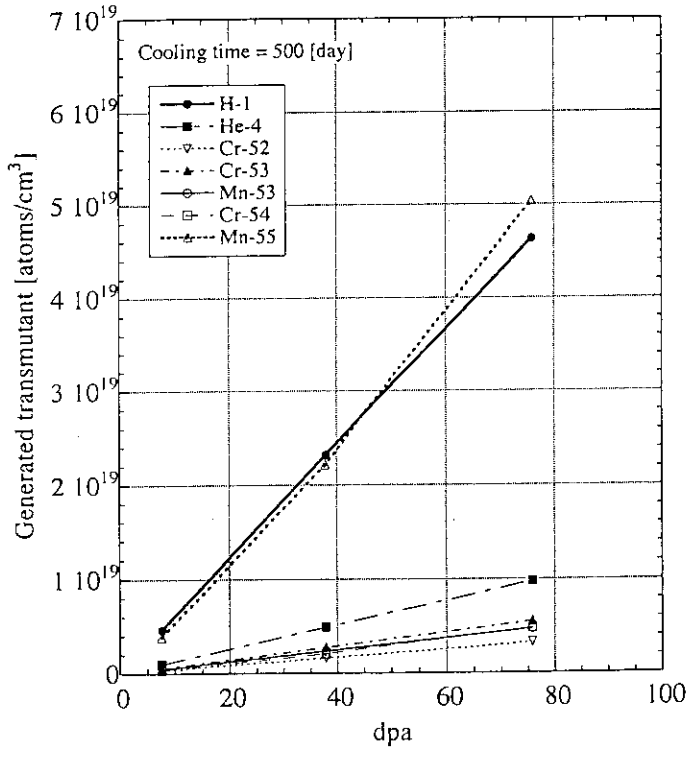

Fig. 4.2.10 Generation rate of transmutant with dpa of Fe at the IFMIF Fe50%/NaK30% module with the foot print of 5 cm x 20 cm (cooling time = 500 day)

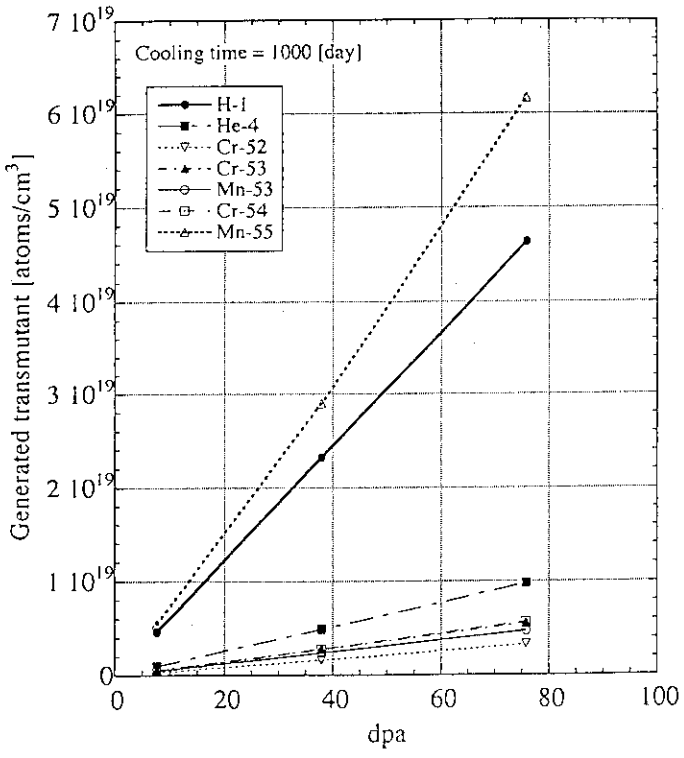

Fig. 4.2.11 Generation rate of transmutant with dpa of Fe at the IFMIF Fe50%/NaK30% module with the foot print of 5 cm x 20 cm (cooling time = 1000 day)

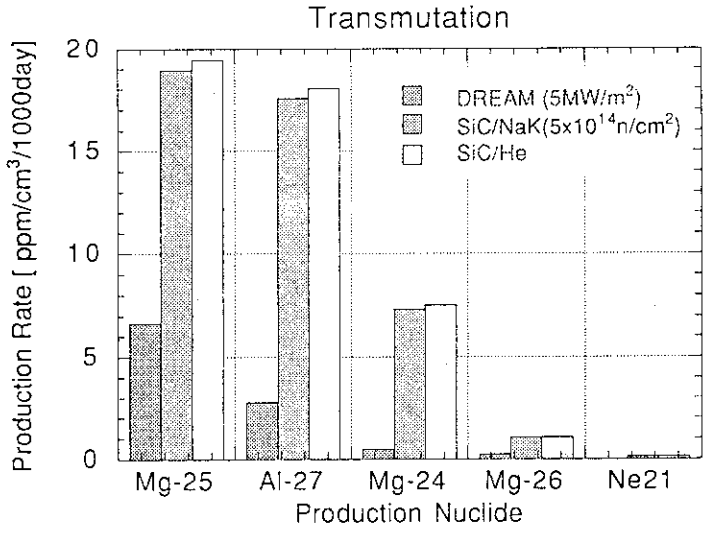

Fig. 4.2.12 Comparison of production rate of transmutants from SiC among the various cases

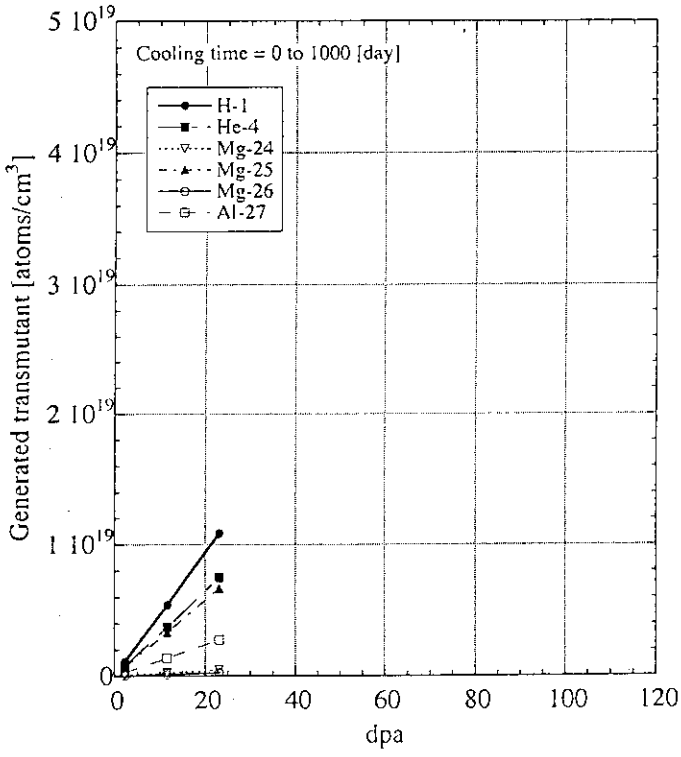

Fig. 4.2.13 Generation rate of transmutant with dpa of SiC at the first wall of the DREAM (no change during cooling time = 0-1000 day)

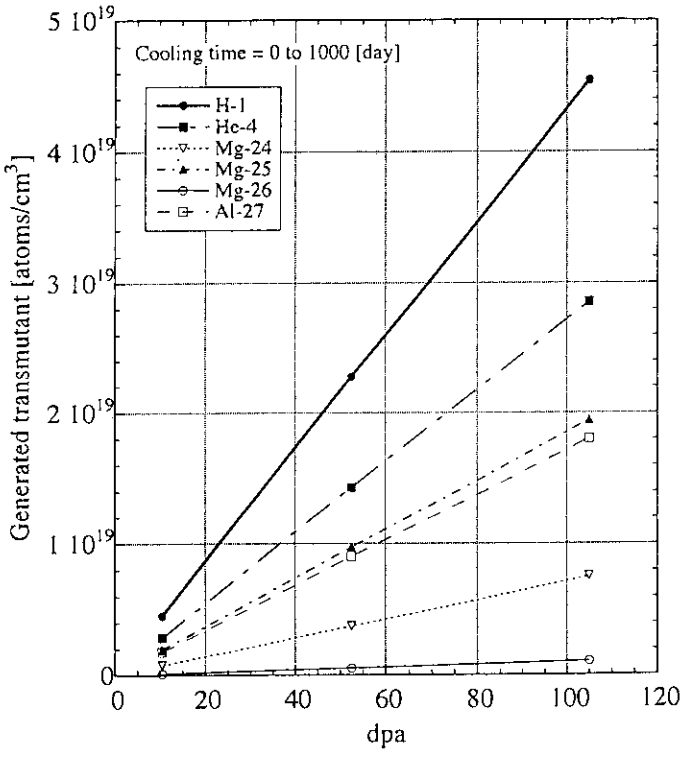

Fig. 4.2.14 Generation rate of transmutant with dpa of SiC at the IFMIF SiC50%/He module with the foot print of 5 cm x 20 cm (cooling time = 0-1000 day)

5. Neutron Field inside the Test Cell

5.1 Dpa Distribution

Neutron flux and dpa distributions inside the test cell are also important to evaluate the usefulness of utilization of the space outside the test module. This requirement is raised from the mainly functional materials tests which usually can be performed in rather low flux by measuring electrical or optical method. For this purpose, 0.1 or 0.01 dpa/y is a guide dpa rate to judge such a usefulness. To obtain these distributions, the room size is assumed to be 6 m x 6m x 6m cubic surrounded by ordinary concrete as shown in Fig. 5.1.1. The target surface is located at the center of the room. For Monte Carlo calculation, the wall thickness of 20 cm was taken in account. Table 5.1.1 summarizes the atomic number density used in the concrete model. The 200 mm long module of Fe/NaK and the incident of 35 MeV deuteron beam is considered.

Figures 5.1.2 and 5.1.3 show the dpa distributions on the vertical (y-z) and the horizontal (x-z) planes at the 0.1 and 0.01 dpa/yr of Fe. In y-z plane, the contour map shows the wing so that just behind the module, the flux is depressed, while on the x-z plane there is no wing structure. This is caused by the two beam incident on the plane. These figures assure that the IFMIF can provide 0.01 dpa/yr region at the upper and lower direction. Figures 5.1.4-5 and Figs. 5.1.6-7 show the contour map of dpa for Si and C when the SiC module is placed.

The effect of the concrete wall of the room on the above dpa level is examined in Figs 5.1.8 and 5.1.9. The figures indicate the wall increase the dpa levels especially for 0.01 dpa/y region.

The neutron spectra are plotted in Fig. 5.1.10 at the boundary position of 0.1 dpa and with directions of forward, upper directions of 90 and 45 degrees, and 45 degree on horizontal plane . The spectrum of peak region is broaden and shifted to lower with increase of the direction angle. Therefore, when the 14 MeV spectrum is important, the test space should be taken at the forward direction. From the contour map, the 0.01 dpa/y region at the forward direction is very small and should be carefully considered. Figures 5.1.11 shows the effect of the room wall on the neutron spectrum at the forward direction on the 0.1 dpa/y boundary. Since the case with concrete wall gives far position from the target for the same dpa level, the spectrum peak is lower than without the wall and the lower energy flux is increased very much.

5.2 Nuclear Heating Distribution

To estimate the nuclear heating of the components located in the test cell, the nuclear heating rate distribution are calculated inside the test cell. The total, neutron and gamma-ray heating rate distributions on the horizontal and vertical planes are shown in Figs. 5.2.1-2, 5.2.3-4 and 5.2.5-6, respectively. To estimate the heating of the concrete wall, considering

KERMA factor difference between Fe and concrete, a factor of 1.5 should be multiplied to the heating rate of Fe. Therefore, nuclear heating of the concrete wall is expected to be 3-8 mW/cm^3. This gives the condition for the cooling system of the wall. From the comparison of the neutron and gamma-ray heating, the neutron heating has the strong directivity of the forward, while the gamma-ray heating is very isotropic and uniform.

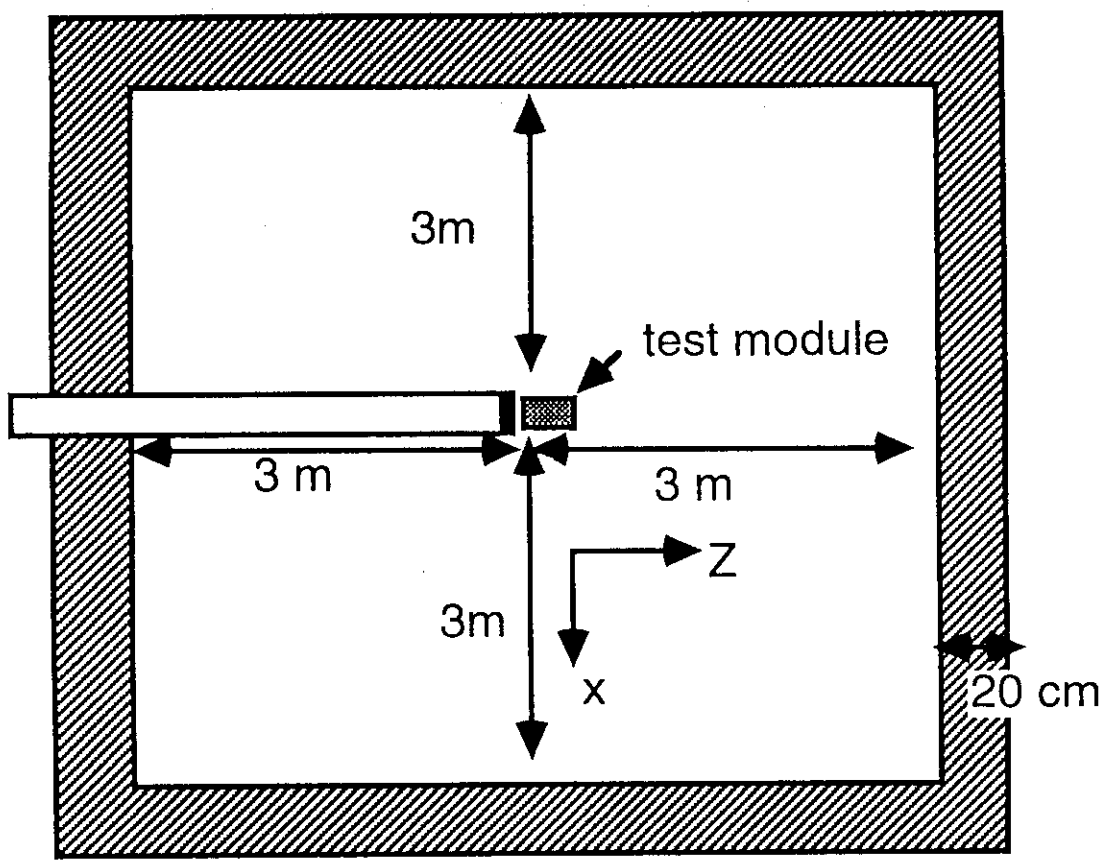

Fig. 5.1.1 Calculation model of the test cell (horizontal plan)

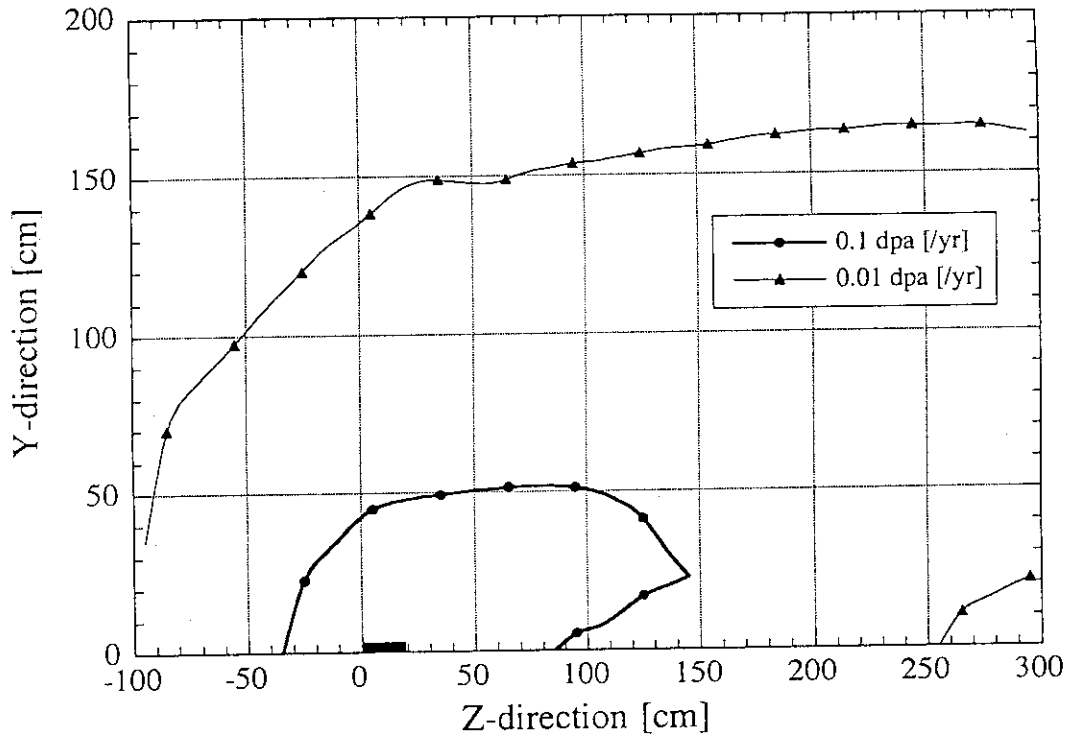

Fig. 5.1.2 Contour plot of dpa rate of Fe on the y-z plane in the test cell in the case that the Fe50%/NaK30% module is placed for 35 MeV deuteron

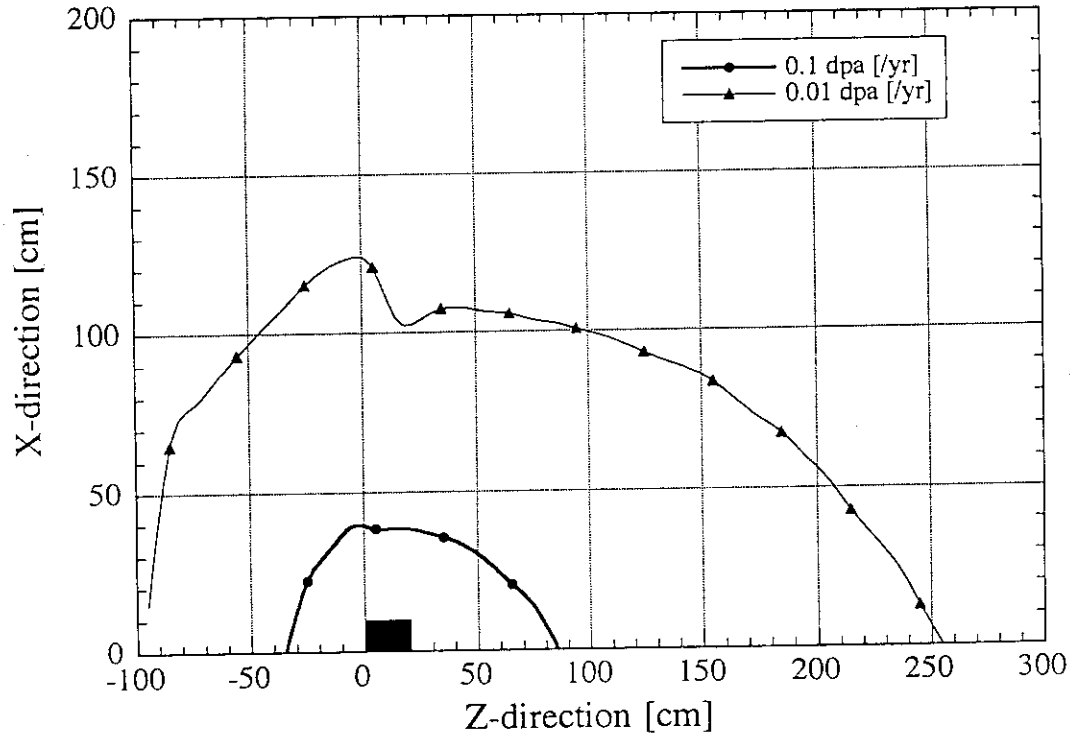

Fig. 5.1.3 Contour plot of dpa rate of Fe on the x-z plane in the test cell in the case that the Fe50%/NaK30% module is placed for 35 MeV deuteron

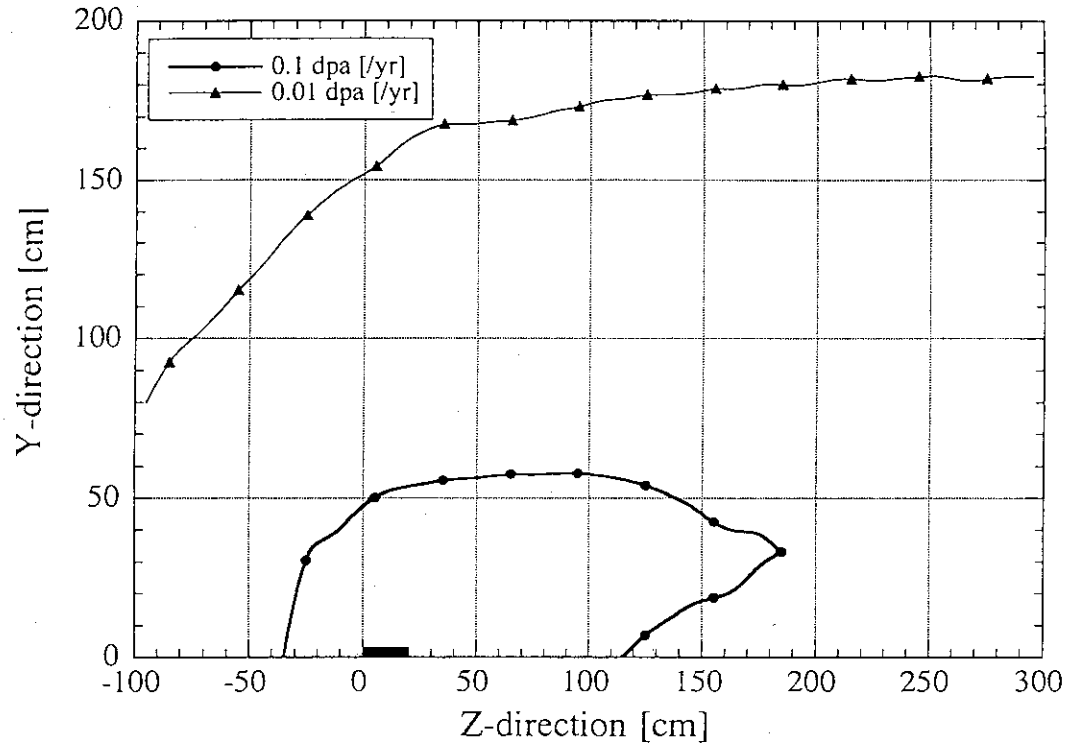

Fig. 5.1.4 Contour plot of dpa rate of Si on the y-z plane in the test cell in the case hat the SiC50%/NaK30% module is placed for 35 MeV deuteron

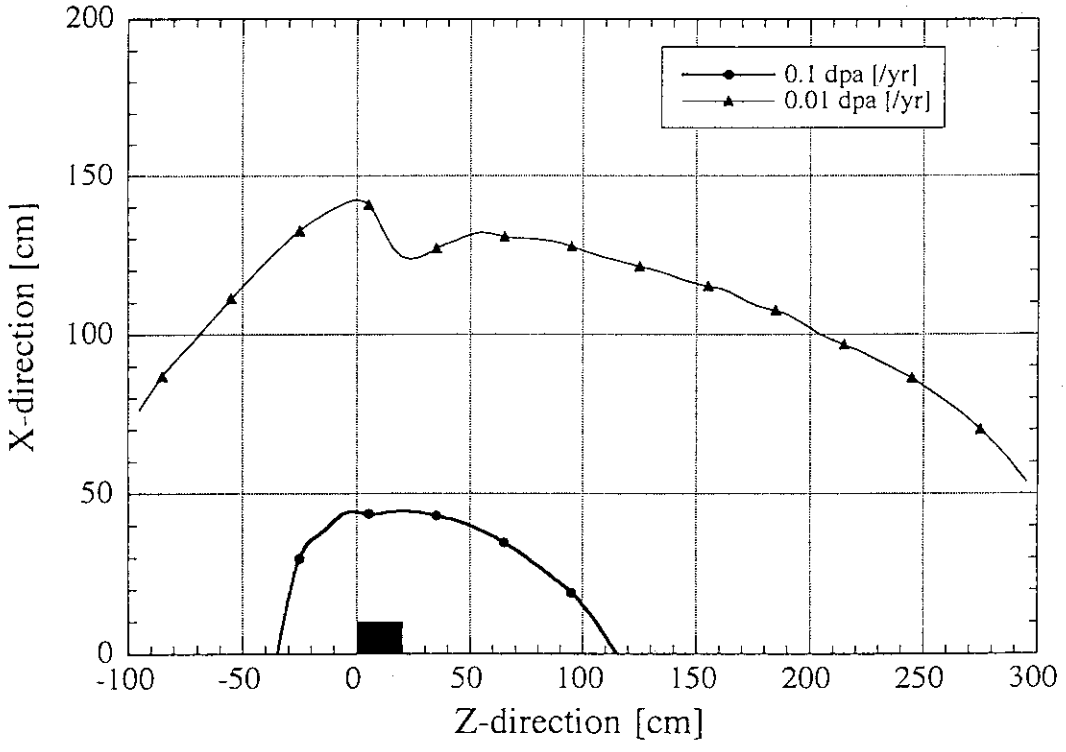

Fig. 5.1.5 Contour plot of dpa rate of Si on the x-z plane in the test cell in the case that the SiC50%/NaK30% module is placed for 35 MeV deuteron

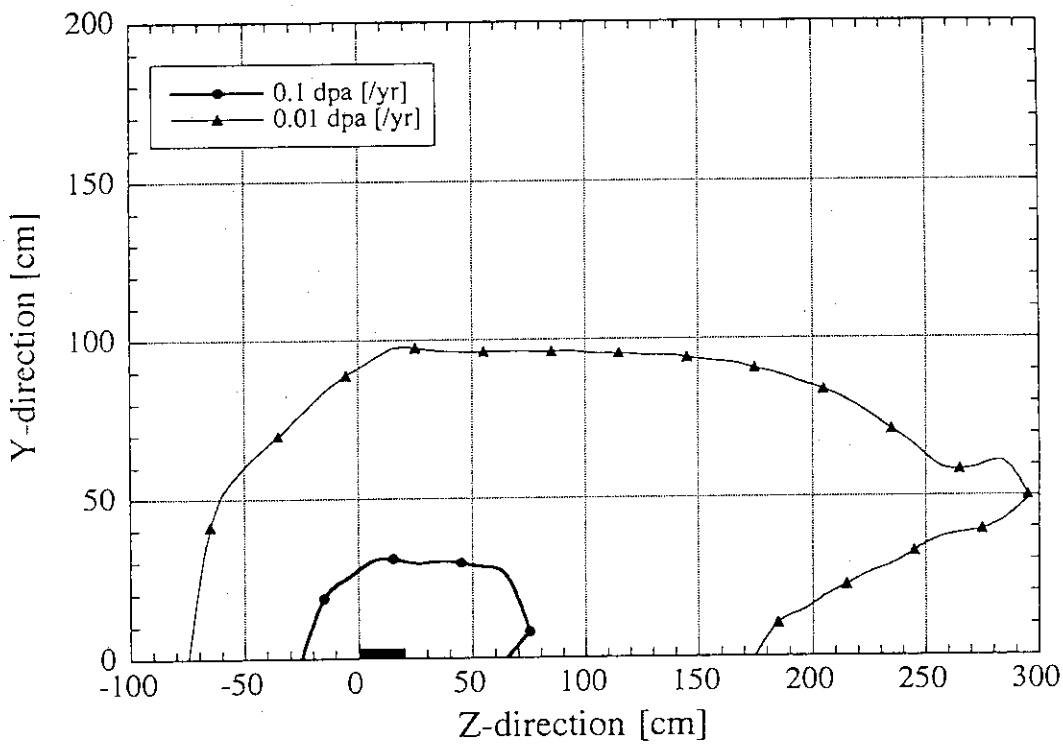

Fig. 5.1.6 Contour plot of dpa rate of C on the y-z plane in the test cell in the case that the SiC50%/NaK30% module is placed for 35 MeV deuteron

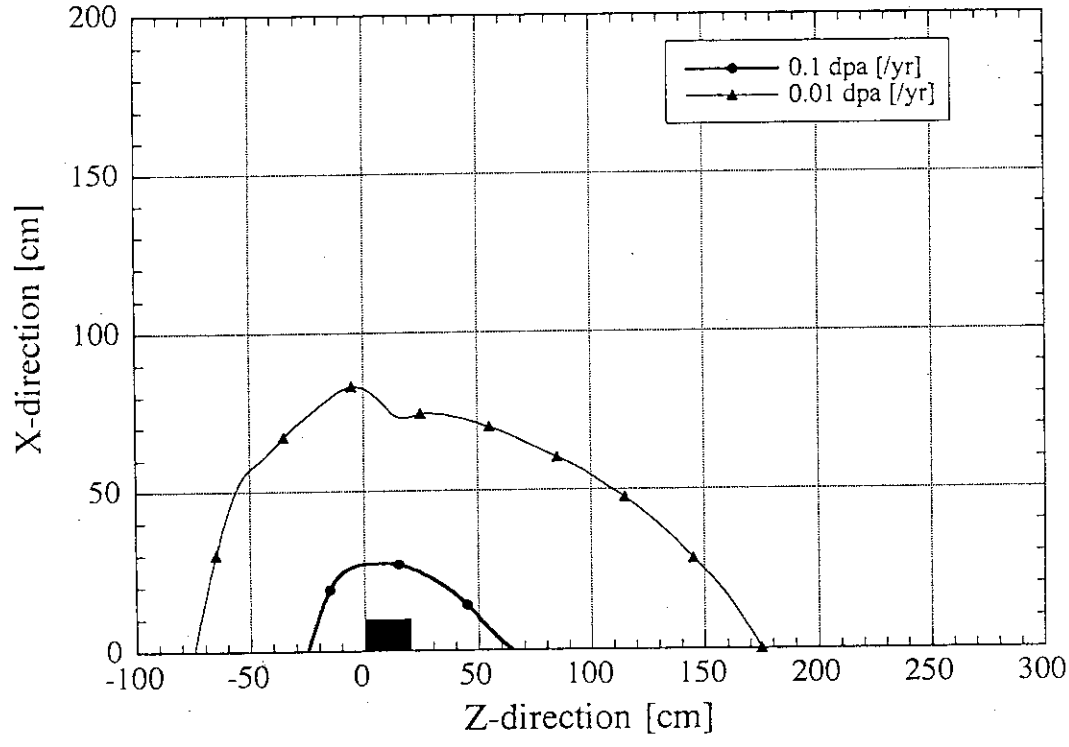

Fig. 5.1.7 Contour plot of dpa rate of C on the x-z plane in the test cell in the case that the SiC50%/NaK30% module is placed for 35 MeV deuteron

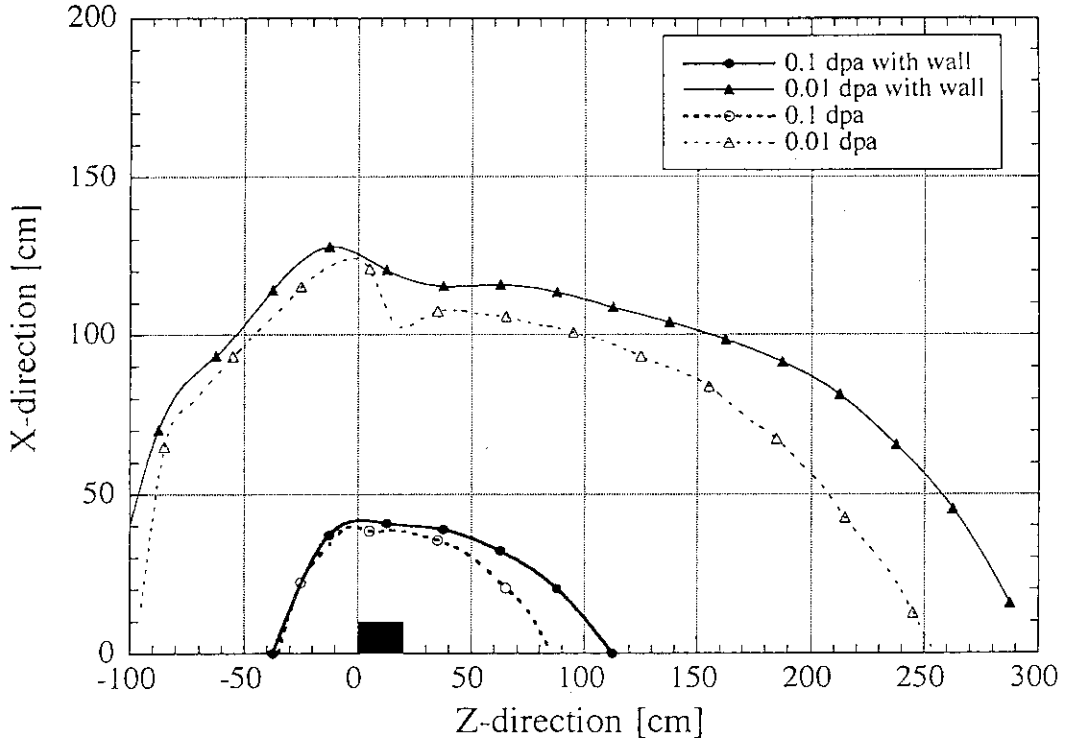

Fig. 5.1.8 Comparison of dpa distributions on x-z plane between the cases with and without the concrete wall in the case that the Fe50%/NaK30% module is placed for 35 MeV deuteron

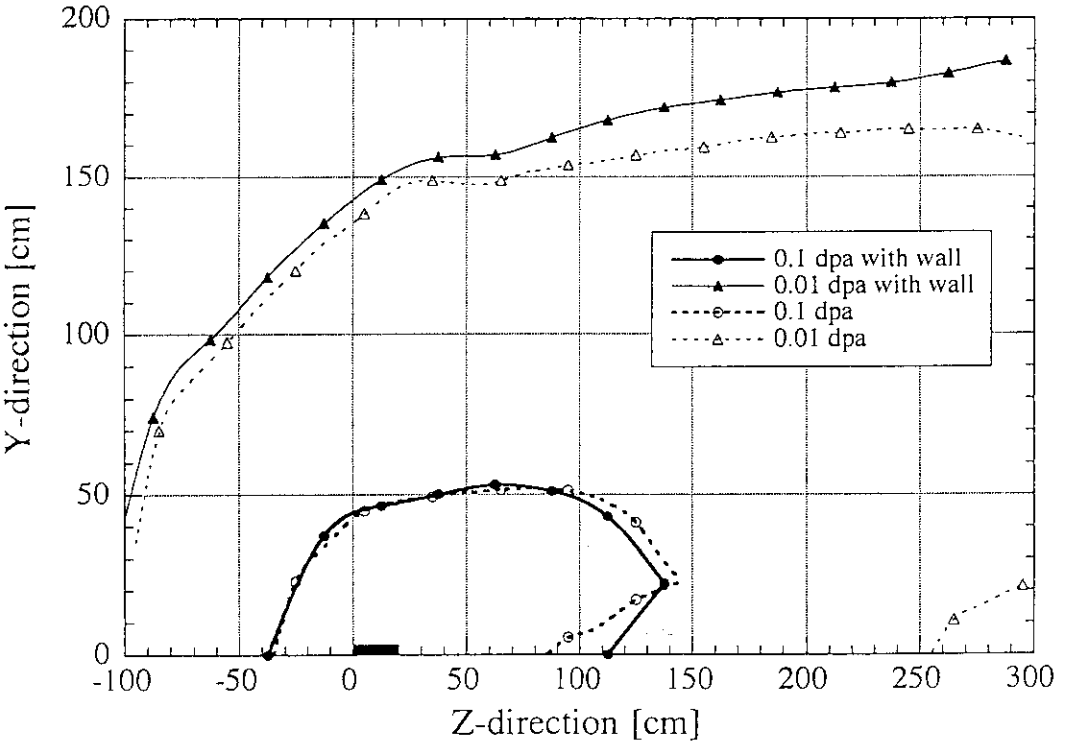

Fig. 5.1.9 Comparison of dpa distributions on y-z plane between the cases with and without the concrete wall in the case that the Fe50%/NaK30% module is placed for 35 MeV deuteron

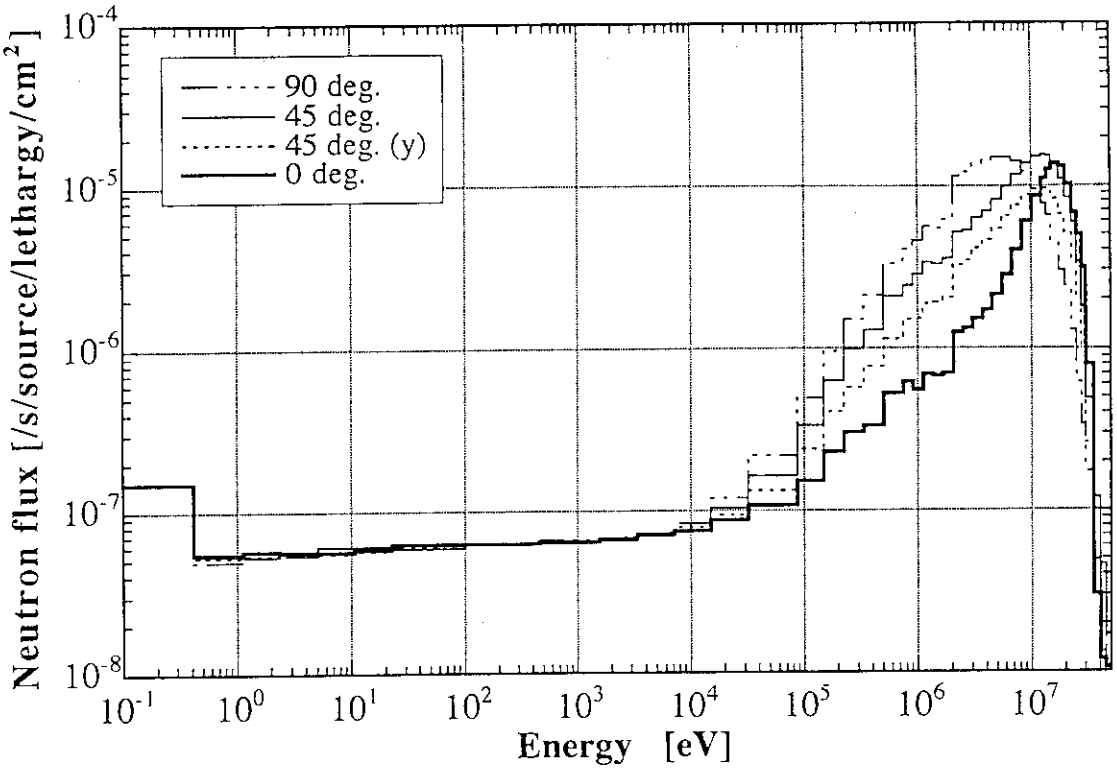

Fig. 5.1.10 Neutron spectra at the boundary of 0.1 dpa/yr with concrete wall in the case that the Fe50%/NaK30% module is placed for 35 MeV deuteron

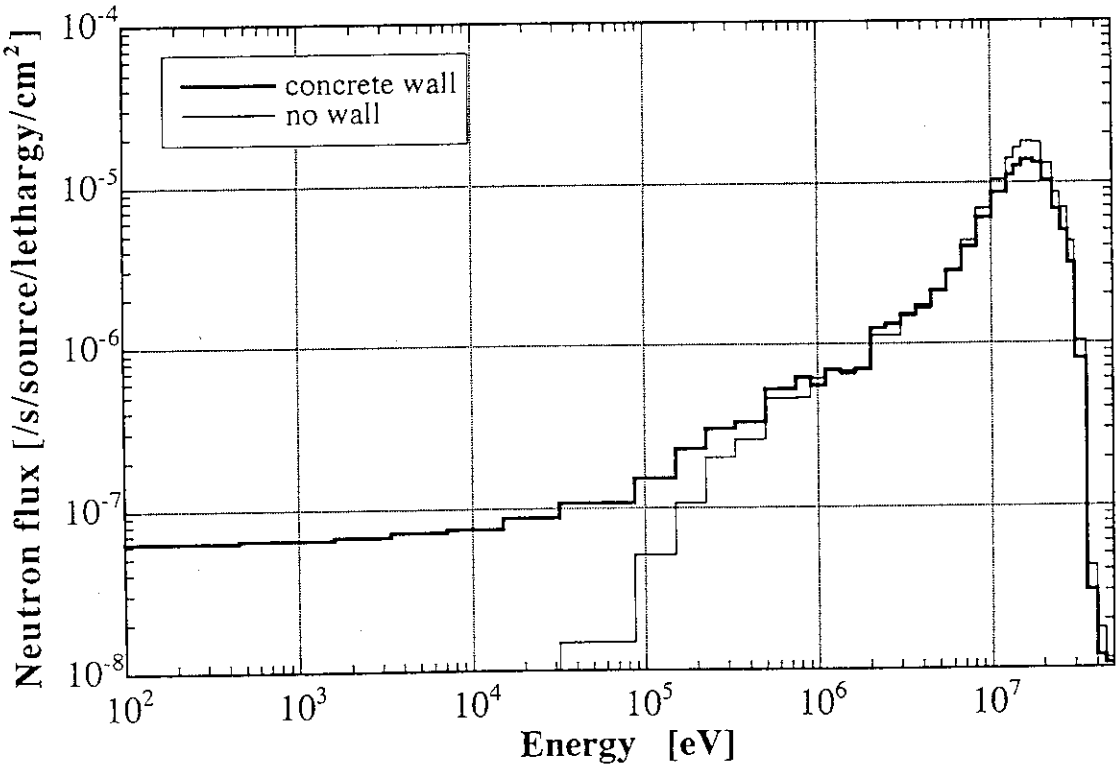

Fig. 5.1.11 Neutron spectra at the forward boundary of 0.1 dpa/yr with and without concrete wall in the case that the Fe50%/NaK30% module is placed for 35 MeV deuteron

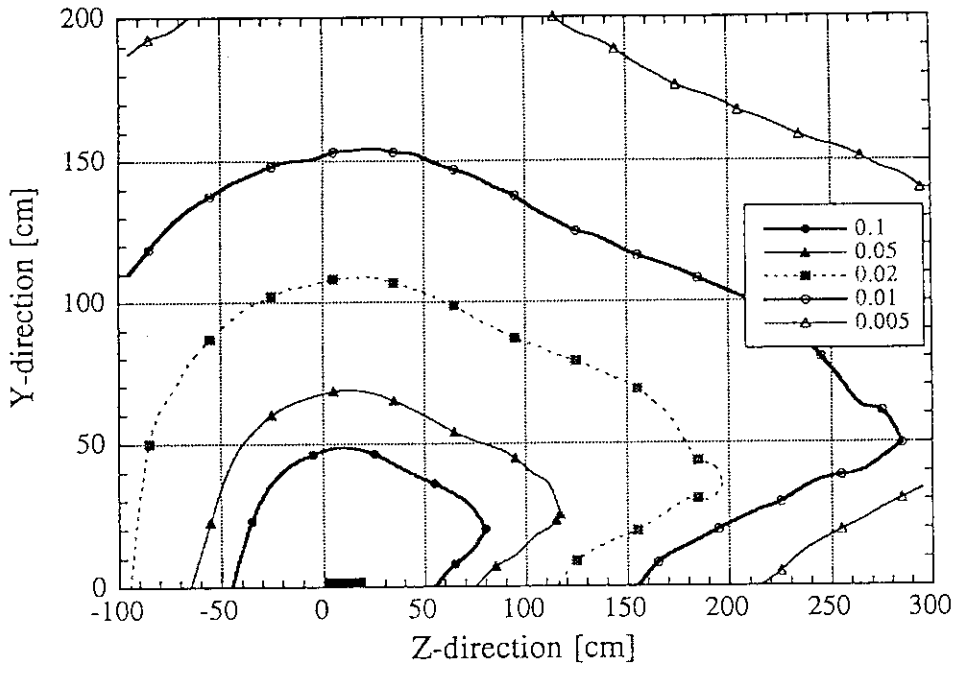

Fig. 5.2.1 Contour plot of total nuclear heating of Fe placed on the y-z plane in the test cell in the case that the Fe50%/NaK30% module is placed for 35 MeV deuteron

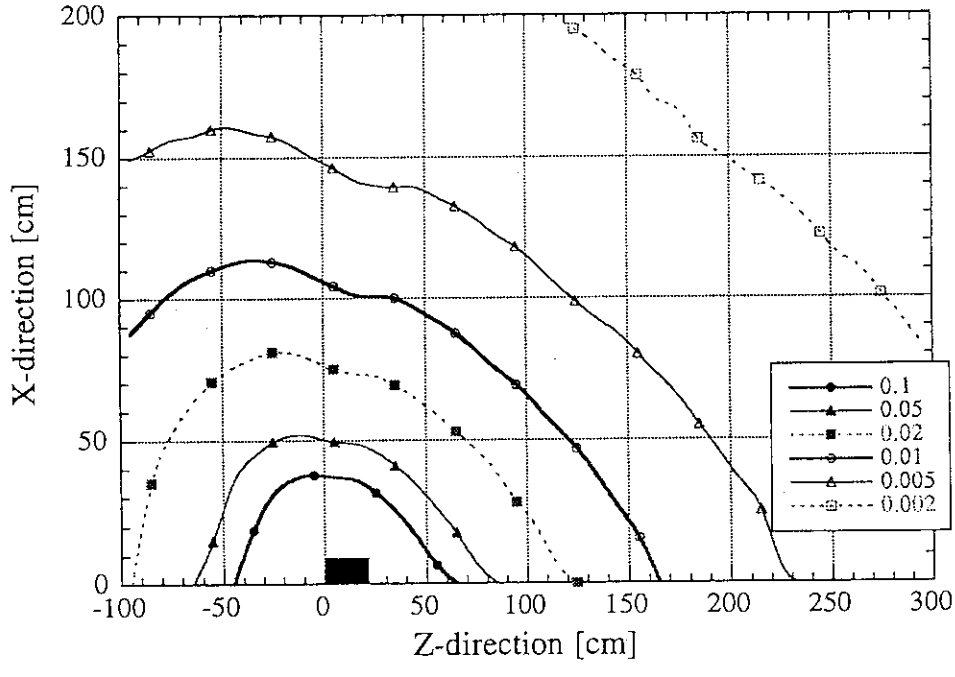

Fig. 5.2.2 Contour plot of total nuclear heating of Fe placed on the x-z plane in the test cell in the case that the Fe50%/NaK30% module is placed for 35 MeV deuteron

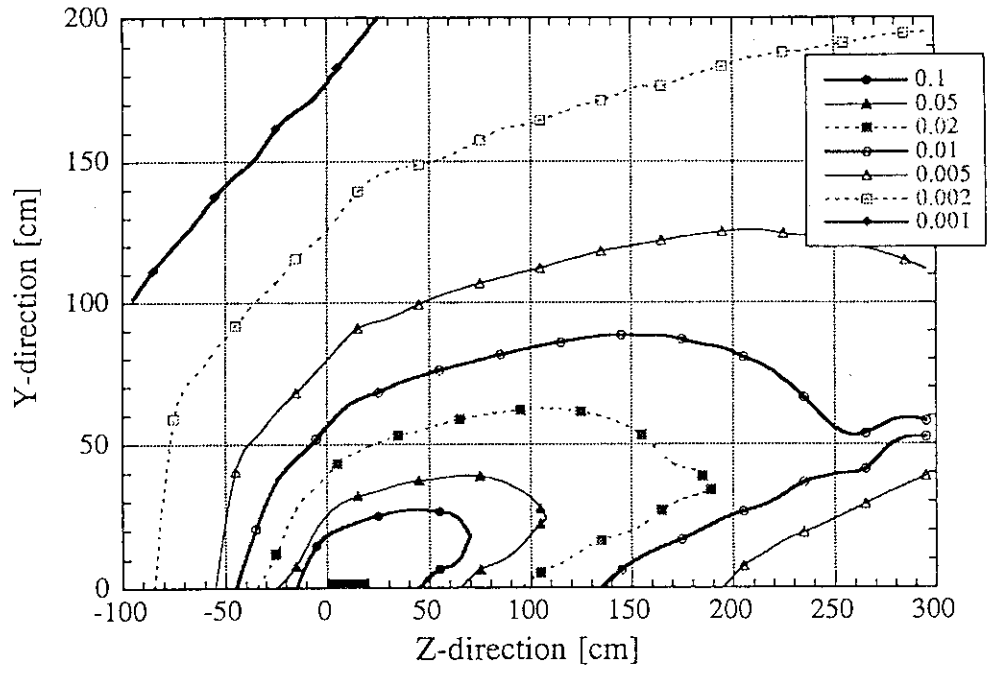

Fig. 5.2.3 Contour plot of neutron nuclear heating of Fe placed on the y-z plane in the test cell in the case that the Fe50%/NaK30% module is placed for 35 MeV deuteron

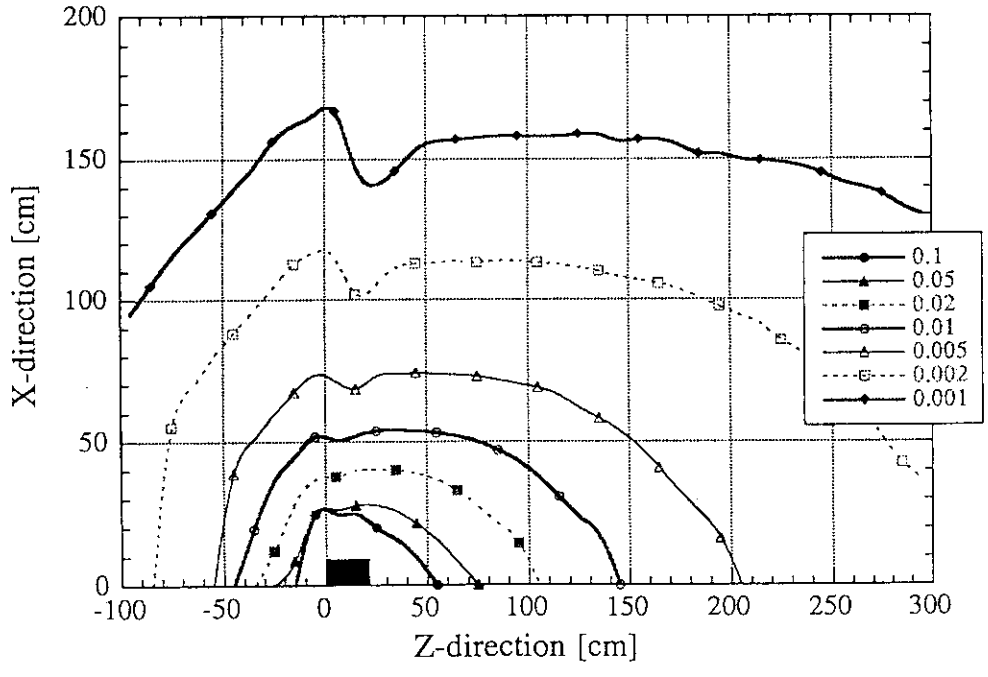

Fig. 5.2.4 Contour plot of neutron nuclear heating of Fe placed on the x-z plane in the test cell in the case that the Fe50%/NaK30% module is placed for 35 MeV deuteron

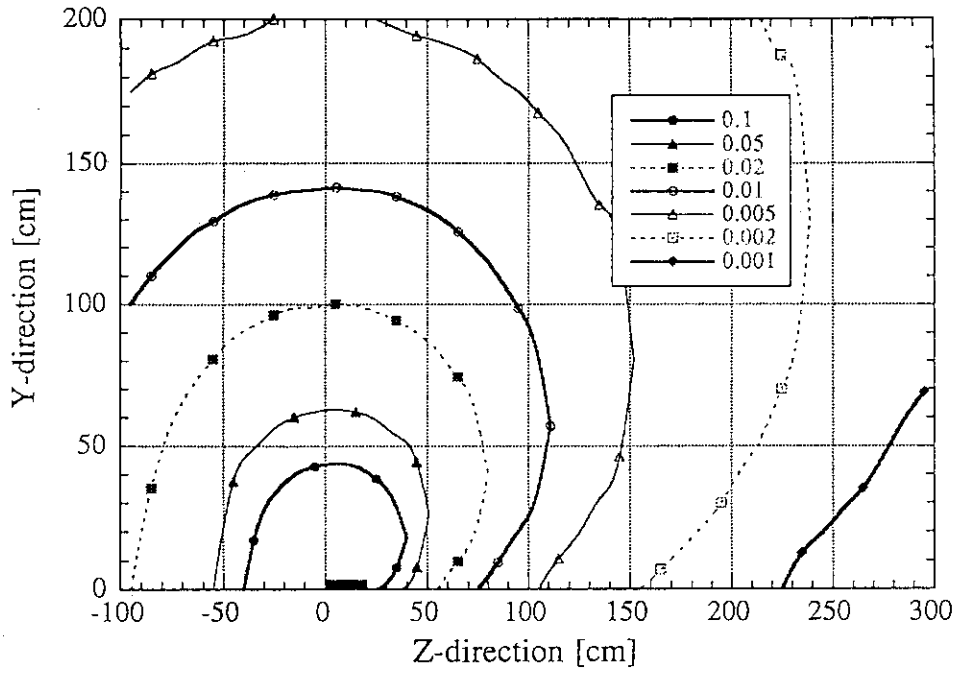

Fig. 5.2.5 Contour plot of gamma-ray heating of Fe placed on the y-z plane in the test cell in the case that the Fe50%/NaK30% module is placed for 35 MeV deuteron

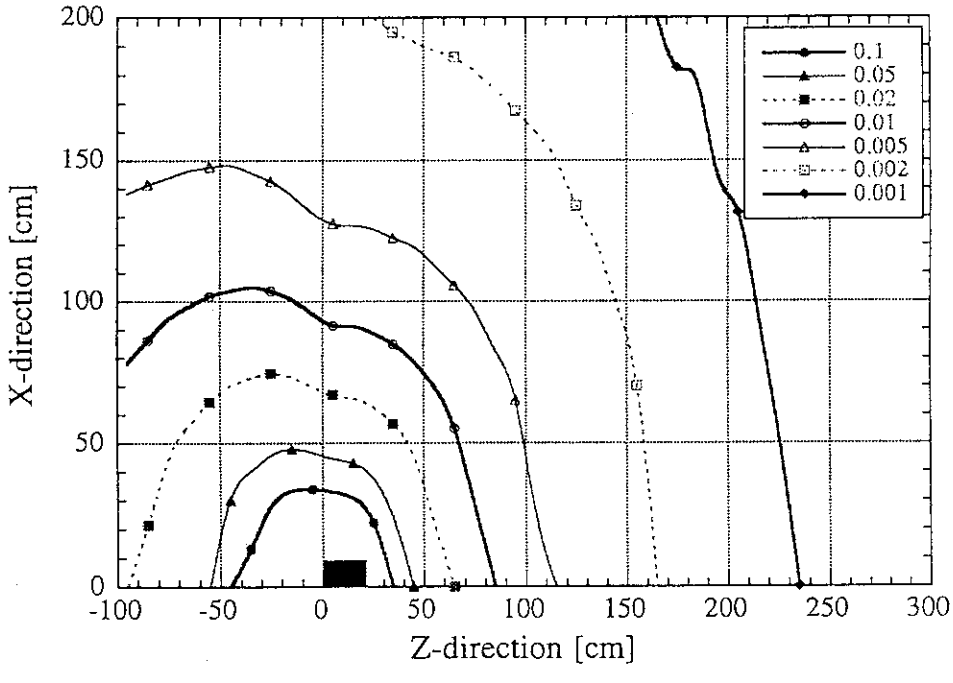

Fig. 5.2.6 Contour plot of gamma-ray heating of Fe placed on the x-z plane in the test cell in the case that the Fe50%/NaK30% module is placed for 35 MeV deuteron

Table 5.1.1 Atomic number densities of concrete wall

Nuclide	atomic number density [$10^{24}/cm^3$]
H-1	1.3851×10^{-2}
C-12	1.1542×10^{-4}
O-16	4.5921×10^{-2}
Mg	1.2388×10^{-4}
Al-27	1.7409×10^{-3}
Si	1.6621×10^{-2}
K	4.6205×10^{-4}
Ca	1.5025×10^{-3}
Fe	3.4510×10^{-4}

6. Impact of D-Li Neutron Source Term Uncertainty on Neutronics Analysis[24]

The estimation of those parameters was made by neutron transport codes using the previously developed source model. Since the present source model is obtained from a rather simple nuclear reaction model, it brings the uncertainty to the calculated flux and spectrum of emission neutrons. Therefore, it is very important to know the uncertainty level of the calculated irradiation parameters originating from the source term uncertainty.

The present work evaluates the uncertainty of the source flux and spectrum used in the calculation, at first. Then a sensitivity of neutron contribution with each energy is examined to the damage parameters such as dpa. Finally the uncertainty of the calculated results of the IFMIF irradiation parameters are estimated.

6.1 Source Model Uncertainty

To obtain the source function as described in Section 2.1, the differential cross section is calculated by the same assumption as that of Johnson et al.[7] with some modifications followed by the method developed in the ESNIT program. The neutron production reaction of $^{7}Li(d,n)^{8}Be$ is only considered for the main reaction among the possible reactions, and in the calculation of cross sections the Serber's stripping reaction model[8] and the evaporation process are taken into account and combined to the source function for generating the emission neutron spectra. This can represent simply a gross structure of spectrum. The source function was normalized at 32 MeV deuteron energy to the Lone evaluation and Sugimoto experiments[9,10], taking average of both experimental values of flux integration above 2 MeV for emission at 0 degree direction. Shown in Figs. 6.1.1-5 are the differential cross sections at 10-40 MeV and at 0 degree with the cross sections used in the FMIT work where the spectrum shape was fitted to the measured one before 1979 available at that time, The present source model is very similar to that used in the FMIT above 20 MeV, except the high energy part representing neutrons with E_d+15 MeV (Q-value) going to the ground state of residual nuclei. This branch is not considered in our model, because the contribution is considered to be small. Thus in our model higher energy neutrons are contributed only by an evaporation tail. For the low energy cross section such as 10 MeV in Fig. 6.1.1 shows evaporation tail in our model, because our model includes evaporation cross section below 15 MeV deuteron incident. The evaporation part is important to represent the angular dependence of neutron spectrum at larger angles. To reproduce this angular distribution, the evaporation cross section is cut off over 15 MeV deuteron.

To compare the spectra by both the models in detail with the Sugimoto experiment, Figs. 6.1.6 and 6.1.7 for 0-150 degree. From these figures, one can see that gloss shape of the spectra over the angles is better for the FMIT model, but the absolute flux around the

peak is better for the JAERI model, especially at the forward direction. Figure 6.1.8 compare the difference between the resulted spectra by both the models. The main difference is the flux around 5 degree and in the regions of the below 4 MeV and above 30 MeV. The JAERI spectrum seems to be more artificial shape.

The comparison of forward neutron emission spectrum, which is more important to evaluate the neutron field inside the test module, is shown in Fig. 6.1.9 with the FMIT model and Sugimoto's experiment measured at 32 MeV. A good agreement can be seen as a whole for the present spectrum, though the peak shape is a little broad. Both the present and FMIT results for thick target spectra are very similar in gross, but the absolute intensity is different. As in the figure, if the FMIT is multiplied by 1.2, the agreement becomes much better. The detailed comparison is given in Table 6.1.1 for each energy region in the calculation-to-experiment ratio (C/E). More than 99 % of neutrons are generated with the energy below 30 MeV. This approves to neglect a high energy part of emission spectrum. For neutrons below 15 MeV, its fraction is 69% and the C/Es are 0.96 and 0.79 for JAERI and FMIT, respectively. Generally the FMIT spectrum gave lower value except high energy part.

Figure 6.1.10 also shows the angular dependence of the emission yield. The JAERI result shows better agreement with the experiment than the FMIT, while worse at angles larger than 30 degree where the difference is a factor of two.

6.2 Sensitivity of Source Neutron Spectrum to the Irradiation Parameters

6.2.1 Sensitivity Calculation for Test Module

Neutron transport calculations to obtain neutron irradiation parameters were performed inside the test module loaded with the test materials samples. A test module was placed in front of the target with three different shapes, i.e., 50x 200, 100x 100 and 25 x400 mm square and with the same depth of 200 mm. As standard loading matrices, the following four cases are considered: for iron sample, 1) Fe 50%, He (and Void) 50%, and 2) Fe 50%, NaK 30%, Void 20%, and for SiC sample, 3) SiC 50%, He (and Void) 50%, and 4) SiC 50%, NaK 30%, Void 20%. The test matrices with the standard loading were averaged by the volume fraction and homogenized. The estimated parameters are calculated for the element of 100% density. The test matrix was placed at 2 mm from the target surface, with yhe 1 mm back wall and 2 mm Li margin in thickness beyond the deuteron range, i.e., for 35 MeV deuteron 19 mm thick Li target was assumed. The test matrix filled by specimen was 20% bigger than the target area in each orthogonal direction and 200 mm in thick. For example, for the 50 mm x 200 mm target, the specimen loading region was 60 mm x 240 mm x 200 mm.

Neutron transport calculation was performed using the Monte Carlo code, GMVP[11]. The parameters in the module to be examined are as follows: 1) Volume available

for the desired dpa rate inside standard loading, 2) Neutron flux distribution inside the samples, 3) Nuclear heating for the samples, and 4) dpa rate distribution, 5) Gas production and nuclear transmutation.

6.2.2 Sensitivity of Source Function and Uncertainty of Calculated Results

Contributions of source neutrons with three energy groups were calculated by the method in the previous section on the parameters such as Fe dpa, heating and He production for the Fe/He cooled module. Table 6.2.1 summarizes contribution ranges for those energies. It is concluded from the table that He production is most sensitive to higher energy, i.e., 30% for neutrons above 20 MeV, and dpa has lower sensitivity. On the other hand, nuclear heating is less sensitive to such high energy range.

Table 6.2.2 summarizes the uncertainties of source function for corresponding energies based on the comparison with Sugimoto experiment. Sensitivity of source term to nuclear responses is determined by complicated way of uncertainties of source function, i.e., uncertainties of energy spectra for every emission angle. Here to simplify the method and to roughly estimate impact of the source term, the uncertainty of source term is assumed to be represented by that of the forward emission spectrum. Hence by multiplying sensitivity in Tables 6.2.1 calculated with the uncertainty estimated from the comparison of the forward emission spectrum to the experiment in Table 3, and summing up for total response, the uncertainty of the calculated parameters due to the source function uncertainty can be estimated as also shown in Table 6.2.2. However, one should noted that the this estimation does not reflect the impact of the uncertainty due to cross section sets used.

From Table 6.2.2, the impact of the source function uncertainty estimated for dpa, heating, gas production are as follows: 1) A 75-85% fraction of dpa for Fe is determined by neutrons below 20 MeV. 2) A 10% uncertainty of neutron emission above 20 MeV contributes to those of the total dpa only by 2-3% , of the total heating by 1% and of the He production by 2-3%. 3) A 10% uncertainty of 10-20 MeV neutrons contributes to those of the total dpa by 4-5 %, of the total heating by 6% and of the He production by 6%. 4) Considering the source term uncertainty, the uncertainties of nuclear responses by the ESNIT and the FMIT models ranged in ~ 8% and ~ 17%, respectively.

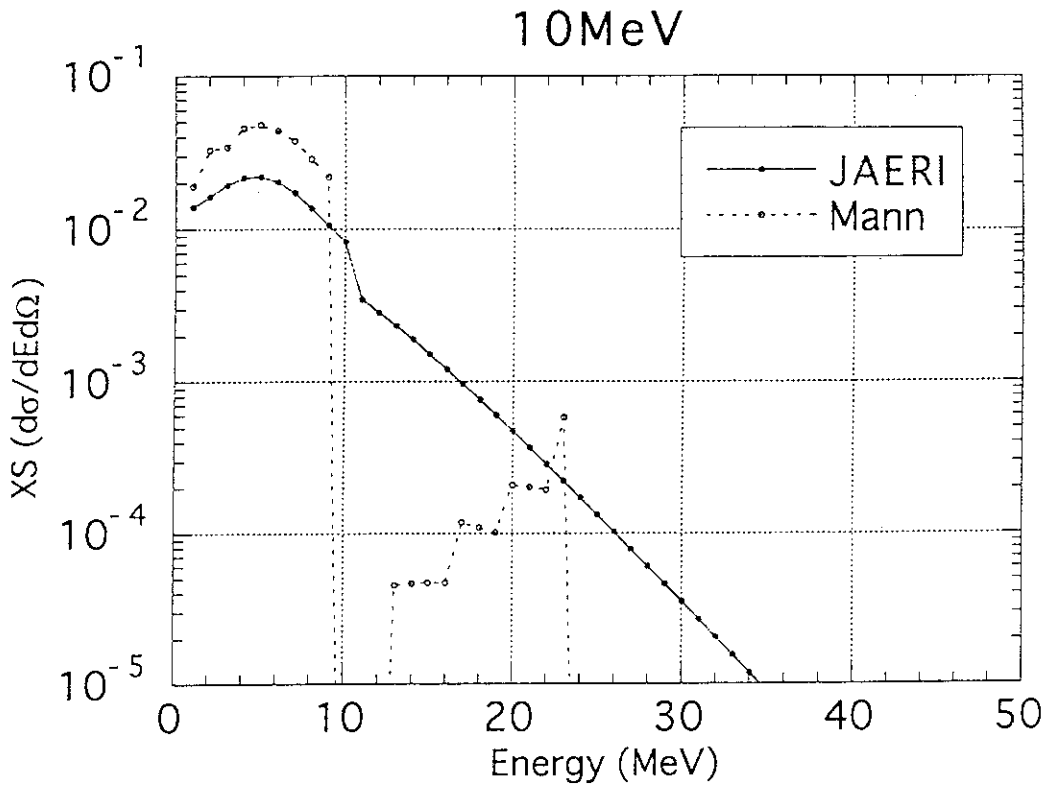

Fig. 6.1.1 Differential cross section of 10 MeV deuteron for Li used in both the JAERI and FMIT(Mann) models

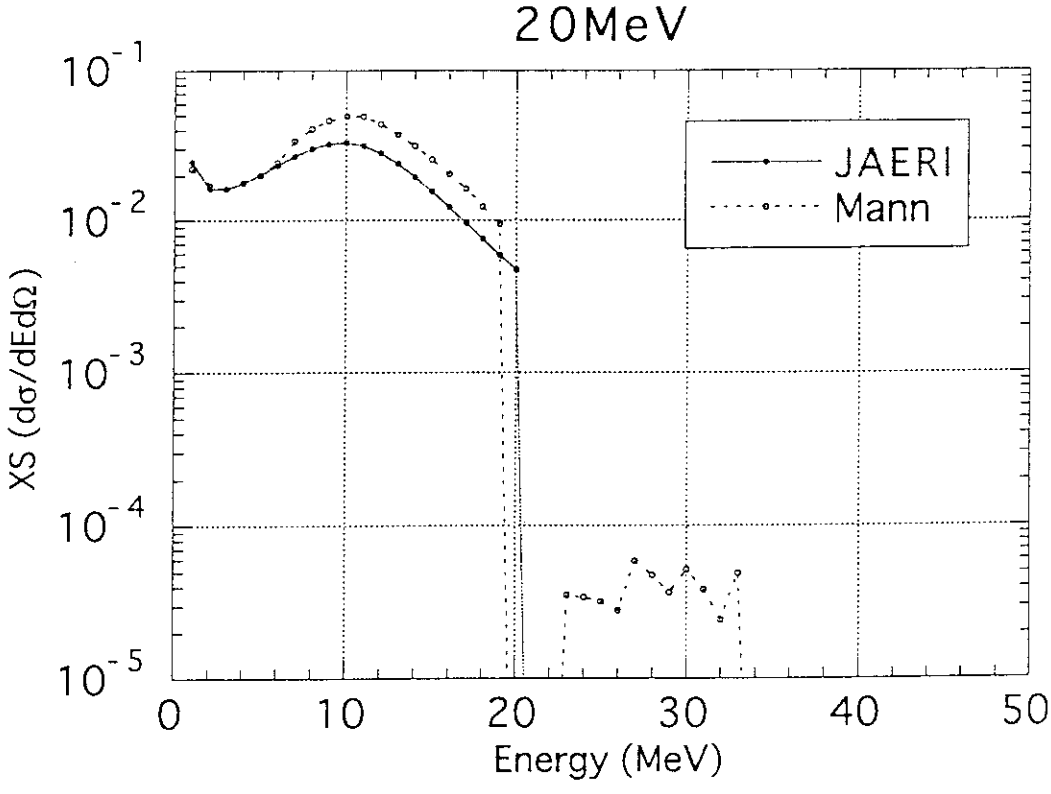

Fig. 6.1.2 Differential cross section of 20 MeV deuteron for Li used in both the JAERI and FMIT(Mann) models

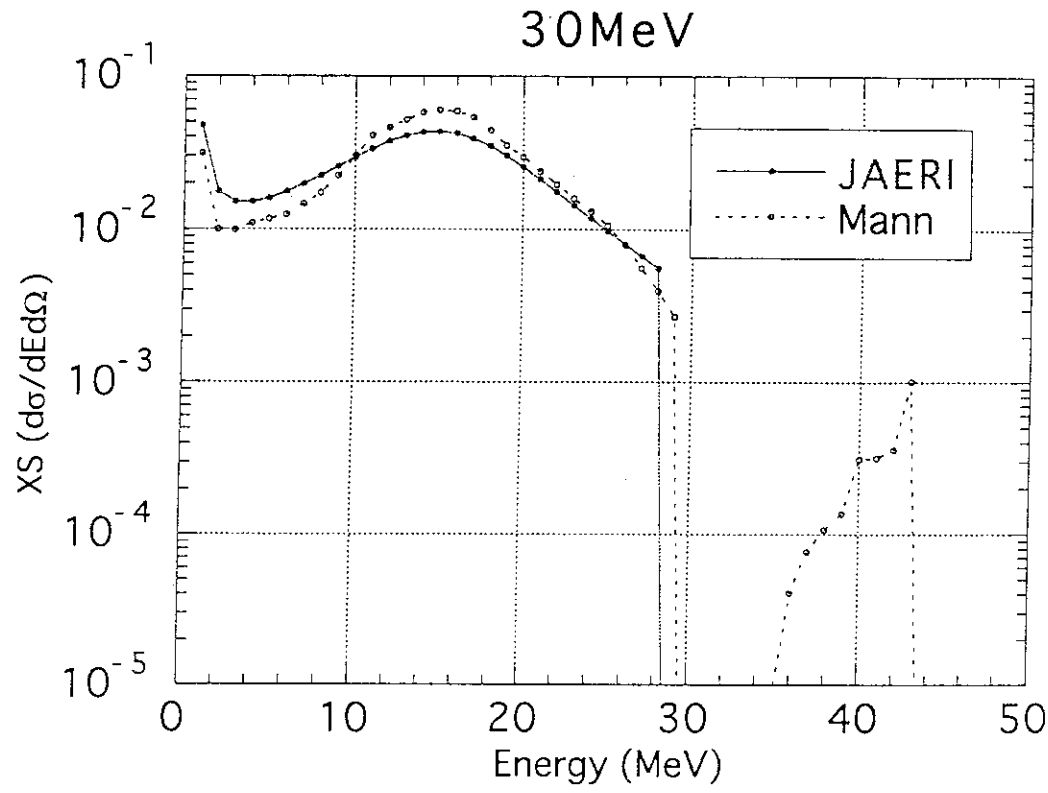

Fig. 6.1.3 Differential cross section of 30 MeV deuteron for Li used in both the JAERI and FMIT(Mann) models

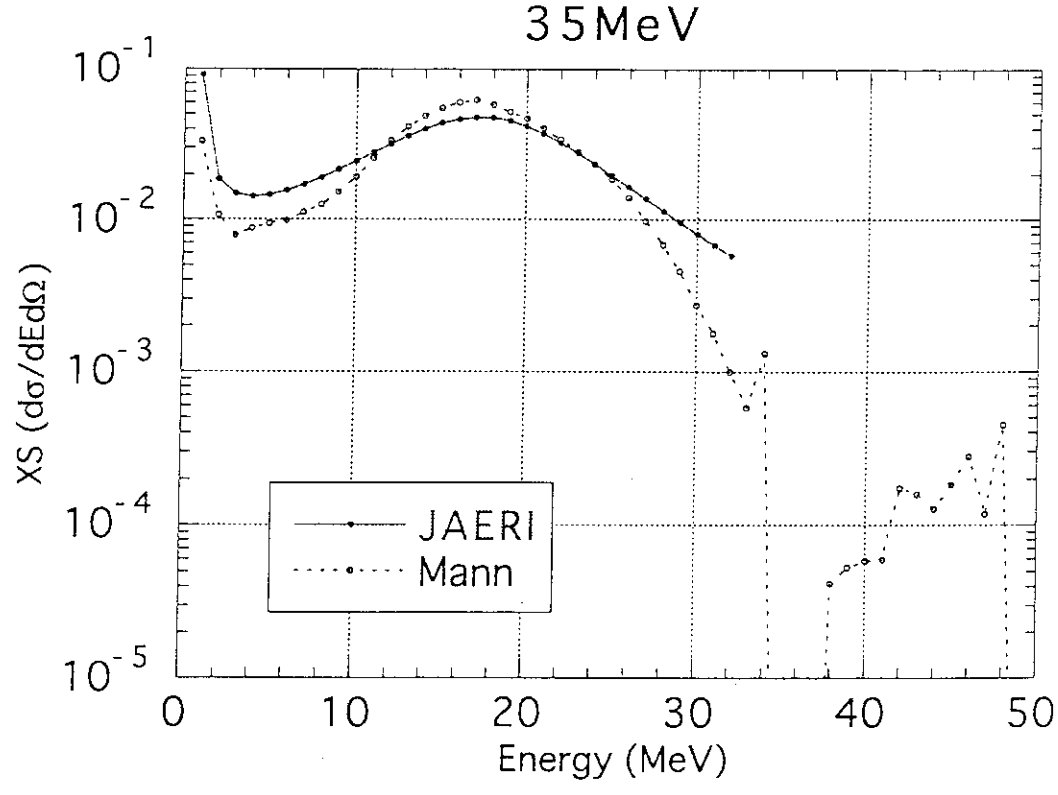

Fig. 6.1.4 Differential cross section of 35 MeV deuteron for Li used in both the JAERI and FMIT(Mann) models

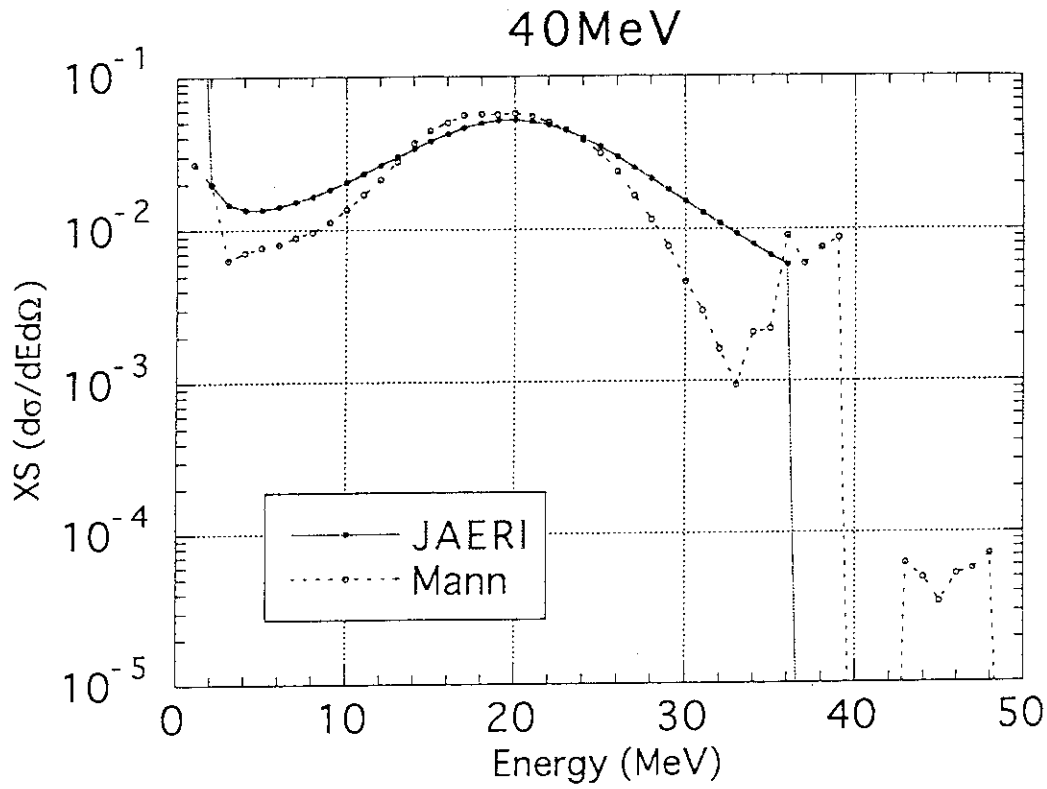

Fig. 6.1.5 Differential cross section of 40 MeV deuteron for Li used in both the JAERI and FMIT(Mann) models

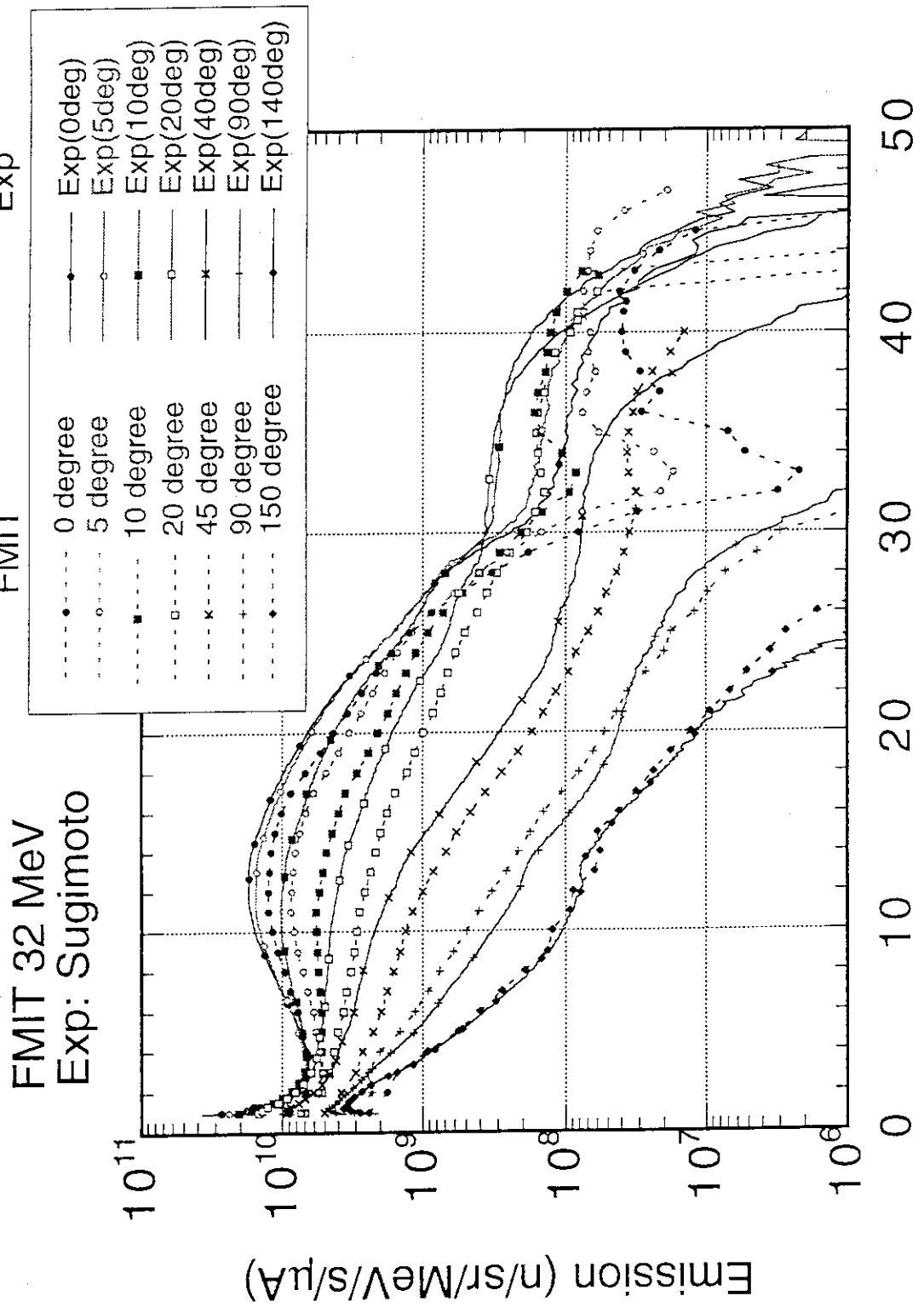

Fig. 6.1.6 Comparison of angle dependent neutron spectra for the 32 MeV thick target experiment to the FMIT calculation

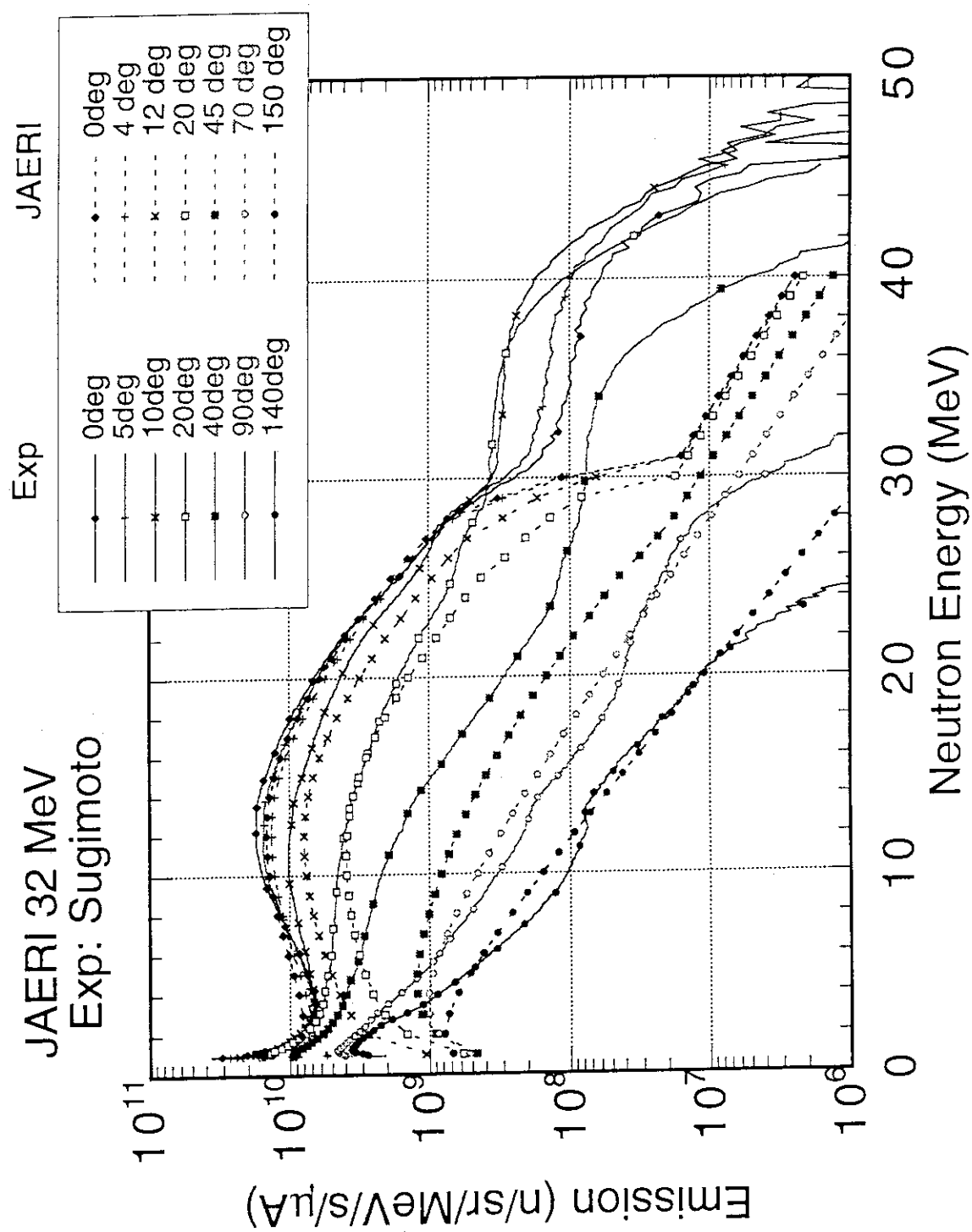

Fig. 6.1.7 Comparison of angle dependent neutron spectra for the 32 MeV thick target experiment to the JAERI calculation

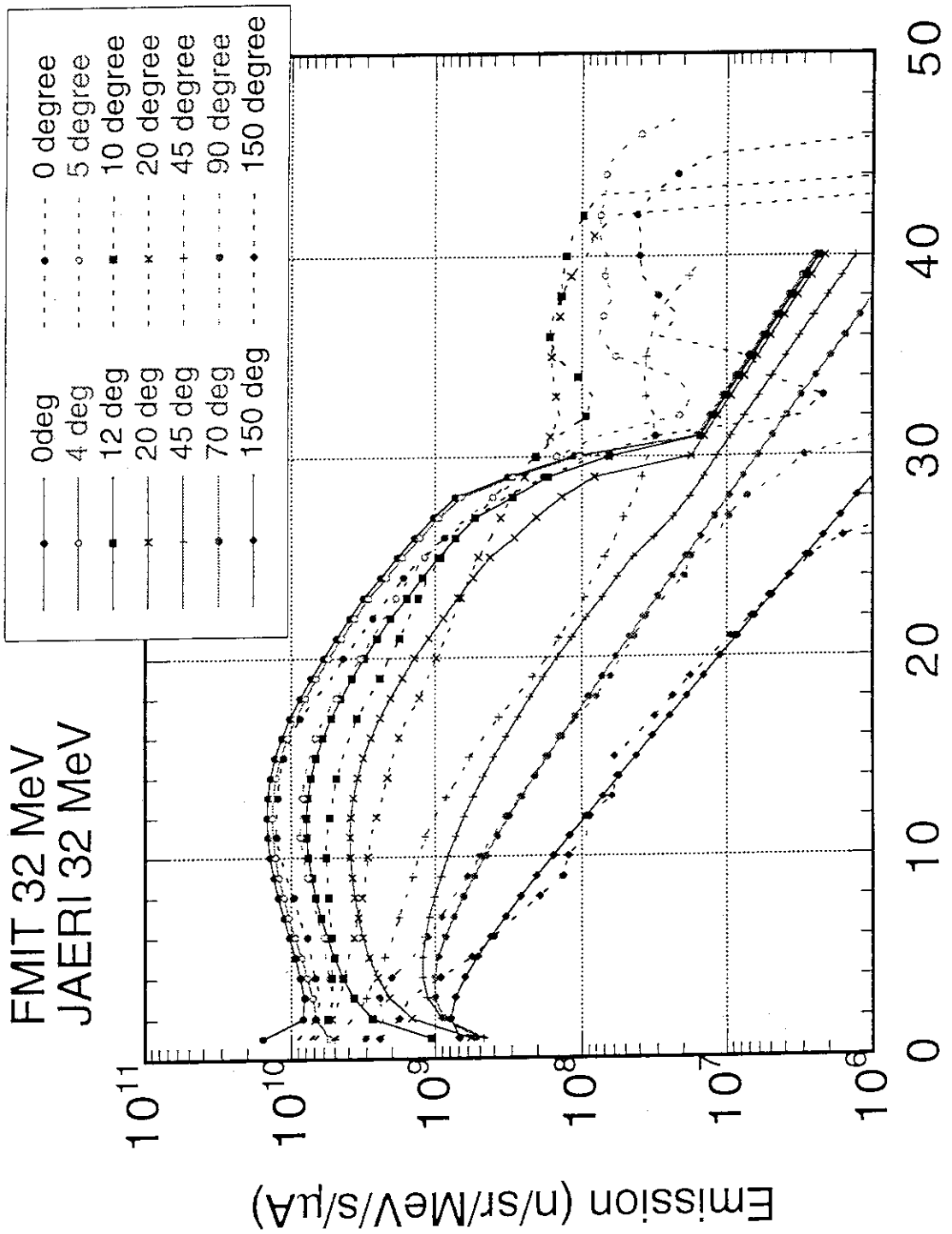

Fig. 6.1.8 Comparison of angle dependent neutron spectra for the 32 MeV thick target calculations between the JAERI and the FMIT calculations

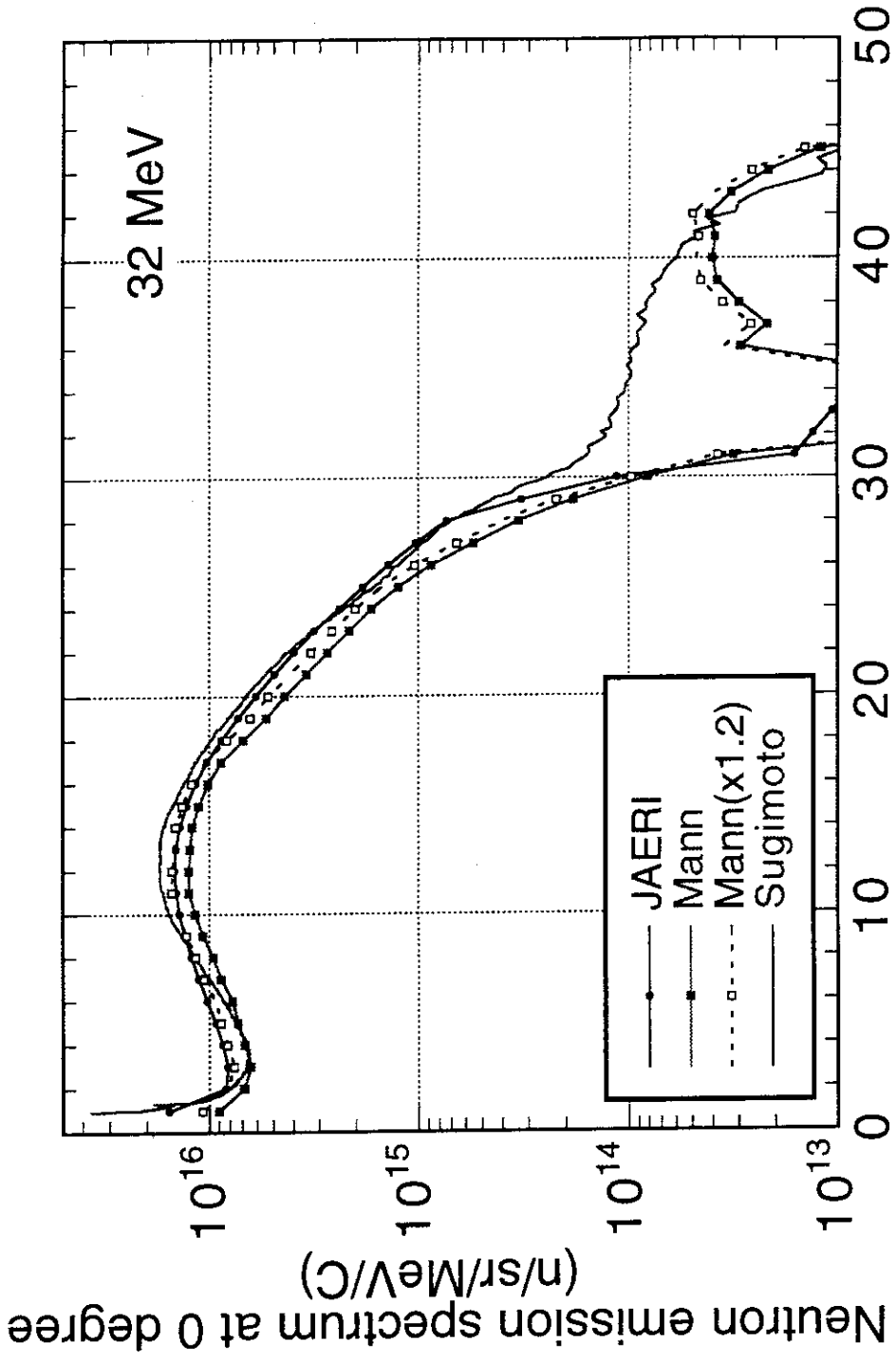

Fig. 6.1.9 Comparison of the forward emission spectra at 32 MeV deuteron incident for the experiment and the calculations

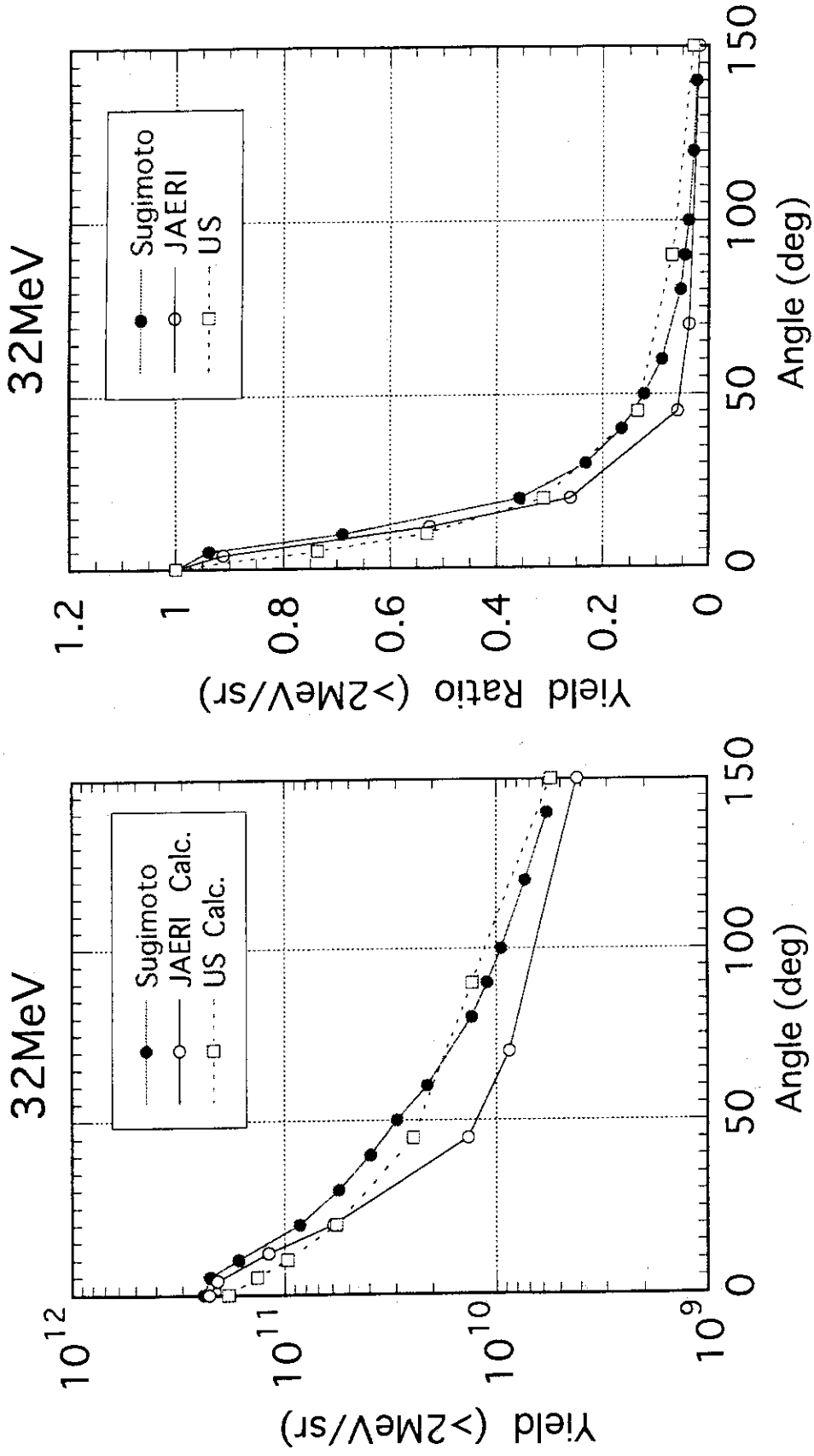

Fig. 6.1.10 Comparison of the angular dependence of the neutron flux integrated above 2 MeV (left: log, right: linear)

Table 6.1.1 Comparison of the integrated forward flux calculated by our source model (single beam) to the measured ones (emission angle=0 degree, 32 MeV deuteron)

Energy range [MeV]	Sugimoto Experiment [n/sr/s/mA]	Fraction to total flux of 1-50 MeV	JAERI Model	C/E	FMIT model	C/E
1-2	1.28e+10	0.051	1.21e+10	0.945	7.95e+9	0.623
2-10	7.66e+10	0.304	8.46e+10	1.104	6.70e+10	0.874
10-15	8.40e+10	0.333	7.12e+10	0.848	6.13e+10	0.730
15-30	7.76e+10	0.308	7.06e+10	0.911	5.46e+10	0.703
30-40	1.10e+9	0.004	1.31e+8	0.119	2.28e+8	0.208
40-50	1.63e+8	0.00065	not given	------	1.68e+8	1.029
Total	2.52e+11	1.00	2.39e+11	0.946	1.91e+11	0.758

Table 6.2.1 Sensitivity of source neutron energy to the parameters of Fe/He cooled test module (Ed=35MeV, 250 mA)

Energy range of source neutron	Source flux / 4p		Contribution range over module[%]		
	Partial yield [n/s]	Fraction [%]	dpa of Fe	Total nuclear heating	^{4}He production of ^{56}Fe
1-10MeV	3.54e+16	58	20-40	37	12-19
10-20MeV	2.17E+16	35.5	45-55	55	59-61
> 20MeV	3.96e+15	6.5	15-25	8	20-29
Total	6.10e+16	100	100	100	100

Table 6.2.2 Uncertainty of calculated parameters

Energy range	Uncertainty of Source Function		Uncertainty of calculated parameters					
			dpa of Fe		Total heating		^{4}He production	
	JAERI	FMIT	JAERI	FMIT	JAERI	FMIT	JAERI	FMIT
1-10 MeV	+8%	-16%	+1.6-3.2%	-(3.2-6.4)%	+3%	-6%	+1-1.5%	-(1.9-3)%
10-20 MeV	-14%	-27%	-(6.3-7.7)%	-(12-15)%	-7.7%	-15%	-(8.3-8.5)%	-(16-16.5%)
> 20 MeV	-7%	-36%	-(1.1-1.8)%	-(5.4-9)%	-0.56%	-2.9%	-(1.4-2)%	-(7.2-10)%
total	-5%	-24%	-(4-6)%	-(21-30)%	-5%	-30%	-9%	-(27-30)%

7. Summary

As the conceptual design study of International Fusion Material Irradiation Facility, neutron field characteristics are studied. Cross section model is provided for developing neutron source term of D-Li reaction target.

The deuteron beam specification was determined for the beam angle and beam foot print shape. First the beam angle was optimized for two beam geometry, and the optimum angle of 10 degree is obtained. Second the height of the beam foot print should be larger than 50 x 200 mm square case.

Volume-Flux Relation

The reference foot print shape, 50 mm x 200 mm , provides 0.3 litter and 0.75 litter irradiation volumes for NaK and He coolant cases, for 20 and 10 dpa/y, respectively. If the 100 mm x 100 mm target is used, the 0.4 and 1 litter volumes for 20 and 10 dpa/y can be obtained. To increase the irradiation volume for the reference target by 0.4 litter, the beam current should be increased by 300 mA. The effect of sample loading, i.e., perturbation due to the test module, is about 20-40% reduction of irradiation volume and the lower flux region has higher reduction. For SiC, the 0.5 and 1 litter volumes can be obtained in the reference target for 20 and 10 dpa/y of Si, respectively. To obtain 0.4 litter for a region over 20 dpa , the deuteron beam current is required to increase from 250 mA to 300 mA for Fe loading module. The flux gradient inside the matrix is steeper than 10%/cm, which is the requirement from the user, and close to 15%/cm.

Gas production, dpa and Transmutation

The He/dpa ratio ranges 13.6 to 14.5, and the ratio increases for the thinner target of 25 mm x 400 mm. For transmutation production from Fe, the production ratios of ^{54}Cr is larger but that of ^{53}Cr is smaller than those of ferritic steel in the SSTR of the Japanese DEMO reactors, i.e., the ferritic steel and water cooling reactor. For transmutation production from SiC, the production ratios of ^{27}Al and ^{24}Mg are larger than that of DREAM of the other DEMO concept, i.e., SiC/He reactor.

Nuclear Heating

Nuclear heating by neutrons in the Fe matrix is almost equal to the gamma-ray heating, but neutron heating in the SiC matrix is ten times larger. The total heating is about 20 W/cm^3 at front region of the matrix.

Low dpa region

Low dpa rate region such as 0.01 or 0.1 dpa/y can be obtained behind the module

and inside the test cell.

Uncertainty of the Calculation

The source function uncertainty in the IFMIF neutronics calculation was estimated by comparison with the recent experimental data. The source uncertainty was about 5% in total. The sensitivity of these uncertainty was calculated by the contribution of source neutrons with separated energy to the parameters calculated for the IFMIF test module with standard loading.

The results showed the JAERI calculation has the uncertainties of about -5% for dpa and heating, and of -9% for He production, while the FMIT model gives the uncertainties of -(20-30)% for dpa and -30% for heating and He production. As a result, the uncertainty of our source function gives about -(5-9)% uncertainty for the irradiation parameter estimation.

In conclusion, the irradiation field of the proposed IFMIF could satisfy the dpa rate required from the user, but not the gradient. The space besides the test module can also be used for low flux irradiation of functional materials. These evaluation is assured with an accuracy less than 10%.

Acknowledgments

The author would like to express their thanks to the IFMIF group at JAERI for collaborative work. They also thank international colleagues of IFMIF/CDA for valuable discussion.

and inside the test cell.

Uncertainty of the Calculation

The source function uncertainty in the IFMIF neutronics calculation was estimated by comparison with the recent experimental data. The source uncertainty was about 5% in total. The sensitivity of these uncertainty was calculated by the contribution of source neutrons with separated energy to the parameters calculated for the IFMIF test module with standard loading.

The results showed the JAERI calculation has the uncertainties of about -5% for dpa and heating, and of -9% for He production, while the FMIT model gives the uncertainties of -(20-30)% for dpa and -30% for heating and He production. As a result, the uncertainty of our source function gives about -(5-9)% uncertainty for the irradiation parameter estimation.

In conclusion, the irradiation field of the proposed IFMIF could satisfy the dpa rate required from the user, but not the gradient. The space besides the test module can also be used for low flux irradiation of functional materials. These evaluation is assured with an accuracy less than 10%.

Acknowledgments

The author would like to express their thanks to the IFMIF group at JAERI for collaborative work. They also thank international colleagues of IFMIF/CDA for valuable discussion.

References

(1) Torego A.L., et al.: Nuclear Technology/Fusion, 4(2), 695 (1983).

(2) Noda K., Oyama Y., Yamaguchi S., Maekawa H. and Hishinuma A.: J. Nucl. Materials, 174, 319 (1990).

(3) Kondo T., Doran D.G., Ehrlich K. and Wiffen F.W.: J. Nucl. Mateterials, 191-194, 100 (1992).

(4) "IFMIF-International Fusion Materials Irradiation Facility Conceptual Design Activity, Final Report", IFMIF-CDA Team, edited by M. Martone, RT/ERG/FUS/96/11, ENEA Frascati (December, 1996).

(5) Oyama Y., Yamaguchi S., Kosako K., Maekawa H.: " Calculation of Neutron Field Generated at Thick Li Target bombarded with 10-40 MeV Deuterons for Energy Selective Neutron Irradiation Test facility," JAERI-M 92-191, Japan Atomic Energy Research Institute (1992).

(6) Anderson H. M. and Ziegler J. F.: "Hydrogen Stopping Power and ranges in All Elements," Pergamon Press (1977).

(7) Johnson D. L., Mann F. M., Watson J.W., Ullmann J. and Wyckoff W. G.: J. Nucl. Materials, 85 & 86, 467 (1979).

(8) Serber R.: Phys. Rev., 72, 1008 (1947).

(9) Lone M. A. and Bigham C. B.: in Neutron Source for Basic Physics and Application, Chapter VI, OECD/NEA report, (1983) p.140.

(10) Sugimoto M.: private communication, Japan Atomic Energy Research Institute (1994).

(11) Mori T. and Nakagawa M.: "MVP/GMVP-General Purpose Monte Carlo Codes for Neutron and Photon Transport Calculations based on Continuous Energy and Multigroup Methods," JAERI-Data/Code 94-007, Japan Atomic Energy Research Institute (1994).

(12) Emmett M.B.: "The MORSE Monte Carlo Radiation Transport Code System," Oak Ridge National Laboratory report, ORNL-4972, (1975).

(13) Oyama Y. and Kosako K.: "HILO86/J3 Library for IFMIF Neutronics Design," private communication (1995).

(14) Alsmiller R. G. Jr. and Barish J.: "Neutron-Photon Multigroup Cross Sections for Neutron Energies up to 400 MeV," Oak Ridge National Laboratory report, ORNL/TM-7818, (1981).

(15) Shibata K., Nakagawa T., Asami T., Fukahori T., Narita T., Chiba S., Mizumoto M., Hasegawa A., Kikuchi Y., Nakajima Y. and Igarasi S.: "Japanese Evaluated Nuclear Data Library, Version-3 - JENDL-3-," JAERI 1319, Japan Atomic Energy Research Institute (1990).

(16) Yamano N., Minami K., Koyama K. and Naito Y.: "RADHEAT-V4: A Code System to Generate Multigroup Constants and Analyze Radiation Transport for Shielding Safety Evaluation," JAERI-1316, Japan Atomic Energy Research Institute (1989).

(17) Nakagawa T.: "JENDL-3 Revision 2," JAERI-M 94-019, Japan Atomic Energy Research Institute, pp. 68-78 (1994).

(18) Oyama Y., Noda K., Kosako K., Yamano N.: J. Nucl. Materials., 233-237, 1577 (1996).

(19) Gomes I.C. and Smith D.L.: Fus. Eng. Des., 28, 724 (1995).

(20) Yamano N. and Tabara T.: "Development of DPA Cross Section Library and Transmutants Calculation Code System for Energy Selective Neutron Irradiation Test Facility", Report of ESNIT International Advisory Meeting, Japan Atomic Energy Research Institute (1993).

(21) Seki Y., et al.: "Steady State Tokamak Reactor," JAERI-M 91-081, Japan Atomic Energy Research Institute (1991).

(22) Seki Y., et al.: "Advanced Tokamak Reactor, DREAM", private communication (1994).

(23) Engle W. W.: "A User's Manual for ANISN, A One-Dimensional Discrete Ordinate Transport Code with Anisotropic Scattering," K-1693, Union Carbide Corporation, Computing Technology Center (1976).

(24) Oyama Y., Kosako K. and Noda K.,: "Impact of D-Li Neutron Source Term Uncertainty on Neutronics Analysis," 4th Int. Symp. on Fusion Nucl. Technol., April 6-11, Tokyo, Japan (1997).